

Vitrification Mechanisms in Soft Colloidal Mixtures

Inaugural-Dissertation
zur
Erlangung des Doktorgrades der
Mathematisch-Naturwissenschaftlichen Fakultät
der Heinrich-Heine-Universität Düsseldorf

vorgelegt von

CHRISTIAN MAYER

aus Düsseldorf

Düsseldorf, Februar 2007

Aus dem Institut für Theoretische Physik II
der Heinrich-Heine Universität Düsseldorf

Gedruckt mit Genehmigung der
Mathematisch-Naturwissenschaftlichen Fakultät
der Heinrich-Heine-Universität Düsseldorf

Referent: Prof. Dr. C. N. Likos
1. Koreferent: Prof. Dr. H. Löwen
2. Koreferent: Prof. Dr. K. Binder

Tag der mündlichen Prüfung: 27. April 2007

© Christian Mayer 2007
All Rights Reserved.

This thesis is based on the following original papers:

Chapter 2

C. N. Likos, C. Mayer, E. Stiakakis, and G. Petekidis,
Clustering of soft colloids due to polymer additives,
Journal of Physics: Condensed Matter **17**, 3363 (2005).

C. Mayer and C. N. Likos,
A coarse-grained description of star-linear polymer mixtures,
to appear in Macromolecules (2007).

Chapter 3

E. Zaccarelli, C. Mayer, A. Asteriadi, C. N. Likos, F. Sciortino, J. Roovers,
H. Iatrou, N. Hadjichristidis, P. Tartaglia, H. Löwen, and D. Vlassopoulos,
Tailoring the flow of soft glasses by soft additives,
Physical Review Letters **95**, 268301 (2005).

C. Mayer, E. Stiakakis, E. Zaccarelli, C. N. Likos, F. Sciortino, P. Tartaglia,
H. Löwen, and D. Vlassopoulos,
Rheological transitions in asymmetric colloidal star mixtures,
to appear in Rheologica Acta (2007).

Chapter 4

C. Mayer, E. Zaccarelli, C. N. Likos, F. Sciortino, P. Tartaglia, and H. Löwen,
Multiple glass transitions in star polymer mixtures,
(in preparation) (2007).

C. Mayer, E. Zaccarelli, C. N. Likos, F. Sciortino, P. Tartaglia, and H. Löwen,
Local ordering in binary star polymer mixtures,
(in preparation) (2007).

Chapter 5

F. Lo Verso, C. N. Likos, C. Mayer, and L. Reatto,
Effect of attraction on the dynamical arrest of soft colloids,
Molecular Physics **104**, 3523 (2006).

F. Lo Verso, C. N. Likos, C. Mayer, and H. Löwen,
Collapse of telechelic star polymers to water-melon structures,
Physical Review Letters **96**, 187802 (2006).

Abstract

In this thesis, we deal with mixtures of macromolecules in good solvent. Star polymers are used as a model system for colloids with soft interactions. In the first part of the thesis we consider mixtures of star polymers with linear polymer chains. On the basis of computer simulations and theory an effective interaction between stars and chains is derived and subsequently used in order to calculate the structure of the fluid. We find evidence for the formation of clusters in the system which we compare with experimental results. Moreover, we study the influence of the linear chains on the glass transition of the star polymers. Afterwards, we turn our attention to binary star polymer mixtures. By using the Mode Coupling Theory for the glass transition, glass lines are calculated and compared to rheological measurements of the same system. Subsequently, we calculate the dynamical properties of the system by molecular dynamics simulations. Finally, we investigate star polymers with attractive interactions. As a first model system we consider solutions of macromolecules which attract each other and study their glass formation. Afterwards, we study so called telechelic star polymers with mutually attracting end groups. We study the conformations of a single molecule depending on the temperature and the transition to collapsed states.

Zusammenfassung

In der vorliegenden Dissertation haben wir uns mit Mischungen von Makromolekülen in gutem Lösungsmittel beschäftigt. Als Modellsystem für Kolloide mit weicher Wechselwirkung wurden dabei Sternpolymere verwendet. Im ersten Teil der Arbeit betrachten wir Mischungen von Sternpolymeren mit linearen Polymerketten. Auf der Basis von Computersimulationen und Theorie wird eine effektive Wechselwirkung zwischen Sternen und Ketten hergeleitet und anschließend verwendet, um die Struktur der Flüssigkeit zu berechnen. Dabei finden wir Hinweise auf die Bildung von Clustern in dem System, die wir mit experimentellen Ergebnissen vergleichen. Außerdem untersuchen wir den Einfluss der linearen Ketten auf den Glasübergang der Sternpolymere. Danach wenden wir uns binären Mischungen von Sternpolymeren zu. Mit Hilfe der Modenkopplungstheorie des Glasübergangs werden Glaslinien berechnet und mit rheologischen Messungen am selben System verglichen. Anschließend berechnen wir die dynamischen Eigenschaften der Mischung mit Molekulardynamik-Simulationen. Zuletzt studieren wir Sternpolymere mit attraktiven Wechselwirkungen. Als erstes Modellsystem betrachten wir Lösungen von Makromolekülen, die sich gegenseitig anziehen und untersuchen ihre Glasbildung. Danach betrachten wir so genannte telechelische Sternpolymere, bei denen sich die Enden jedes Arms wechselseitig anziehen. Wir untersuchen die Konformationen eines einzelnen Moleküls in Abhängigkeit von der Temperatur und den Übergang zu einem kollabierten Zustand.

Contents

1	Introduction	11
2	Mixtures of Star Polymers and Linear Chains	15
2.1	Effective Interactions	15
2.2	Early Approaches	16
2.2.1	Interactions	16
2.2.2	Fluid Structure in Dilute Star Solutions	17
2.2.3	Chain-Mediated Effective Interaction	20
2.2.4	Experimental Findings	21
2.2.5	Cluster Formation in Other Systems	21
2.3	Star-Star and Chain-Chain Interactions	24
2.4	Star-Chain Interactions	26
2.4.1	Molecular Dynamics Simulations	26
2.4.2	Theory of the Star-Linear Effective Interaction	27
2.5	The Many-Body Problem	36
2.5.1	Mixtures at Low Star Concentrations	36
2.5.2	Mixtures for High Star Concentrations	43
2.6	Conclusions	46
3	Binary Star Polymer Mixtures: Dynamical Phase Behavior	49
3.1	Introduction	49
3.2	Experiments	50
3.3	Structure of the System	54
3.4	Phase Diagram	57
3.5	Elastic Modulus	58
3.6	Summary and Conclusions	60
4	Binary Star Polymers: Relaxation Dynamics	63
4.1	Asymptotic Solutions of the MCT Equations	63
4.2	MCT Results	65
4.3	Simulations: Iso-diffusivity Lines	70

4.4	Multiple Glassy States	74
4.4.1	Region I: Single Glass	74
4.4.2	Region II: Double Glass	78
4.4.3	Region III: Second Double Glass	79
4.4.4	Region IV: Attractive Glass and Phase Separation	82
4.5	Conclusions	84
5	Ultrasoft Systems with Attractive Interactions	85
5.1	Attractive Forces in Star Polymer Solutions	85
5.1.1	Theoretical Model	85
5.1.2	Mode Coupling Results	87
5.1.3	Conclusions	89
5.2	Collapse of Telechelic Star Polymers	89
5.2.1	Introduction	89
5.2.2	Molecular Dynamics simulations	90
5.2.3	Free Energy	94
5.2.4	Conclusions	97
6	Conclusions and Outlook	99
A	Ornstein-Zernike Equation for Binary Mixtures	101
B	Mode Coupling Theory	103
	Acknowledgments	115

Chapter 1

Introduction

Soft matter science deals with the study of systems that have structure on a mesoscopic length scale, i.e., ranging typically from 1 nm to 1 μm [1, 2], dispersed in molecular or atomic solvents. All soft matter systems (also called complex fluids or colloidal dispersions) are easily deformable, giving rise to their name. An abundant number of soft matter systems exist in nature. Viruses, proteins, and DNA molecules all share this characteristic length scale. Additionally, many products in use in everyday life belong to this class. Indeed, most products of food, pharmaceutical, and the chemical industry fall into this category. Examples for soft matter systems are ink used in ball point pens and xerography, as well as many varieties of paints and cosmetics [1]. Therefore there is a great deal of interest in understanding the macroscopic properties (statics and dynamics) of these systems based on their composition and molecular architecture. The fact that the constituent particles of complex fluids have an enormous number of internal degrees of freedom renders the problem even more challenging than in simple classical fluids. The possibility to synthesize the constituents in the laboratory allows for the opportunity to design material properties (almost) at wish, a possibility that is completely absent in atomic systems, where the properties of the individual particles cannot be altered.

There are two basic scenarios for the formation of colloidal dispersions. In the first case, the solute already has dimensions between 1 nm and 1 μm , e.g., proteins, polysaccharides, and many synthetic polymers [1]. In the second case, the systems consist of small molecules which form aggregates in solution; the mesoscopic structures are not synthesized chemically, but self-organize in the solution. Soap molecules for example form micellar structures at high concentrations [1].

The macroscopic states of condensed matter can be characterized as fluids or solids. While the latter systems are shear-resistant, the former ones flow. Usually with solid-like behavior a regular crystal structure is associated. However, glasses show solid-like macroscopic dynamics but feature the microscopic structure of a disordered fluid. One of the most interesting phenomena in soft condensed matter

systems is the slowing down at dynamical arrest, related to the glass transition [3,4]. Under the influence of concentration or temperature changes dense systems show a slowing-down of their dynamics, characterized by an increase of their viscosity by several orders of magnitude for small variations of the external parameters. However, while for crystallization the arrested state is connected to a breaking of the symmetry of the fluid, glasses show a structure which is very similar to that of the underlying supercooled liquid. So while the structure of the system is unchanged at the glass transition, the dynamics of fluid and glass becomes completely different, with density fluctuations not relaxing in time in the latter state.

In atomic and molecular systems, dynamical arrest is usually related to the glass transition [4]. In soft condensed matter there exist a lot of different arrested states: repulsive and attractive glasses, gels, associating polymers, and so on [4]. The abundance of arrested states is due to the vast range of effective interaction potentials in soft matter. Therefore, a large number of studies has dealt with the simplest colloidal dispersion which consists of spherical hard particles of mesoscopic size [5]. In the theoretical description they are modeled as ideal hard spheres which show no interactions when their center-to-center distance is larger than their diameter and exhibit an infinite interaction energy when they overlap. One of the most commonly studied experimental systems consists of poly-(methyl methacrylate) (PMMA) particles with grafted poly-(12-hydroxy stearic acid) (PHSA) to stabilize the system against van der Waals attraction [6]. This has been shown to be a very good realization of a hard sphere system [6]. The ideal hard sphere system is a commonly used reference system for the study of the structure and dynamics of fluids and solids, especially for the colloidal glass transition (for a recent review, see [4]). Due to the form of the potential, hard spheres are athermal and can be characterized by one single parameter, the volume fraction $\eta = \pi\rho\sigma^3/6$, where ρ is the number density and σ the diameter of the spheres. It has been shown in the 1950s by computer simulations that this system has a phase transition from a fluid to a face centered cubic crystal with a coexistence region between $0.49 < \eta < 0.545$ [7]. However, it was found experimentally, that for $\eta > 0.58$ no crystallization happens in the experimental time window [8]. The studies of the dynamics of hard sphere colloids have been an important confirmation [4] of the quantitative predictions of Götze's Mode Coupling Theory (MCT) for the glass transition [3]. Nevertheless, questions like the influence of gravitation on the colloidal glass transition are still debated [4].

Another success in the understanding of colloidal glasses was the study of colloids with short range attractions. In mode coupling theory a reentrant glass transition was found [9], i.e., with increasing strength of the attraction the system goes from a repulsive glass to a fluid and becomes again arrested in an attractive glass. The shape of the phase diagram was confirmed in experiments on colloid-polymer mixtures [10,11]. Moreover, computer simulations of short range attractive colloids confirmed the experimental and theoretical findings [12,13].

In this thesis, however, we will turn our attention to the influence of particle *softness* on the macroscopic properties of the system, especially on cluster formation and vitrification. Star-shaped polymers [14,15] have emerged as a well-characterized, tunable and highly versatile model colloidal system which displays very rich equilibrium and dynamical behavior. Additionally, star polymers are also interesting from a technical point of view. Hydrogenated polyisoprene star polymers are used as viscosity index modifiers in the oil industry [14], other star systems are used in coating materials, as binders in toners for copying machines, and in pharmaceutical and medical applications [14]. The physical parameter that determines the softness of these macromolecular aggregates is the number f of polymer chains that are anchored on a common center, also called *functionality* of the star. Focusing on the mesoscopic length scales, the fluctuating monomers of the f chains in a concentrated star-polymer solution can be integrated out, leaving behind a collection of ‘effective point particles’ (the star centers) that interact by means of a monomer-mediated, soft effective repulsion [16]. The versatility of star polymers arises physically from the influence of the functionality f on the softness of this repulsion: it has been shown [17,18] that it depends logarithmically on the star-star separation for overlapping distances, crossing over to an exponential decay for larger ones. The functionality influences both the overall strength of the repulsion, in the form of a $f^{3/2}$ -prefactor, and the decay length of the exponential tail which scales as $\sigma f^{-1/2}$, with σ denoting the corona diameter of the star [18].

Whereas for sufficiently low functionalities, $f \leq f_c = 32$, the star-star repulsion is too weak to sustain stable crystals at arbitrary concentrations, for $f > f_c$ and above the stars’ overlap density, stable bcc (body centered cubic) and fcc (face centered cubic) crystals are predicted to be the equilibrium structures, accompanied by reentrant melting and formation of open crystal structures at even higher densities [19,20]. The formation of ordered fcc- and bcc-crystals has recently found experimental confirmation for various star-like systems stemming from self-organized block copolymers [21–24]. Yet, for real star-polymer samples, the development of periodic structures is usually hindered by glass formation, which is further encouraged by the inherent polydispersity of the solutions [25,26]. A recent, mode coupling analysis based on the effective interaction of Ref. [18], has shown that the vitrification of star polymers can be understood along the same lines as the dynamical arrest of a hard-sphere system, driven by the existence of a density-dependent, effective hard-sphere diameter between the stars [27]. Accordingly, the observed melting of the star-polymer glass upon addition of shorter homopolymer chains has been attributed to the ability of the additives to bring about a softening of the star-star repulsion and a concomitant reduction of the effective hard-sphere diameter between the same [28].

In the course of this dissertation, we study in detail mixtures of star polymers with linear chains as well as binary star polymer mixtures. We focus on two aspects

of these systems: depletant induced cluster formation and the influence of the additives on the rheological properties of the system. The rest of this thesis is organized as follows. In chapter 2 we introduce a model for star polymer-chain mixtures. We show cluster formation and glass transitions in the system and compare our results to recent experimental data. In chapter 3, we investigate the dynamics of binary star polymer mixtures and compare the data to rheological measurements, before we show a detailed study of the relaxation dynamics of such systems in chapter 4. In chapter 5, we present data for a one component model of star polymers with competing short range attraction and long range repulsion. Moreover, we study star polymers with mutually attractive end groups on each arms in dilute solution. Finally, we summarize and draw our conclusions in chapter 6.

Chapter 2

Mixtures of Star Polymers and Linear Chains

In this section, we study dynamics and equilibrium structure of mixtures of polymer chains and stars in solution. We propose an accurate model for the star-chain effective interaction. Employing this model, we study the formation of clusters and the long-time dynamics of the mixture and compare our results to recent experimental data.

2.1 Effective Interactions

The strategy employed throughout this work is that of *coarse-graining* of both components, the stars and the linear chains (coded with the subscripts ‘s’ and ‘c’, respectively, in what follows.) In this approach, which enables us to form a bridge between the microscopic and the mesoscopic scales, suitable coordinates that characterize the star and the chain as a whole are chosen and all the remaining fluctuations of the monomers are traced out in a well-defined statistical mechanical fashion [16]. In particular, the effective coordinates are kept fixed in any prescribed configuration and the restricted, canonical partition function of all the remaining ones is (approximately) calculated. To simplify the situation, suppose that we are having only two mesoscopic particles (regardless of their type) in the system and let $\mathbf{r}_{1,2}$ denote the *fixed* position vectors of their respective effective coordinates. Denote as $\mathcal{Z}_{\alpha\beta}(\mathbf{r}_1, \mathbf{r}_2)$ the aforementioned restricted partition function, where $\alpha, \beta = c, s$. The quantity of interest is then the *effective interaction* $V_{\alpha\beta}(\mathbf{r}_1, \mathbf{r}_2)$, defined as

$$V_{\alpha\beta}(\mathbf{r}_1, \mathbf{r}_2) = -k_{\text{B}}T \ln \left[\frac{\mathcal{Z}_{\alpha\beta}(\mathbf{r}_1, \mathbf{r}_2)}{\mathcal{Z}_{\alpha\beta}(|\mathbf{r}_1 - \mathbf{r}_2| \rightarrow \infty)} \right], \quad (2.1)$$

with Boltzmann’s constant k_{B} and the absolute temperature T . We also define here $\beta = (k_{\text{B}}T)^{-1}$ for future reference. In other words, the effective interaction is

the free energy cost for bringing the two particles from infinity to their prescribed positions \mathbf{r}_1 and \mathbf{r}_2 . When averaging over all but a single effective coordinate of a macromolecule and there are only two such present, we have $V_{\alpha\beta}(\mathbf{r}_1, \mathbf{r}_2) = V_{\alpha\beta}(r)$, where $r = |\mathbf{r}_1 - \mathbf{r}_2|$. In general, many-body effective terms result from the process of coarse-graining but they are ignored in the pair-potential approximation. In a system containing \mathcal{N}_s stars and \mathcal{N}_c chains, the total effective potential energy U reads then as:

$$U = \sum_{i < j}^{\mathcal{N}_s} \sum_{j=1}^{\mathcal{N}_s} V_{ss}(|\mathbf{r}_i - \mathbf{r}_j|) + \sum_{i < j}^{\mathcal{N}_c} \sum_{j=1}^{\mathcal{N}_c} V_{cc}(|\mathbf{r}_i - \mathbf{r}_j|) + \sum_{i=1}^{\mathcal{N}_s} \sum_{j=1}^{\mathcal{N}_c} V_{sc}(|\mathbf{r}_i - \mathbf{r}_j|). \quad (2.2)$$

Hence, both species, stars and chains are figured as soft spheres interacting with the corresponding soft potentials $V_{\alpha\beta}(r)$.

2.2 Early Approaches

In this section, we keep our attention on star-chain mixtures while turning our focus to the regime of low- or intermediate concentrations of the stars, i.e., far from their overlap concentration and the associated crystallization or vitrification phenomena. Our theoretical modeling will be based on a heuristic ansatz for the effective star-chain interactions which was already used with great success to explain experimental data in [28]. In Sec. 2.4, we will derive an accurate expression for the interaction and verify it by monomer resolved simulation. We consider a mixture of star polymers with functionality f with smaller linear chains. Following a coarse-graining procedure for both species, we describe the stars by their centers and the chains by their centers of mass. With r denoting the separation between any two such coordinates, the mesoscopic structure of the system can then be determined by using the three effective interaction potentials $V_{ij}(r)$, $i, j = s, c$, together with the physical characteristics of the system: the star functionality f , the chain-to-star size ratio $\xi < 1$, as well as the partial number densities $\rho_i = \mathcal{N}_i/\Omega$, where \mathcal{N}_i denotes the number of stars ($i = s$) or chains ($i = c$) enclosed in the macroscopic volume Ω . As we are dealing with polymers in athermal solvents throughout, the temperature appears in all effective interactions involved exclusively in the form of a prefactor $k_B T$ (with k_B being Boltzmann's constant), and therefore does not play any role in the structure of the system.

2.2.1 Interactions

For the three effective interactions $V_{ij}(r)$, we adopt the same expressions used in preceding studies of the vitrification properties of star-chain mixtures [28]. The star-star interaction, $V_{ss}(r)$, is given by a combination of a logarithmic and a Yukawa

potential of Ref. [18]

$$\beta V_{\text{ss}}(r) = \frac{5}{18} f^{3/2} \begin{cases} -\ln\left(\frac{r}{\sigma_s}\right) + \frac{1}{1 + \sqrt{f}/2} & \text{for } r \leq \sigma_s; \\ \frac{1}{1 + \sqrt{f}/2} \frac{\sigma_s}{r} \exp\left[-\frac{\sqrt{f}}{2\sigma_s}(r - \sigma_s)\right] & \text{else,} \end{cases} \quad (2.3)$$

featuring a crossover from the logarithmic to the exponential form at the aforementioned length scale σ . Extensive computer simulations have established between this length and the radius of gyration R_g of the stars the relation $\sigma \cong 1.2 R_g$ [29]. The chain-chain effective potential has been derived in the work of Louis *et al.* [30,31]:

$$V_{\text{cc}}(r) = 1.87 k_B T \exp[-(r/\tau)^2], \quad (2.4)$$

where $\tau = 1.13 R_g^{\text{lin}}$ and R_g^{lin} is the linear chains' gyration radius. Finally, a heuristic form for the cross interaction, based on typical overlap energy estimates, has been adopted in Ref. [28,32], which reads as

$$V_{\text{sc}}(r) = 1.387 k_B T (r/\delta)^{-12}, \quad (2.5)$$

with $\delta = (\sigma + 2\sigma/\sqrt{f} + R_g)/2$. The size asymmetry is expressed through the ratio $\xi = \tau/\sigma < 1$.

2.2.2 Fluid Structure in Dilute Star Solutions

In order to determine the pair structure of the mixture we have solved the *two-component* Ornstein-Zernike equation with hypernetted chain (HNC) closure [16, 33] for given sets of physical parameters $(f, \xi; \rho_s, \rho_c)$, obtaining thereby the radial distribution functions $g_{ij}(r)$ and the structure factors $S_{ij}(q)$. In order to maintain contact with currently available experimental samples, we have considered three different values of the star functionality $f = 73, 122$, and 270 , as well as two different values of the size ratio $\xi = 0.3$ and 0.5 . The density ρ_s was always kept within the dilute regime, $\rho_s \sigma^3 \ll 1$, whereas ρ_c was varied at wish.

Selected results for the star-star structure factors $S_{\text{ss}}(q)$ are shown in Fig. 2.1. Upon the addition of a small amount of chains, the star system displays weakened correlations, as witnessed by the drop of the height of the main peak of $S_{\text{ss}}(q)$ and the virtual disappearance of the second one. However, as ρ_c further increases, a new feature shows up: the structure factor develops a double-peak structure with two peaks that correspond to two independent length scales: whereas a 'particle peak' shows up at $q_2 \sigma \cong 6$, a 'cluster peak' appears at much smaller wave-numbers, $q_1 \sigma \cong 2$, the position of which changes with chain density. In fact, as ρ_c grows, the latter peak moves to lower q -values, indicating the growth of the cluster size

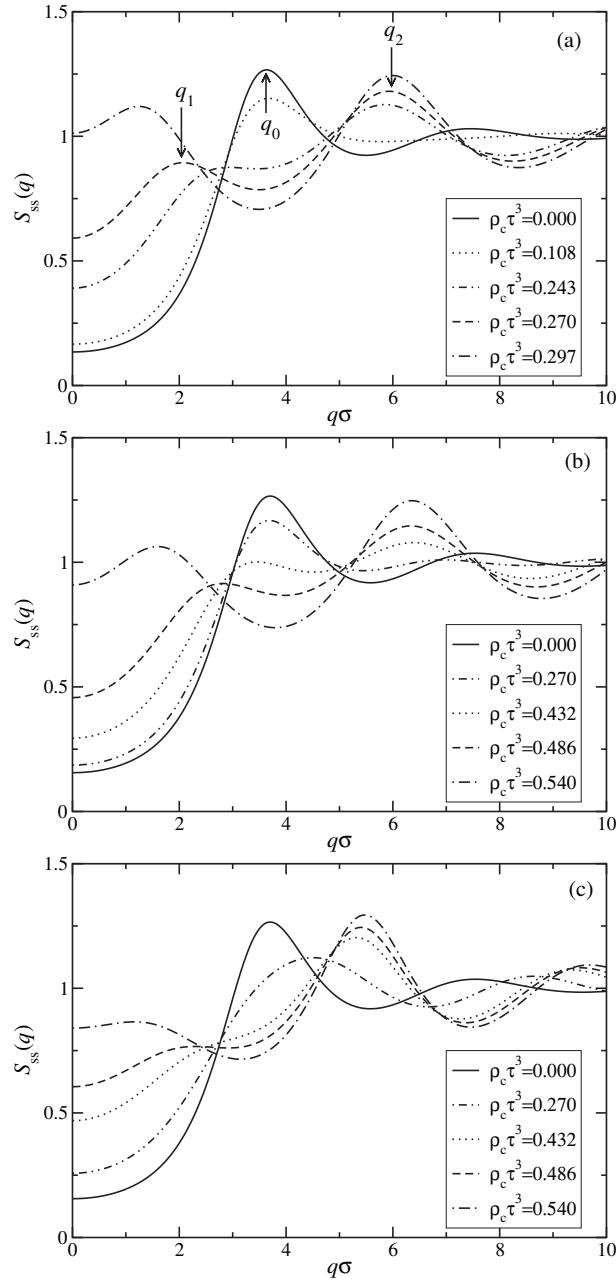


Figure 2.1: Star-star structure factors $S_{ss}(q)$ for star polymers at density $\rho_s \sigma^3 = 0.1$ and chain densities $\rho_c \tau^3$ as indicated in the legends, for different star functionalities f and chain-to-star size ratios ξ . (a) $f = 73$, $\xi = 0.3$; (b) $f = 122$, $\xi = 0.3$; (c) $f = 122$, $\xi = 0.5$. The arrows in (a) denote the cluster-peak position q_1 and the particle-peak position q_2 introduced in the text, whereas the peak position q_0 for the chain-free star solution is also marked for comparison.

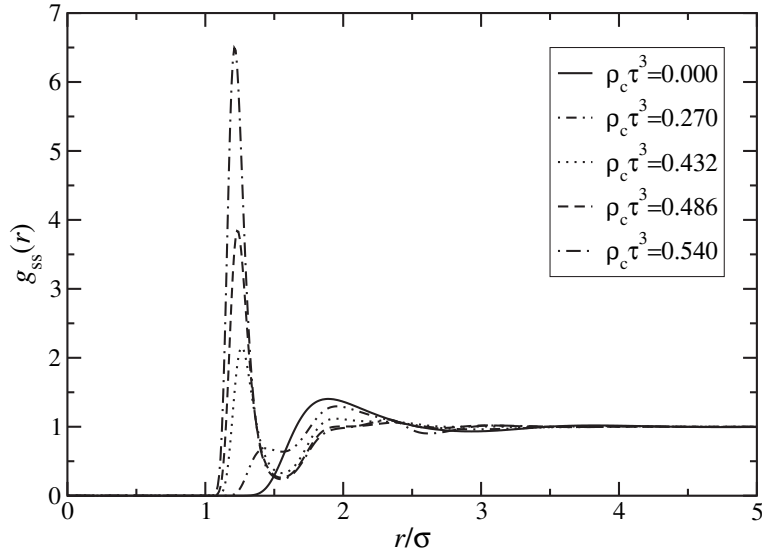


Figure 2.2: The star-star radial distribution function $g_{ss}(r)$ at $\rho_s \sigma^3 = 0.1$ and chain densities $\rho_c \tau^3$ as indicated in the legend. Here $f = 122$ and $\xi = 0.3$.

(and the concomitant intercluster separation). Eventually, at sufficiently high chain densities, the peak moves towards $q = 0$ and a spinodal line, $S_{ss}(q = 0) \rightarrow \infty$, is reached. The double-peak structure factor is strongly reminiscent of features present in model systems for which the development of clusters has been detected, both in experiment [32,34,35] and in theory [35–42]. We will return to a comparison between our system and some of these models at the end of this section.

Comparing now the quantitative features of Figs. 2.1(a)-(c), we see that the occurrence of a double peak (and thus of the clusters) takes place at lower chain densities for $f = 73$ than for $f = 122$, at fixed size ratio $\xi = 0.3$. In fact, for star functionality $f = 270$, which we also examined, we did not find any clustering phenomena. Moreover, the interparticle distance within the clusters, r_m , which is given roughly as $r_m \cong 2\pi/q_2$, has a dependence both on f and on ξ . Comparing Figs. 2.1(a) and (b) we see that, for fixed ξ , the particles within the clusters come somewhat closer to each other as f increases. On the other hand, by comparing the position of q_2 between Figs. 2.1(b) and (c) we see that, for fixed f , an increase in ξ leads to a concomitant increase of the particle separation within the clusters, witnessed by the significant shift of q_2 to the left. Otherwise, the position of q_2 is rather insensitive on the value of the density ρ_c of the additives: clusters are formed and grow in size upon increasing ρ_c but, otherwise, the particle-particle distance within a cluster is not influenced by the chain concentration.

Fig. 2.2 shows the evolution of the radial distribution function $g_{ss}(r)$ of the stars

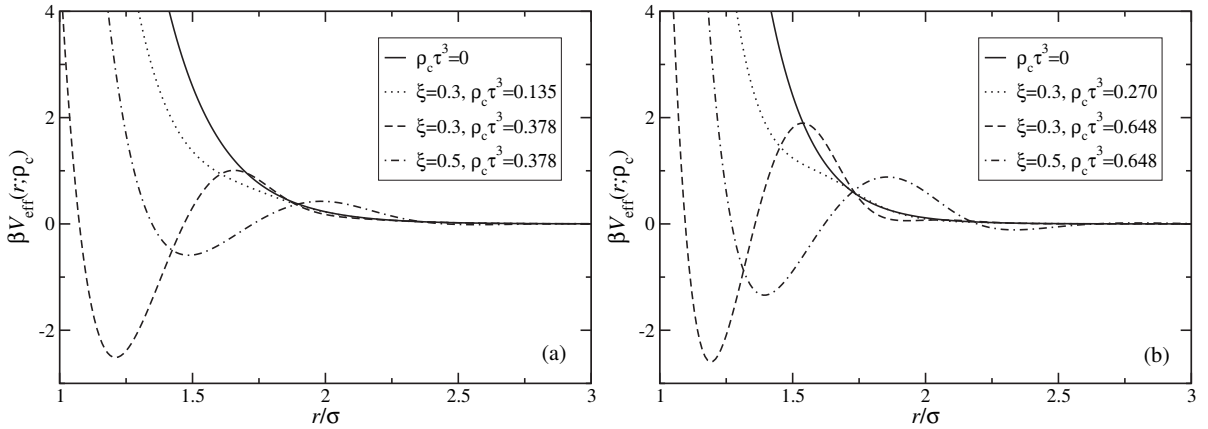


Figure 2.3: The chain-induced star-star effective interaction $V_{\text{eff}}(r; \rho_c)$ for various chain densities, as indicated in the legends. (a) $f = 73$; (b) $f = 122$. The size ratios ξ are also shown in the legends.

upon chain addition for the same parameter combination as in Fig. 2.1(b). The initial ‘softening’ of the star-star repulsion and the subsequent accumulation of stars are witnessed by the ‘leaking-in’ of $g_{\text{ss}}(r)$ and the development of an increasingly high peak at $r \gtrsim \sigma$, respectively. Note that, in agreement with the interpretation given above, the peak *position* is hardly affected by ρ_c ; it corresponds to the length scale r_m introduced above. On the other hand, the integral below the peak, which gives the cluster size, does grow upon increase of ρ_c .

2.2.3 Chain-Mediated Effective Interaction

The formation of clusters as well as the trends regarding their size and stability depending on f and ξ can be rationalized through the concept of the effective star-star interaction *in the presence* of the chains, $V_{\text{eff}}(r; \rho_c)$. This quantity is derived from the stars’ radial distribution function $g_{11}(r)$ through

$$V_{\text{eff}}(r; \rho_c) = - \lim_{\rho_s \rightarrow 0} \ln g_{\text{ss}}(r; \rho_s, \rho_c) \quad (2.6)$$

and includes all the effects from the chains through its dependence on the chain density ρ_c . In the absence of chains, we have $V_{\text{eff}}(r; \rho_c \rightarrow 0) = V_{\text{ss}}(r)$. In Fig. 2.3 we show characteristic results for this quantity for different values of f , ξ and ρ_c . Whereas for small values of ρ_c the effect of the chains is just a reduction of the repulsion strength of the interaction, upon sufficient increase of ρ_c a ‘well-and-shoulder’ form of the effective interaction arises. The attractive well is a typical depletion effect and is caused by the osmotic pressure of the chains surrounding two

stars that are sufficiently close to each other, so that polymer chains are excluded from the inter-star space. The repulsive shoulder is a feature arising from the chain interactions and correlations, as the latter become crowded in the inter-star region for larger inter-star distances, a phenomenon also known from asymmetric hard sphere mixtures [43].

2.2.4 Experimental Findings

Stiakakis *et al.* [32, 44] have also performed experiments employing mixtures of $f = 122$, regular 1,4-polybutadiene stars with homopolymer chains of size ratio $\delta = 0.4$. Dynamic light scattering experiments yielded the intermediate scattering function $C(q, t)$ which was analyzed via an inverse Laplace transform, determining the characteristic relaxation times through the peak distribution of the same [45]. Such measurements allow for the independent determination of both the hydrodynamic radius and the radius of gyration of the dissolved objects for any given chain density. Indeed, the relaxation peaks resulting from the self-diffusion of the stars (slow) and the collective diffusion of the chains (fast) are well-separated in time, allowing for the identification of two distinct relaxation processes in the system. Calling $\Gamma(q)$ the q -dependent inverse decay time associated with the stars, the self-diffusion coefficient D_{star} of the same was calculated as $D_{\text{star}} = \Gamma(q)/q^2$ and the Stokes-Einstein relation yielded the star hydrodynamic radius. On the other hand, the integrated intensity under the peak gives the *static* scattering intensity $I(q)$ from the stars, allowing then for a determination of the gyration radius R_g through a Guinier fit for the cluster-free case and by a Debye-Bueche fit in the clustered phase [46].

Both methods yielded identical results regarding the dependence of the radii on ρ_c . In Fig. 2.4 we show the result for R_g . There is an initial shrinkage of the stars, caused by the osmotic pressure of the chains and lasting up to a concentration $c_{\text{lin}}/c_{\text{lin}}^* \cong 0.4$, where c_{lin}^* denotes the overlap concentration of the chains. Thereafter, a rapid increase of R_g was measured with growing chain concentration, pointing to the development of clusters with R_g as large as 10 times the value of an isolated star. After a period of several weeks, the clusters did not grow in size, suggesting their equilibrium nature. These trends are in agreement with the theoretical predictions.

2.2.5 Cluster Formation in Other Systems

Cluster formation has been recently observed in protein solutions and charged colloid-polymer mixtures [34]; their stability was attributed to the presence of an effective potential with a short-range attraction and a long-range repulsion. The presence of *both* an attractive well and a repulsive shoulder is very common in the

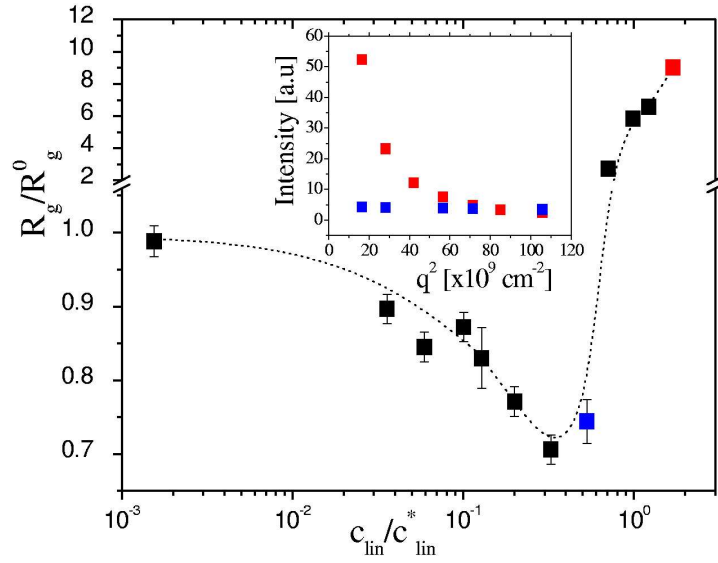


Figure 2.4: The ratio R_g/R_g^0 of the measured star radius of gyration over its value at zero chain concentration in a dilute star solution containing linear chains, plotted against the concentration of the latter. Here, c_{lin} denotes the weight fraction of linear chains with c_{lin}^* standing for the value of this quantity at the chains' overlap concentration. Inset: the measured scattering intensity at the blue and red points. Notice the dramatic increase of the latter at low scattering wave vectors q at the red point, indicating the presence of clusters in the system. Figure courtesy of E. Stiakakis.

formation of finite, stable clusters. Indeed, in a number of recent works effective potentials of this kind have been employed in order to explain the emergence of mesoscopic structures (clusters or stripes) in soft matter. However, Mladek *et al.* [47] also observed the formation of clusters for bound potentials which are purely repulsive. Sear and Gelbart worked with a hard-sphere potential, dressed by the superposition of two ‘Kac-tail’, long-range interactions, one attractive, causing the well, and one repulsive, giving rise to the shoulder [36]. Sciortino *et al.* introduced an effective potential consisting of a superposition of a generalized $n - 2n$ Lennard-Jones potential and a long-range Yukawa repulsion [37, 38], finding the formation of spherical or linear clusters, depending on parameter values. Liu *et al.* investigated the structural properties of double Yukawa (attractive/repulsive) fluids, finding macrophase separation or cluster formation, depending on the relative strength of the attractive and repulsive parts [39], whereas Imperio and Reatto employed a model similar to that of Ref. [36] and discovered cluster- and stripe formation in two dimensions [40, 41]. Also two dimensional mixtures of superparamagnetic colloids were investigated in two dimensions [35, 42]. Also in this system aggregation of particles into clusters was observed. The physics behind the cluster stability lies in the tendency of the attractive well to cause particle aggregates, whose size is thereafter limited by the repulsive barrier that prevents the growth of an infinite cluster. In this respect, the particle separation within the clusters, r_m , is set by the minimum in the effective potential $V_{\text{eff}}(r; \rho_2)$. This explains the observation that q_2 decreases (r_m grows) as ξ increases, cf. Fig. 2.3(b) with Figs. 2.1(a) and (b). Moreover, the fact that cluster formation is easier at fixed ρ_c for smaller ξ , can be understood if one takes into account that, for given $\rho_c \tau^3$, the number density of the small stars is larger for smaller ξ , i.e., $\rho_c \sigma^3 = \rho_c \tau^3 / \xi^3$. Hence, the smaller- ξ chains can bring about a higher osmotic pressure that leads to cluster formation. Without the barrier, the system would be driven to phase separation without the occurrence of clusters, i.e., $S_{\text{cc}}(q)$ would develop a peak at $q = 0$ and not at finite q -values [36]. Note, however, that the presence of clusters does *not* exclude macroscopic phase separation. Whereas one can choose the potential parameters in such a way that a binodal is completely eliminated or strongly suppressed [36–38], one can have situations in which a binodal line is preceded by a region of stability of finite clusters, as found by Liu *et al.* in their study of the double-Yukawa system [39]. Here, we find a similar scenario, in which cluster formation is followed by indications of a macroscopic phase separation, i.e., star-chain demixing, witnessed by the drifting of the cluster peak towards $q = 0$ as ρ_c is increased. Due to lack of experimental samples, the chain concentration could not be increased beyond the values quoted here. On the basis of the theoretical analysis, a macrophase separation is expected upon further increase of ρ_c . The theoretical investigation of this question is left for future studies. However, we will address the related questions on the influence of the added chains on the gelation and vitrification properties of the stars in the following sections. We will

now abandon the purely heuristic approach taken until now and will base our study on an effective interaction derived in theoretical modeling of the star and chain and confirmed by extensive monomer-resolved computer simulations.

2.3 Star-Star and Chain-Chain Interactions

In the following sections we perform an accurate calculation of the effective interactions used to model the mixture of star polymers and chains. In this way, we extend and improve the model presented in Sec. 2.2.1.

The question that arises is which coordinates should be chosen as effective ones. For the star polymers, and in particular in the case of high functionality f , the position of their central particle, on which all chains are grafted, is the natural one. The corresponding effective interaction V_{ss} has been derived a long time ago [17, 18] and its validity has been confirmed through extensive comparisons with scattering data [18, 24] and computer simulations [29]. It is the same interaction as we use in Eq. (2.3). We quote it again for the sake of completeness [18]:

$$\beta V_{ss}(r) = \frac{5}{18} f^{3/2} \begin{cases} -\ln\left(\frac{r}{\sigma_s}\right) + \frac{1}{1 + \sqrt{f}/2} & \text{for } r \leq \sigma_s; \\ \frac{1}{1 + \sqrt{f}/2} \frac{\sigma_s}{r} \exp\left[-\frac{\sqrt{f}}{2\sigma_s}(r - \sigma_s)\right] & \text{else.} \end{cases} \quad (2.7)$$

Again, σ_s is the corona diameter of the star. The distance $\sigma_s/2$ marks the crossover between the inner part of the macromolecule, where the latter resembles a semidilute polymer solution and the outer part, in which loose chains form a local, dilute solution [18]. The Yukawa part of the interaction decays with the characteristic length $2\sigma_s/\sqrt{f}$, set by the diameter of the outermost star blob [15]. Monomer-resolved computer simulations have shown that the relation $\sigma_s \cong 4/3 R_g^{(s)}$ holds, where $R_g^{(s)}$ is the radius of gyration of the star polymer.

The choice of the effective coordinate for the linear chains is less obvious. At least three possibilities have been employed repeatedly in the literature. Witten and Pincus [17] considered the coordinate of the end-monomer as an effective one that characterizes the whole chain. In computer simulations [31, 48–54] and field-theoretical approaches [48] the polymer's center of mass is an oft-used coordinate, resulting into a Gaussian effective interaction of strength $\sim 2k_B T$ and range set by the chain's radius of gyration, $R_g^{(c)}$. This approach was also employed by us in Sec. 2.2.1. Finally, another alternative is given by choosing the central monomer as an effective coordinate, a choice that is more symmetric than that of the end-monomer [48, 55]. The latter choice establishes a certain symmetry between multiarm star polymers and linear chains, since a chain of polymerization N_c now becomes equivalent to a

star of functionality $f = 2$ and polymerization $N_c/2$ per arm. Accordingly, this is the choice we follow in the next sections. In this representation, the effective interaction between the polymer chains has been calculated by theory and simulation in Ref. [55]. The interaction energy between two polymer chains as a function of the distance r between their central monomers is given by:

$$\beta V_{\text{cc}}(r) = \frac{5}{18} 2^{3/2} \begin{cases} -\ln\left(\frac{r}{\sigma_c}\right) + \frac{1}{2\alpha^2\sigma_c^2} & \text{for } r \leq \sigma_c; \\ \frac{1}{2\alpha^2\sigma_c^2} \exp[-\alpha^2(r^2 - \sigma_c^2)] & \text{else.} \end{cases} \quad (2.8)$$

As for multiarm stars the scale σ_c satisfies the relation $\sigma_c \cong 4/3 R_g^{(c)}$ [55]. The parameter α is given by $\alpha\sigma_c = 1.03$, a choice that guarantees the correct value of the second virial coefficient of a polymer solution [55]. The similarity between high- f ($f \gtrsim 10$) stars and linear chains ($f = 2$) is manifest by comparing the interactions of Eqs. (2.7) and (2.8). Both feature a logarithmic divergence for close approaches, scaling with the prefactor $(5/18)f^{3/2}$. This feature arises from general scaling considerations, as it will be demonstrated shortly. However, the type of decay for larger separations is different: a Yukawa-type decay holds for multiarm stars, whereas a Gauss-type decay is valid for linear chains. The physical reason for this difference lies in the fact that high- f stars feature geometric blobs in their exterior, which arise from the crowding of the f chains in a sphere. The size of the outermost blob sets the scale for the decay of the Yukawa part of the potential [18]. Such blobs are absent in linear chains and the interaction decays in a different way, which is much better modeled by a Gaussian [55].

Evidently, it remains to specify the cross-interaction $V_{\text{sc}}(r)$ in order to have a full, mesoscopic description of the mixture. In Refs. [28, 32, 44] and Sec. 2.2, in which star-chain mixtures have also been considered, the approach of using the chain's center of mass as effective coordinate has been adopted. Accordingly, the chain-chain interaction was modeled by a Gaussian [31], and for the cross-interaction a heuristic power-law form with additive length scale was assumed. That modeling led to a satisfactory description of experimental observations. Here, however, we aim at a realistic modeling of the cross interaction and thus a more detailed analysis is necessary, also in view of the fact that a different effective coordinate (the central monomer) is used to coarse-grain the linear polymer. This is the subject of the following section.

2.4 Star-Chain Interactions

2.4.1 Molecular Dynamics Simulations

One strategy leading to the determination of the unknown interaction $V_{cs}(r)$ is to employ computer simulations. These also serve as a stringent test for theoretical approximations. Computer simulations are, at the same time, limited by the degree of polymerization N and the star functionality f that can be simulated. For this purpose, we limited ourselves to moderate values of these parameters and subsequently compared the simulation results with those from theory. The maximum number of monomers of the star in the simulations is 5000. The excellent agreement between the two allows us then to apply the theoretical approach to arbitrary star functionalities.

We performed Molecular Dynamics (MD) simulations in which each monomer is resolved and calculated the effective force $\mathbf{F}_{sc}(r)$ acting on the star center in the presence of a chain whose own central monomer is held at distance r from the former; clearly, $\mathbf{F}_{cs}(r) = -\mathbf{F}_{sc}(r)$ and the relation to $V_{sc}(r)$ reads as

$$\mathbf{F}_{sc}(r) = -\frac{\partial V_{sc}(r)}{\partial r} \hat{\mathbf{r}}, \quad (2.9)$$

where we position the star at the origin and the mid-monomer of the chain at $\mathbf{r} = r\hat{\mathbf{r}}$. The simulation model employed is the same used in various previous studies of star polymers and polymer chains [29, 56]. In order to mimic good solvent conditions, all monomers interact with each other via a purely repulsive and truncated Lennard-Jones potential, namely

$$V_{LJ}(r) = \begin{cases} 4\epsilon \left[\left(\frac{\sigma_{LJ}}{r} \right)^{12} - \left(\frac{\sigma_{LJ}}{r} \right)^6 + \frac{1}{4} \right] & \text{for } r \leq 2^{1/6} \sigma_{LJ}; \\ 0 & \text{else.} \end{cases} \quad (2.10)$$

Here, σ_{LJ} is the monomer size and ϵ sets the energy scale. As in previous simulations [29], we use $k_B T = 1.2\epsilon$. The monomer mass m is also taken as unitary, setting thereby the time scale of the MD simulation as $\tau_{MD} = \sqrt{m\sigma_{LJ}^2/\epsilon}$. Connected monomers along each star arm and along the chain experience an additional bonding interaction, expressed by the finite extensible nonlinear elastic potential (FENE):

$$V_{FENE}(r) = \begin{cases} -15\epsilon \left(\frac{R_0}{\sigma_{LJ}} \right)^2 \ln \left[1 - \left(\frac{r}{R_0} \right)^2 \right] & \text{for } r < R_0; \\ \infty & \text{else,} \end{cases} \quad (2.11)$$

where $R_0 = 1.5\sigma_{LJ}$.

f	N_s	N_c	$R_g^{(s)}/\sigma_{LJ}$	$R_g^{(c)}/\sigma_{LJ}$	σ_s/σ_{LJ}	σ_c/σ_{LJ}	R_d/σ_{LJ}
20	50	40	11.6	4.36	15.46	5.82	0.5
35	50	40	12.6	4.36	16.8	5.82	0.5
50	100	200	20.2	11.9	27	15.8	0.5
100	50	200	15.1	11.9	20.1	15.8	0.8

Table 2.1: List of the parameters of the simulated systems. The corona diameters σ_α ($\alpha = s, c$) were taken to be $4/3$ of the respective radii of gyration, $R_g^{(\alpha)}$, as discussed in the text.

Due to the high monomer concentration in the center of the star, a hard core with radius R_d is introduced [29]. The interaction between the core and the monomers is the same as between the monomers, but shifted by a distance R_d of microscopic order; all parameters are summarized in Table 2.1. The effective force $\mathbf{F}_{sc}(r)$ above is then simply the average over all microscopic forces acting on the center of the star [16, 29]. We simulated four different pairs consisting of one star and one chain; the parameter combinations are given in Table 2.1. The equations of motion were integrated using a time step $\Delta t = 2 \times 10^{-3} \tau_{MD}$. For every different separation r , the system was first equilibrated during 10^6 time steps and up to an additional 5×10^7 time steps were used to gather the statistics. During equilibration, we couple the system to a heat bath [49] that acts as a thermostat, which is switched off at the end of equilibration time. A typical simulation snapshot is shown in Fig. 2.5. The results from the MD simulations will be discussed in what follows, in conjunction with the theoretical modeling.

2.4.2 Theory of the Star-Linear Effective Interaction

In developing a theoretical approach for the unknown quantity $V_{sc}(r)$, two different regimes for the interparticle separation r must be considered. When the two are sufficiently close together, $r \lesssim (\sigma_s + \sigma_c)/2$, analytical considerations from scaling theory can be employed. We denote this range of separations as the *scaling regime*, whereas the domain $r \gtrsim (\sigma_s + \sigma_c)/2$ defines the *weak overlapping regime*.

1. *The scaling regime.* In the scaling regime, we can invoke arguments from scaling theory [57]. The partition function \mathcal{Z}_1 of a linear chain with N monomers scales as

$$\mathcal{Z}_1(N) \sim z^N N^{-\nu\eta_2}, \quad (2.12)$$

where the fugacity z is a quantity depending on microscopic details but the Flory exponent $\nu \cong 3/5$ and the exponent η_2 are universal for all polymers in good solvent

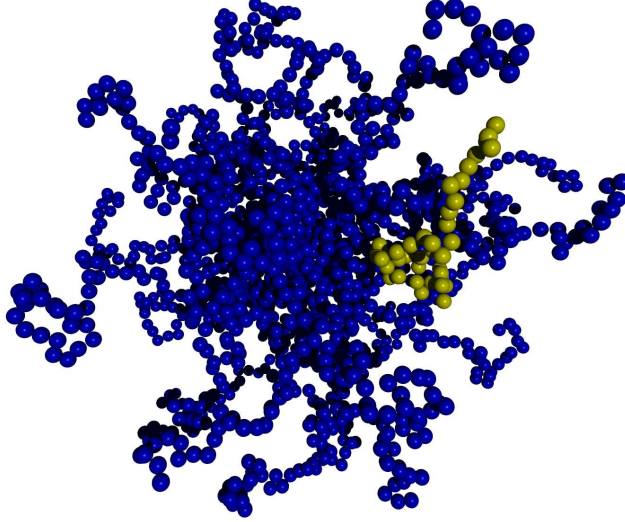


Figure 2.5: Simulation snapshot of a star polymer with $f = 35$ arms and $N_s = 50$ monomers (dark beads) per chain and a linear chain with $N_c = 40$ monomers (light gray beads) at a center-to-center distance $r = 10 \sigma_{LJ}$.

conditions. Eq. (2.12) above can be generalized to f -arm stars and reads as

$$\mathcal{Z}_f(N) \sim z^{fN} N^{\nu(\eta_f - f\eta_2)}, \quad (2.13)$$

with the family of exponents η_f being known from renormalization group analysis and simulations [58] and scaling as $\eta_f \sim -f^{3/2}$ for $f > 1$. Note that Eqs. (2.12) and (2.13) above immediately imply that $\eta_1 = 0$. At the same time, it can be seen that a linear chain can be simultaneously seen as a star with $f = 1$ arm and N monomers (end-monomer representation) or as a star with $f = 2$ and $N/2$ monomers (mid-monomer representation): the partition functions $\mathcal{Z}_1(N)$ and $\mathcal{Z}_2(N/2)$ have the same N -dependence.

When two stars with different functionalities, f_1 and f_2 are brought to a small separation r of the order of the monomer length a , their partition function takes the form:

$$\mathcal{Z}_{f_1 f_2}(r; N_1, N_2) \sim C_{f_1 f_2}(r) \mathcal{Z}_{f_1 + f_2}(N), \quad (2.14)$$

which reflects the fact that two stars held close together resemble a new star with functionality $f_1 + f_2$. Here N stands for either N_1 or N_2 , supposing that the two are not too dissimilar, so that the radii of the two stars, which scale as N_i^ν can be identified with a single length scale $R \sim N_i^\nu$. When $r \rightarrow \infty$, $\mathcal{Z}_{f_1 f_2}(N_1, N_2)$ factorizes into the partition functions of the individual components, $\mathcal{Z}_{f_1 f_2}(N_1, N_2) = \mathcal{Z}_{f_1}(N_1) \mathcal{Z}_{f_2}(N_2)$.

At the same time, since the monomer length scale is irrelevant for scaling arguments, the only remaining length is the aforementioned star size R . On dimensional grounds, the partition function $\mathcal{Z}_{f_1 f_2}(N_1, N_2)$ must take the form

$$\mathcal{Z}_{f_1 f_2}(r; N_1, N_2) \sim B_{f_1 f_2}(r/R) \mathcal{Z}_{f_1} \mathcal{Z}_{f_2}, \quad (2.15)$$

with some unknown function $B_{f_1 f_2}(r/R)$. Taking into account Eq. (2.13) above, Eqs. (2.14) and (2.15) imply that

$$B_{f_1 f_2}(r/R) \sim N^{-\nu \theta_{f_1 f_2}}, \quad (2.16)$$

with

$$\theta_{f_1 f_2} = \eta_{f_1} + \eta_{f_2} - \eta_{f_1 + f_2}. \quad (2.17)$$

Taking into account the scaling $R \sim N^\nu$, we see that Eq. (2.16) can be fulfilled only if the function $B(z)$ is a power law of z : $B(z) \sim z^{\theta_{f_1 f_2}}$. Finally, Eq. (2.15) is written as:

$$\mathcal{Z}_{f_1 f_2}(r; N_1, N_2) = \left(\frac{r}{R}\right)^{\theta_{f_1 f_2}} \mathcal{Z}_{f_1} \mathcal{Z}_{f_2}. \quad (2.18)$$

Combined with the definition of the effective interaction, Eq. (2.1), the last equation gives the asymptotic behavior of $V_{f_1 f_2}(r)$ for small r as $\beta V_{f_1 f_2}(r) \sim -\theta \ln(r/R)$. Inserting the scaling $\eta_f \sim -f^{3/2}$, we obtain therefore

$$\beta V_{f_1 f_2}(r) = -\alpha \left[(f_1 + f_2)^{3/2} - \left(f_1^{3/2} + f_2^{3/2} \right) \right] \ln \left(\frac{r}{R} \right) + K, \quad (2.19)$$

with some unknown constants α and K . The constant α can be fixed by requiring that $V_{f_1 f_2}$ reduces to Eq. (2.7) in the case $f_1 = f_2 = f$. Thereby, we obtain

$$\beta V_{f_1 f_2}(r) = -\Theta_{f_1 f_2} \ln \left(\frac{r}{R} \right) + K, \quad (2.20)$$

where

$$\Theta_{f_1 f_2} = \frac{5}{36} \frac{1}{\sqrt{2} - 1} \left[(f_1 + f_2)^{3/2} - \left(f_1^{3/2} + f_2^{3/2} \right) \right]. \quad (2.21)$$

Eq. (2.20) above is the expression that we adopt for small star-chain separations, setting $f_1 = f$ and $f_2 = 2$. It remains to specify what is meant by ‘short’. The scaling argument above holds for separations r of the order of the monomer length. However, monomers of length a can be regrouped into effective ones with increased length, $a \rightarrow \lambda a$, provided one simultaneously rescales the polymerization, $N \rightarrow \lambda^{-1/\nu} N$, thereby increasing the range of validity of the asymptotic regime. Clearly, this procedure can be carried until the rescaled monomer length has reached a size of the order of the gyration radius. We expect, thus, Eq. (2.20) to hold for $r \lesssim R$, and

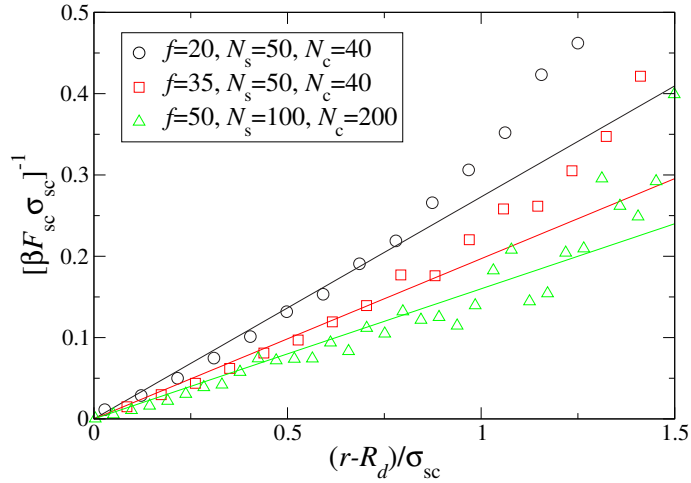


Figure 2.6: The inverse force $F_{cs}(r) = \hat{\mathbf{r}} \cdot \mathbf{F}_{cs}(r)$ [see Eq. (2.9)] between stars of different functionalities and chains of different lengths, as indicated in the legend. The symbols denote simulation results, shifted by the star core, whereas the lines are the predictions of the theory according to Eq. (2.22). The slope in the linear part is in agreement with the theoretical description but the scaling breaks down for separations $r > \sigma_{sc}$.

in the following we will test this assumption. A consequence of Eq. (2.20) is that the force $F_{cs}(r) = \hat{\mathbf{r}} \cdot \mathbf{F}_{cs}(r)$ [see Eq. (2.9)] takes the form:

$$\beta F_{sc} = \frac{\Theta_{f2}}{r}, \quad (2.22)$$

implying that the inverse force scales linearly with r .

In Fig. 2.6 we show a comparison of the results from the computer simulations and scaling theory regarding the inverse force. It can be seen that the scaling regime holds up to a separation $\sigma_{sc} = (\sigma_s + \sigma_c)/2$, i.e., the cross-diameter for the logarithmic interaction is additive. Thus, we write the star-chain effective potential as

$$\beta V_{sc}(r) = -\Theta_{f2} \ln \left(\frac{r}{\sigma_{sc}} \right) + \bar{K} \quad \text{for } r \leq \sigma_{sc}, \quad (2.23)$$

with an additive constant \bar{K} to be fixed later. It remains, thus to determine the interaction in the weak overlapping regime, $r > \sigma_{sc}$.

2. *The weak overlapping regime.* For large separations between the star center and the central monomer of the chain, we use a Flory-type approach, which has been shown to yield accurate results for dendritic macromolecules [59,60]. The interaction energy between the star and the chain is now estimated by a simple overlap integral

between the *undisturbed* density profiles of the two objects. This is justified, since we use this theoretic approach only for large distances. We assume that the density profiles are the profiles of the two objects for an infinite separation. Thus, $V_{sc}(r)$ reads as

$$\beta V_{sc}(r) = \beta \iint d^3r' d^3r'' c_s(r') c_c(|\mathbf{r}'' - \mathbf{r}|) v(|\mathbf{r}' - \mathbf{r}''|). \quad (2.24)$$

Here, $c_s(r)$ and $c_c(r)$ are the density profiles of the star and chain, respectively, and $v(r)$ is the monomer interaction. The interaction between the monomers is approximated by a δ -function [61–63]:

$$\beta v(|\mathbf{r}' - \mathbf{r}''|) = v_0 \delta(\mathbf{r}' - \mathbf{r}''), \quad (2.25)$$

where v_0 has the dimension of a volume and is called excluded volume parameter. Using this interaction in Eq. 2.24 we obtain

$$\beta V(r) = v_0 \int d^3r' c_s(r') c_c(|\mathbf{r}' - \mathbf{r}|). \quad (2.26)$$

The modeling of the density profile of the star polymers is based on the considerations in Ref. [55]. According to the blob model of star polymers by Daoud and Cotton [15], for sufficiently long arms the largest part of the star is in good solvent conditions and the monomer density follows a power-law:

$$c_s(r) \sim r^{-4/3}. \quad (2.27)$$

The length $\sigma_s/2$ is the distance from the star center up to which the scaling Eq. (2.27) holds. Outside of this region there is a layer of free rest chains. In Ref. [55], it was found that the local osmotic pressure in the outer region takes the form

$$\Pi(r) \propto \left(\frac{1}{r^2} + 2\kappa^2 \right) \frac{\zeta}{\sigma_s} \exp \left\{ -\kappa^2 [r^2 - (\sigma_s/2)^2] \right\}, \quad (2.28)$$

where κ is a fit parameter of the order $1/R_g^{(s)}$ and

$$\zeta = \frac{1}{1 + \kappa^2 \sigma_s^2 / 2}.$$

In this outer region, the monomer density is very low and the region can be locally seen as a dilute polymer solution. Therefore, $c \propto \Pi$ and the resulting density profile of a single star is then given by

$$c_s(r) = A \begin{cases} r^{-4/3} (\sigma_s/2)^{-5/3} & \text{for } r \leq \sigma_s/2 \\ \left(\frac{1}{r^2} + 2\kappa^2 \right) \frac{\zeta}{(\sigma_s/2)} \exp \left\{ -\kappa^2 [r^2 - (\sigma_s/2)^2] \right\} & \text{else.} \end{cases} \quad (2.29)$$

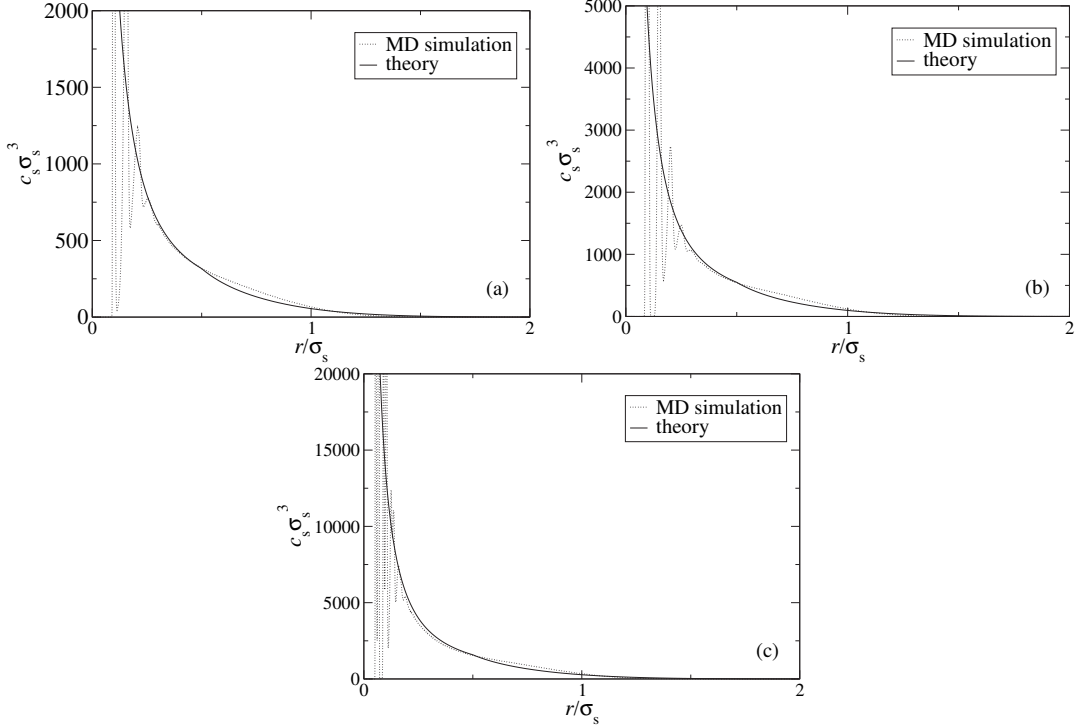


Figure 2.7: The monomer density profiles $c_s(r)$ of three different star polymers. Each panel shows a comparison of the the simulation results and the theoretical modeling according to Eq. (2.29). (a) $f = 20$, $N_s = 50$; (b) $f = 35$, $N_s = 50$; and (c) $f = 50$, $N_s = 100$.

The profile is continuous at $r = \sigma_s$. The prefactor A is determined by the mass conservation condition:

$$N_s f = \int d^3 r c_s(r). \quad (2.30)$$

Eq. (2.29) above satisfies known conditions from scaling theory. First, since $A \propto f$ and $\sigma_s \sim a f^{1/5}$, for fixed N_s , it yields $c_s(r) \propto r^{-4/3} f^{2/3}$ for $r < \sigma_s$. Subsequently, the relation $\Pi \propto c^{9/4}$ in the semidilute regime formed in the star interior yields $\Pi(r) \propto r^{-3} f^{3/2}$ there.

In Fig. 2.7 we show a comparison between the theoretical model for the star density profiles and the simulation results. There is a single fitting parameter, namely κ , which must be of the order of $1/R_g^{(s)}$. Indeed, the fits shown in Fig. 2.7 were achieved for a value $\kappa R_g^{(s)} = 0.95$ for all three cases. Subsequently, we employ this value for all stars modeled in the theory. Apart from a region close to the grafting core, in which the local steric-induced ordering of the monomers causes oscillations in the density profile, the agreement is good. Notice, in any rate, that

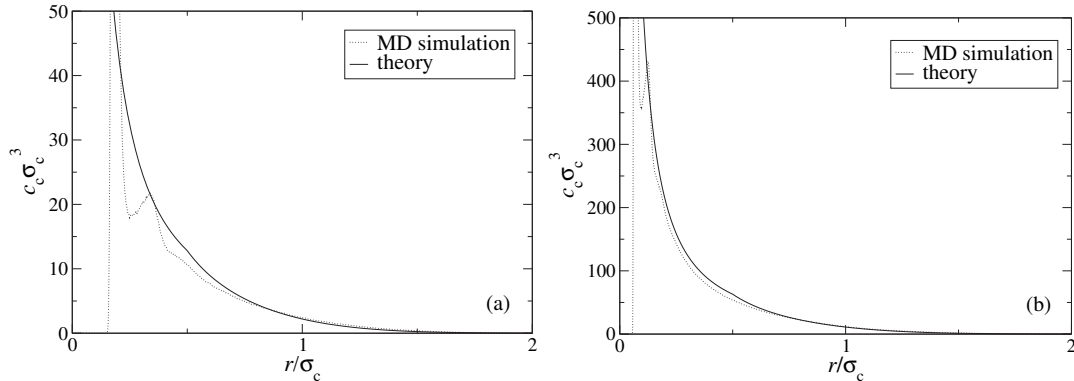


Figure 2.8: The monomer density profiles $c_c(r)$ of two different polymer chains. Each panel shows a comparison of the the simulation results and the theoretical modeling. (a) $N_c = 40$; (b) $N_c = 200$.

f	N_s	N_c	$v_0\sigma_{LJ}^3$
20	50	40	0.957
35	50	40	0.955
50	100	200	0.445
100	50	200	0.546

Table 2.2: List of the parameters of the simulated systems. The excluded volume parameter v_0 is determined by the condition that the force be continuous at $r = \sigma_{sc}$.

we are going to make use of the profiles only in their outermost domain, since the interaction for short distances is given by the scaling form, Eq. (2.23).

For the linear polymer chains, we model the profile $c_c(r)$ around the mid-monomer in the same way as for the stars, since in the inner region theory again predicts a $r^{-4/3}$ -scaling [64, 65], and in the outer region we expect some exponential decay. Only the normalization condition changes and reads now as

$$N_c = \int d^3r c_c(r). \quad (2.31)$$

Again $\kappa R_g^{(c)} = 0.95$ was employed. The comparison of the model and the simulation data is shown in Fig. 2.8.

Using these density profiles, we can now calculate effective interactions between the two macromolecular objects for $r > \sigma_{sc}$. Note that the only remaining free parameter in the theory is the excluded volume parameter v_0 . This, along with the additive constant \bar{K} in Eq. (2.23), is uniquely determined by the constraints that

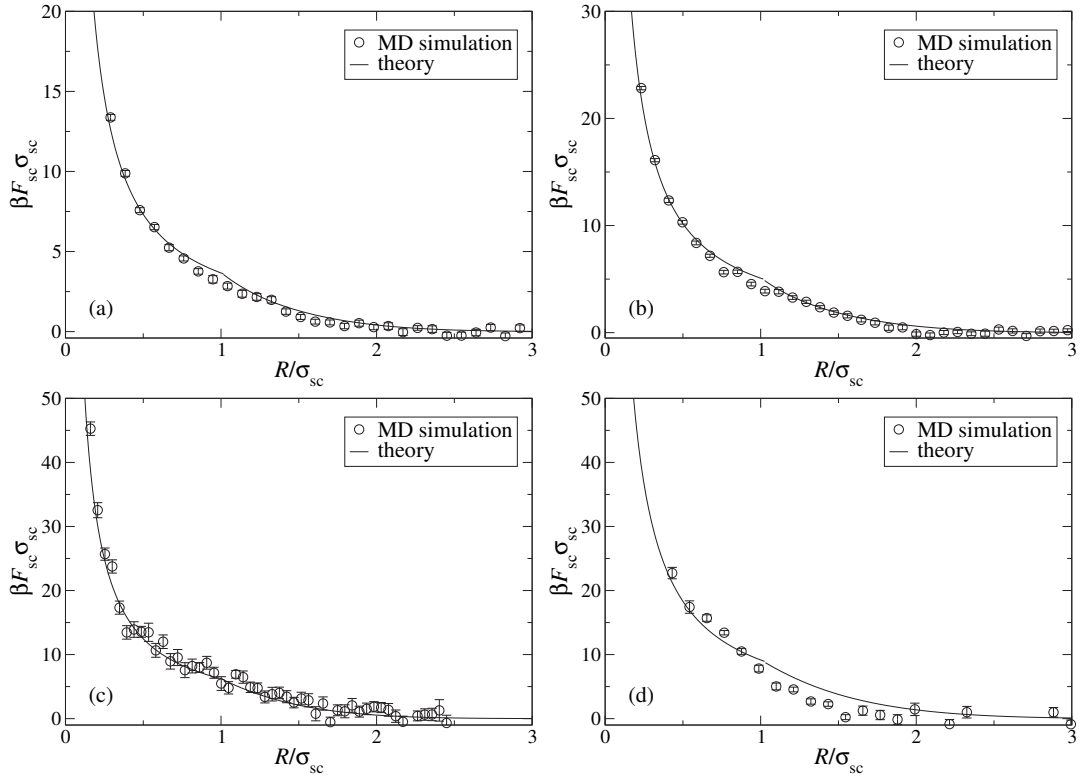


Figure 2.9: Mean force between the star and chain as a function of the distance of the star and chain center. The circles denote the simulation results, the solid line the results from the theoretic modeling. The force is calculated for (a) $f = 20$, $N_s = 50$, $N_c = 40$; (b) $f = 35$, $N_s = 50$, $N_c = 40$; (c) $f = 50$, $N_s = 100$, $N_c = 200$; and (d) $f = 100$, $N_s = 50$, $N_c = 200$.

both the interaction $V_{\text{sc}}(r)$ and its first derivative with respect to r be continuous at the matching point $r = \sigma_{\text{sc}}$. The resulting values for v_0 are shown in Table 2.2. In Fig. 2.9 we show the comparisons between the effective forces obtained in the MD simulations and the ones resulting from the above theoretical modeling, for which the force is given by Eq. (2.9). It can be seen that for the first three combinations, there is excellent agreement between the two whereas for Fig. 2.9(d) the agreement is still good. It should be pointed out, however, that for a star with $f = 100$ and $N = 50$ there is an inner region with strongly stretched monomers and that the size ratio with the associated chain is $\xi = 0.8$ (see Table 2.1), which is larger than the size ratios $\xi \leq 0.5$ considered in this work. Therefore, the predictions of scaling theory are not expected to be very accurate in this case. The agreement between theory and simulations for the parameter combinations considered gives confidence in the theoretical modeling of the profiles and the associated effective interaction.

We now need to provide a general scheme for the consistent calculation of $V_{\text{sc}}(r)$ for arbitrary functionalities f and size ratios ξ , defined as

$$\xi = \frac{\sigma_{\text{c}}}{\sigma_{\text{s}}}.$$

Here, a difficulty arises at first, since, in a mesoscopic description, the degrees of polymerization N_{s} and N_{c} of the star and the chain should drop out of sight and they should enter the effective interactions solely through the dependence of the scales $\sigma_{\text{s,c}}$ on them, namely [14, 61]:

$$\sigma_{\text{s}} \sim f^{1/5} N_{\text{s}}^{3/5} \quad (2.32)$$

and

$$\sigma_{\text{c}} \sim N_{\text{c}}^{3/5}. \quad (2.33)$$

At the same time, *explicit* values for $N_{\text{s,c}}$ are required for the normalization conditions of the density profiles. It appears that one obtains, then, different effective interactions for different $N_{\text{s,c}}$ values at fixed ξ and f . The problem, however, is only an apparent one and it is removed because the part of the effective interaction for $r < \sigma_{\text{sc}}$ provides a strong constraint. One may choose some arbitrary (large) value for N_{s} and subsequently determine *uniquely* the corresponding value of N_{c} from the given size ratio ξ and Eqs. (2.32) and (2.33) above. Using these scaling relations and calculating the convolution integral from Eq. (2.26) above, one finds that the effective interaction $V_{\text{sc}}(r)$ in the region $r > \sigma_{\text{sc}}$ scales proportionally to $\tilde{v} = v_0 N_{\text{s}}^{1/5}$ and that the remaining factor depends only on the scaled separation $x = r/\sigma_{\text{sc}}$. This expression, and its derivative, have to be matched with Eq. (2.23), valid in the strong overlap region, at $x = 1$. The latter, however, depends exclusively on x , without any additional dependence on N_{s} . Therefore, \tilde{v} turns N_{s} -independent. This property gives a $N_{\text{s}}^{-1/5}$ -dependence on v_0 , which shows that the latter should

not be interpreted literally as the true monomer-monomer excluded volume but rather as a parameter that allows the smooth crossover from the scaling- to the weak-overlapping regimes. To put it differently: one can assume just *any* degree of polymerization for the star. The scaling expression, Eq. (2.23), will then force the effective interaction to lose any explicit dependence on N_s also in the *outside* region, as long as it is expressed in terms of the scaled variable $x = r/\sigma_{sc}$, as should indeed be the case. The only dependence of the interaction on N_s and N_c enters implicitly through the dependence of the length scales σ_s , σ_c , and $\sigma_{sc} = (\sigma_s + \sigma_c)/2$ on these quantities, see Eqs. (2.32) and (2.33) above.

2.5 The Many-Body Problem

Having now obtained the star-star, star-chain and chain-chain effective interactions, we can turn our attention to finite mixture concentrations, employing for the coarse-grained description of the mixture the effective potential energy function of Eq. (2.2). The associated physical parameters are the star functionality f as well as the chain-to-star size ratio ξ ; the relevant thermodynamic parameters are the two partial densities $\rho_\alpha = \mathcal{N}_\alpha/\Omega$, $\alpha = c, s$, where $\mathcal{N}_{c,s}$ denote the numbers of stars and chains, respectively, enclosed in the macroscopic volume Ω . For the calculation of the pair structure, the sought-for quantities are the corresponding partial distribution functions $g_{\alpha\beta}(r)$ or, equivalently, the partial structure factors $S_{\alpha\beta}(k)$, defined as [33]

$$S_{\alpha\beta}(k) = \delta_{\alpha\beta} + \sqrt{\rho_\alpha\rho_\beta} \int d^3r [g_{\alpha\beta}(r) - 1] \exp(-i\mathbf{k} \cdot \mathbf{r}). \quad (2.34)$$

The distribution functions have been calculated by employing standard tools from integral equation theory. In particular, we solved the two-component Ornstein-Zernike equation [16, 33] complemented with the Rogers-Young closure [66].

2.5.1 Mixtures at Low Star Concentrations

1. Chain-modified star-star interaction. We can make one more step in the coarse-graining process and integrate out the linear chains, describing thereby the system as an effective, one-component star solution. In this way, the star-star interaction $V_{ss}(r)$ gets renormalized and a higher-level effective interaction between the stars, $V_{\text{eff}}(r)$ arises, which depends on f , the size ratio ξ , and, most importantly, the chain concentration ρ_c . In this way, we can gain insight into the ways of modifying the behavior of a concentrated star solution by changing any of the above characteristics of the mixture. The quantity $V_{\text{eff}}(r)$ can be obtained within the framework of two-component integral equations. Starting from the radial distribution function in the

limit of infinite dilution of star polymers, the effective interaction between them in the presence of polymer chains is given by [67]

$$V_{\text{eff}}(r; \rho_c) = - \lim_{\rho_s \rightarrow 0} \ln g_{\text{ss}}(r; \rho_s, \rho_c). \quad (2.35)$$

and depends parametrically on the (reservoir) density of the linear chains.

In Fig. 2.10 we show the dependence of the effective interaction on the properties of the added polymer, taking now a typical experimental functionality $f = 73$ as a representative. It is instructive to see how different the effect of the linear additives is depending on the size ratio ξ . For $\xi = 0.1$, Fig. 2.10(a), the addition of polymer chains leads first to a weakening of the repulsion between the stars, until a strong depletion attraction is induced. Notice that the chain density in the legend is expressed in units of the chain size; it lies well below its overlap value but it is nevertheless large when expressed in units of the star size, as it gets multiplied by a factor ξ^{-3} . An attractive part develops, which is due to the osmotic pressure of the many small chains pushing the two stars together, a *depletion* phenomenon well-known also from the case of colloid-polymer mixtures. This attraction is devoid of any significant secondary maximum (hump) at larger separations and can lead to a star-chain demixing transition. In the intermediate region of size ratios, $\xi = 0.3$, shown in Fig. 2.10(b), the resulting interaction displays a competition of short range attractions and long range repulsions, which lead to the formation of finite equilibrium clusters, to be discussed below. Here, the presence of the repulsive hump plays the decisive role in stabilizing the multistar aggregates [32, 44].

An unusual feature develops for the case of the largest size ratio considered, $\xi = 0.5$, shown in Fig. 2.10(c). The chains bring about no attraction between the stars, only a reduction of the repulsion range. The striking effect, however, lies in the fact that beyond the overlap density of the chains, $\rho_c^* \sigma_c^3 \approx 1$, the interaction remains virtually unchanged by the addition of more chains. The phenomenon is unknown for the usual cases of colloid-polymer or colloid-colloid depletion, for which the effective potential has a strong dependence on the depletant density [16]. Here, it seems that the effect of the chains saturates when they reach their overlap density and that this feature is present only when the chains have a size comparable to that of the stars. The novelty arises from the soft nature of the cross-interaction potential, $V_{\text{sc}}(r)$, as opposed to the hard interactions encountered in colloid mixtures and can be traced back to the increased penetration of the chains into the stars as their density grows.

To provide an independent check on this phenomenon and to understand better the role of the penetrability, we have calculated the depletion force between the stars using an alternative approach, the superposition approximation [68]. The geometry is shown in Fig. 2.11. Let the star on the left be placed at the origin and a second star be at separation \mathbf{r} from the first. The two are immersed in a solution of linear

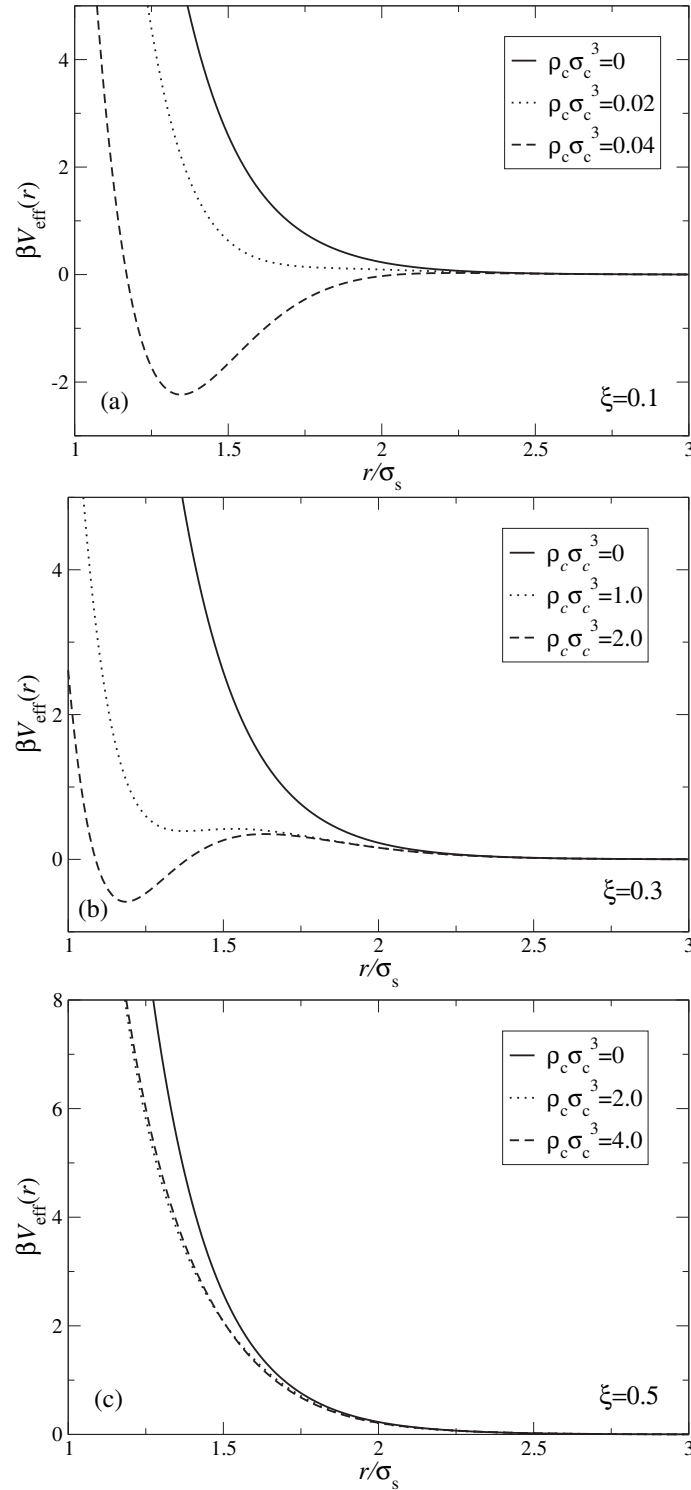


Figure 2.10: Effective interaction between the stars modified by the presence of the chains. The functionality is $f = 73$ in all cases, the size ratio is indicated in the figure.

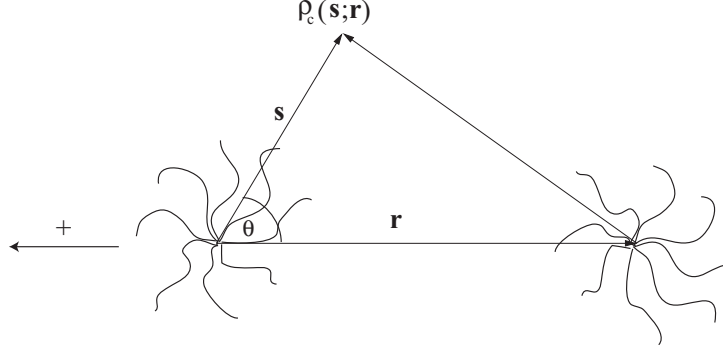


Figure 2.11: The geometry of two stars, separated by the vector \mathbf{r} and being immersed in a sea of linear chains (not drawn). The star on the left is positioned at the origin. At the point described by the position vector \mathbf{s} , the chain density is $\rho_c(\mathbf{s}; \mathbf{r})$, where the second argument indicates its dependence on the star separation \mathbf{r} . The arrow denotes the direction along which the effective force acting on the star on the left is chosen as positive.

chains and the local chain density at position \mathbf{s} is $\rho_c(\mathbf{s}; \mathbf{r})$, depending parametrically on the star-star separation. We consider the chain-mediated force acting on the star at the origin, which we call *depletion force*, $\mathbf{F}_{\text{dep}}(r)$; it is positive if it repels the two stars and negative otherwise. With this convention, we consider now the quantity $F_{\text{dep}}(r) = -\hat{\mathbf{r}} \cdot \mathbf{F}_{\text{dep}}(r)$, which is given by

$$F_{\text{dep}}(r) = -2\pi \int_0^\infty r^2 \frac{dV_{\text{sc}}(r)}{dr} \int_{-1}^1 \rho_c(\mathbf{r}; \mathbf{R}_1, \mathbf{R}_2) \omega d\omega dr, \quad (2.36)$$

where $\omega = \cos \theta$. In the superposition approximation, the chain density $\rho_c(\mathbf{s}; \mathbf{r})$ is decomposed as a product of the radial distributions of two isolated stars, shifted by the distance \mathbf{r} , i.e.,

$$\rho_c(\mathbf{s}; \mathbf{r}) = \rho_c g_{\text{sc}}(s) g_{\text{sc}}(|\mathbf{s} - \mathbf{r}|). \quad (2.37)$$

With this approximation we obtain

$$F_{\text{dep}}(r) = -2\pi \int_0^\infty h(r, s) ds, \quad (2.38)$$

where

$$h(r, s) = \rho_c s^2 \frac{dV_{\text{sc}}(s)}{ds} g_{\text{sc}}(s) f(r, s) \quad (2.39)$$

and

$$f(r, s) = \int_{-1}^1 g_{\text{sc}}(\sqrt{r^2 + s^2 - 2rs\omega}) \omega d\omega. \quad (2.40)$$

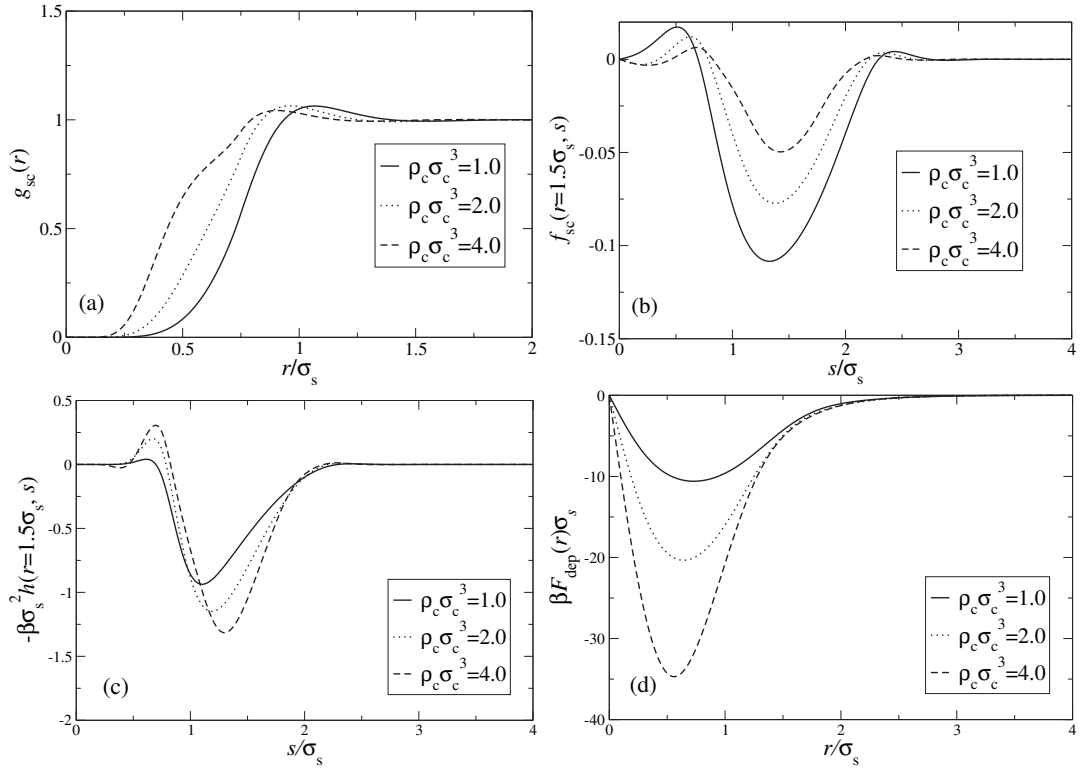


Figure 2.12: (a) The star-linear cross-distribution function $g_{sc}(r)$ for $f = 73$, $\xi = 0.5$, star density $\rho_s = 0$ and chain densities as indicated in the legend; (b) The function $f(r; s)$ of Eq. (2.40) at $r = 1.5\sigma_s$; (c) The function $\rho_c h(r, s)$ defined in Eq. (2.39) for $r = 1.5\sigma_s$; (d) The full depletion force in the superposition approximation. Note the insensitivity to ρ_c for $r > 1.5\sigma_s$.

In Fig. 2.12 we show the individual terms that are involved in $F_{\text{dep}}(r)$, in order to gain some insight into the mechanism that leads to the insensitivity of the depletion force and thus of the effective one, since the latter is the sum of the depletion force and the direct star-star force. When functions of the two variables r and s are shown, we fix the inter-star separation to the value $r = 1.5\sigma_s$, for which, according to Fig. 2.10(c), $V_{\text{eff}}(r)$ hardly changes with ρ_c , and we plot the functions against the integration variable s .

The angularly averaged radial distribution $f(r = 1.5\sigma_s, s)$, Fig. 2.12(b) is strongly dependent on depletant density. Interestingly, though, it is most negative for the lowest density and its magnitude decreases for increasing density. The reason for this behavior lies in the penetrability of $g_{\text{sc}}(r)$ shown in Fig. 2.12(a). Due to the additional presence of the ω -term in the integrand, the function $f(r, s)$ would vanish identically if the function $g_{\text{sc}}(z)$ were equal to unity for all z . An increase in ρ_c and the concomitant penetration inside the soft core, pushes g_{sc} precisely in this direction and causes $f(r, s)$ to decrease in magnitude.

This decrease is compensated again upon multiplication with ρ_c and $g_{\text{sc}}(s)$, which yield the function $h(r, s)$ [Eq. (2.39)] shown in Fig. 2.12(c). Indeed, the three curves for the three different densities integrate to very similar values. Again, a partial role is played by the multiplication of $f(r, s)$ with $g_{\text{sc}}(s)$, which penetrates deeper into the star when ρ_c increases without developing any pronounced correlation structure. These are the signatures of the ultrasoft cross-interactions, thus this phenomenon is absent for the depletion force between impenetrable colloids. Finally, in Fig. 2.12(d), we show the resulting depletion force from the superposition approximation. In full consistency with the results from the inversion of $g_{\text{ss}}(r; \rho_s, \rho_c)$ [Eq. (2.35)], there is hardly any variation with ρ_c for $r \gtrsim 1.5\sigma_s$ when $\rho_c\sigma_c^3 \gtrsim 1$. Note that the depletion force *does* change with ρ_c for smaller separations, yet this effect is masked by the direct force $F_{\text{ss}}(r) = -dV_{\text{ss}}(r)/dr$, which is much larger in magnitude than the depletion force at such length scales.

It is tempting to associate this phenomenon with a worsening of solvent quality for the stars as chains are added. Once the latter have reached and exceeded their overlap concentration, the solvent has reached the vicinity of the Θ -point and hence the stars feel the effective interaction akin to Θ -like conditions. Further increase of the chain concentration within the semidilute regime does not bring about any additional change of solvent quality, hence the effective interaction does not change any more. It is intriguing that the coarse-grained description may be able to reproduce such a behavior and further investigations are needed to explore a possible deeper connection with the classical theory of polymers. Our findings may explain, however, the experimentally observed insensitivity of the behavior of star polymer gels upon addition of linear chains, when the chain-star size ratio exceeds, roughly, the value 0.5, see Ref. [28].

2. *Cluster formation.* An interesting phenomenon taking place in star-linear

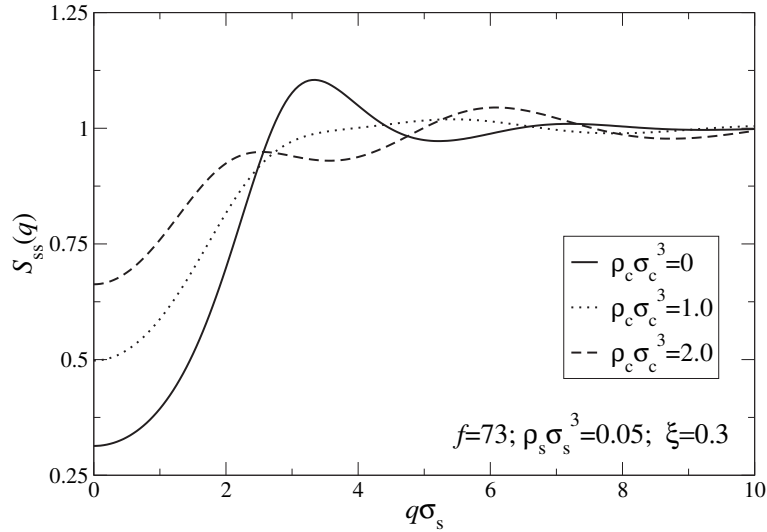


Figure 2.13: The star-star structure factor $S_{ss}(q)$ at different chain concentrations for star functionality $f = 73$. The star number density is kept constant at $\rho_s \sigma_s^3 = 0.05$.

mixtures at very low concentrations, is that of cluster formation between the stars, when the added chains approach or exceed their overlap concentration [32, 44]. The results of our previous heuristic approach are confirmed by our study employing the realistic potential we derived. For a discussion of cluster formation in other systems see Sec. 2.2.5.

Here, we employ the accurate cross-interaction $V_{sc}(r)$, along with the other two interactions, $V_{ss}(r)$ and $V_{cc}(r)$, to investigate the existence and stability of star clusters due to the added chains. In this way, we improve over previous studies that employed a heuristic cross-interaction in the center-of-mass representation [32, 44]. In order to investigate cluster formation, we examine the star–star structure factor of the system. We probe the dependence of the cluster formation on the star functionality and the size ratio between the stars and the added polymers. The presence of clusters is signaled by the appearance of a new length scale in the star–star structure factor that is larger than the typical star–star separation $a_s = \rho_s^{-1/3}$.

In Fig. 2.13 we show the development of the structure factor at *fixed* star density $\rho_s \sigma_s^3 = 0.05$ on increasing the chain concentration for a star functionality $f = 73$ and a chain-to-star size ratio $\xi = 0.3$. Upon increasing ρ_c , the peak height first decreases and shifts to larger q , then the peak splits and a new peak at small q appears. The length scale which is associated with this value is much larger than the size of the individual stars, therefore we associate this length scale with the formation of equilibrium clusters in the system. Eventually, for even higher chain concentrations,

the maximum in the structure factor will shift to $q = 0$, signaling the approach of a macroscopic phase separation for large polymer densities. Note that the equilibrium clusters, as signaled by the development of a prepeak in the star-star structure factor, appear when the chains reach their overlap concentration, in agreement with experimental measurements [44]. The organization of the stars into aggregates is in agreement with the characteristics of the effective star-star interaction shown in Fig. 2.10(b). Indeed, for this particular size ratio, $\xi = 0.3$, $V_{\text{eff}}(r)$ displays a short-range attraction, followed by a repulsive hump. The rather weak prepeak in the structure factor points to the existence of fluctuating clusters, which exchange particles, as opposed to a cluster phase with tightly bounded supramolecular aggregates. For small size ratios, e.g., $\xi = 0.1$, the effective interaction is devoid of a repulsive hump, see Fig. 2.10(a), and thus the system is driven into macrophase separation that is not preceded by the appearance of stable clusters with a well-defined size. For higher ξ -values, the chains do not induce any attraction between the stars, see Fig. 2.10(c), thus again no clusters appear. These facts demonstrate that cluster formation is very sensitive on the physical characteristics of the constituents and can be steered by external control of the size ratio, for instance.

2.5.2 Mixtures for High Star Concentrations

Finally, here we turn our attention to a physical situation that is specular to the one discussed in the preceding subsection, namely high star concentration and low chain concentration. Also in this case, the chains can have a dramatic impact in the behavior of the dense star solution. It is known that high functionality star polymers undergo a dynamical arrest transition at a certain critical density ρ_s^{cr} , roughly at $\rho_s^{\text{cr}} \sigma_s^3 \cong 0.4$. This structural arrest, seen in rheological [25,26,69] and light scattering experiments [32], has also been investigated theoretically within the framework of mode-coupling theory [27] (MCT) based on the interaction potential $V_{\text{ss}}(r)$. For details of the method see Appendix B. The arrest can be identified with a glass transition that arises from the mutual repulsions between stars that lead to caging, i.e. the stars cannot diffuse due to being blocked by their neighbors. Accordingly, it is absent for functionalities $f \lesssim 50$, for which the interstar repulsion of Eq. (2.7) is not strong enough to sustain self-supporting cages.

The influence of multiarm star additives on this soft colloidal glass has been investigated for binary star polymer mixtures [70]. As far as the effect of linear additives is concerned, experimental studies of star polymer-linear chains mixture find a chain induced melting of the star polymer glass, which is caused by a softening of the star-star repulsion [28]. Here, we investigate the phenomenon applying the accurate cross-interaction potential $V_{\text{sc}}(r)$. Already the information encoded in Fig. 2.10 points to the fact that the additives should have the effect of melting the star glass. Indeed, they bring about invariably a reduction of the interstar repulsion,

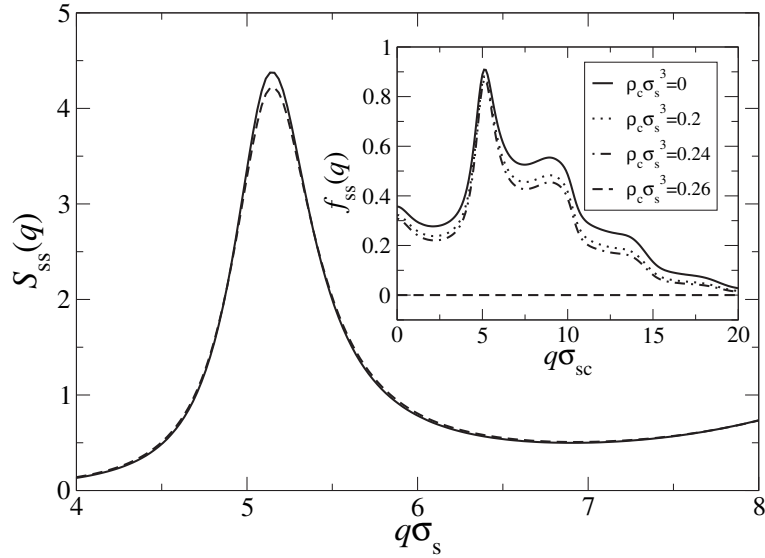


Figure 2.14: Main plot: the star-star structure factor for $f = 122$ -arm stars at density $\rho_s\sigma_s^3 = 0.4$. Solid line: no added chains, $\rho_c\sigma_c^3 = 0$. Dashed line: with added chains of size ratio $\xi = 0.3$ and density $\rho_c\sigma_c^3 = 0.26$. Note the small but clear decrease of the height of the main peak. Inset: the star-star nonergodicity factor $f_{ss}(q)$ for the same mixture, at fixed star concentration $\rho_s\sigma_s^3 = 0.4$ and increasing chain density as indicated in the legend. Below the threshold value $\rho_c\sigma_c^3 = 0.26$, the nonergodicity factor is finite, corresponding to an arrested state, whereas at $\rho_c\sigma_c^3 = 0.26$, $f_{ss}(q) = 0$, denoting restoration of ergodicity.

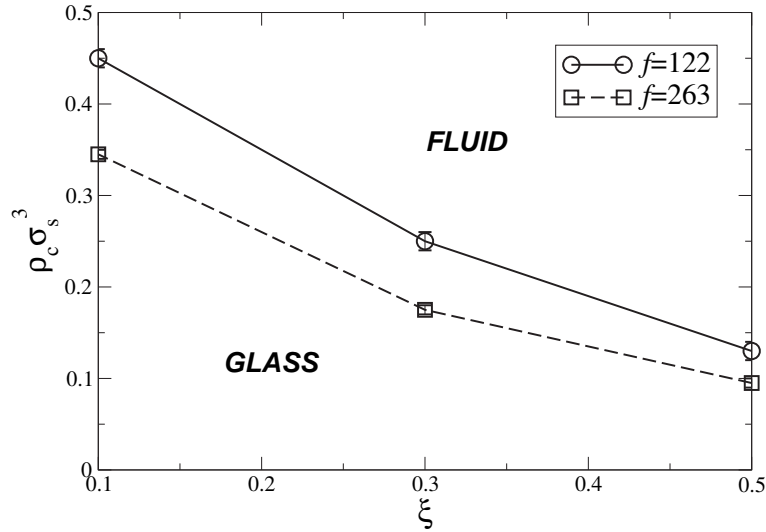


Figure 2.15: Ideal MCT transition lines for star polymers with $f = 122$ and $f = 263$. Here, the star densities are fixed at $\rho_s \sigma_s^3 = 0.4$ for $f = 122$ and $\rho_s \sigma_s^3 = 0.35$ for $f = 263$. The points denote the density of chains that is needed to reach the non-ergodic-to-ergodic transition as a function of the size ratio. The lines are a guide to the eye. Above the line corresponding to each f the system is fluid and below glassy.

due to a classical depletion effect. In this way, the stars, in the presence of the linear polymer, become more penetrable and this leads to a reduction of both the interstar correlations and the peak height in the star-star structure factor $S_{ss}(q)$. This can be seen in the main plot of Fig. 2.14, which shows a characteristic example for $S_{ss}(q)$ of $f = 122$ -arm stars at density $\rho_s \sigma_s^3 = 0.4$, slightly above the critical glass concentration. There is a small reduction of the peak height upon addition of chains, which is nevertheless sufficient to cause restoration of ergodicity, since we are right at the brink of the ergodic-to-non-ergodic transition.

To study the dynamics and vitrification in this system, we employ ideal mode coupling theory [3, 71]. Assuming that the polymer remains mobile in the mixture, we can base our analysis on one-component MCT, using only the structure factors of the stars as input [70, 72]. The object of main interest from MCT is the star-star nonergodicity factor $f_{ss}(q)$, which expresses the $t \rightarrow \infty$ limit of the density time-autocorrelation function. Thus, $f_{ss}(q) = 0$ for an ergodic state in which all density fluctuations decay exponentially in time but $f_{ss}(q) \neq 0$ for an ideal glass. The inset of Fig. 2.14 shows the evolution of the nonergodicity factor upon addition of chains and manifests the transition from a glassy to an ergodic state at some critical chain concentration. A compilation of MCT-results for various parameter combinations

is finally show in Fig. 2.15. This represents a kinetic phase diagram of the system, as obtained by ideal MCT, and again manifests the influence of the composition of the mixture on the dynamics of the system. The basic trends are in agreement with the experimental findings in Ref. [28], as well as comparable to the behavior for binary star polymer mixtures when the small component remains mobile in the matrix formed by the big one [70]. The chain number density required to melt the glass decreases with increasing size ratio ξ . The glass melting of the stars can be interpreted as a worsening of the solvent quality for the stars upon addition of the chains [73].

2.6 Conclusions

We have derived accurate effective interactions between star polymers of functionality f and linear homopolymer chains. The latter have been coarse-grained in the mid-monomer representation, a choice that renders them equivalent to $f = 2$ -stars with half the degree of polymerization per arm. Together with the previously derived star-star and chain-chain interactions, this allows for a full, coarse-grained description of star-linear polymer mixtures and the calculation of the static pair structure of the system. To the extent that statics dictates also dynamical arrest, as in the case of the MCT-scenario for the glass transition, the coarse-grained description also allows for predictions regarding the rheological state of the mixture and the influence of the chains on the flow of the stars. We have confirmed a host of phenomena observed experimentally, such as cluster formation and glass melting, by using this accurate representation. It is rewarding that this approach does not alter the results obtained previously, when the chains were coarse-grained in the center-of-mass representation and a more empirical form of the cross-interaction was used to describe the vitrification [28] and cluster formation [32, 44] (see Sec. 2.2). In this respect, the results of this work are compatible with the requirement that the choice of the effective coordinates should not change the physics of the problem at hand, although, of course, it alters the form of the effective interactions employed. The equivalence of the physical results is only guaranteed, however, when the employed effective interactions do not involve too drastic approximations, i.e., when they capture the physics of the system correctly. A similar equivalence of the center-of-mass vs. mid-monomer representations was recently established for colloid-polymer mixtures [74]. Moreover, since we not only changed the effective coordinate but also the theoretic approach for the interactions was improved, we note that the two different approaches yield qualitatively similar physical properties of the system. Cluster formation and polymer induced melting are general phenomena that do not depend very sensitively on the modeling of the interactions employed.

A very useful tool that arises out of a second coarse-graining procedure is the

chain-modified star-star effective interaction potential. In this work, we established that the form of the latter strongly depends on size ratio. It can feature attractive wells with or without subsequent repulsive humps or it can differ only slightly from the bare star-star interaction as the size ratio grows. The present work deals with good and athermal solvents. A question of great interest is the coarse-grained description of star-linear mixtures in marginal or even Θ -solvents. Experimental results on such systems suggest that, once more, the size ratio of the mixture plays a crucial role [73]. For small size ratios, the chains penetrate into the innermost part of the stars, thereby effectively *improving* solvent quality, an effect opposite to that in good solvents. For large size ratios, however, the chains cause star shrinking [73]. It is a challenging task to attempt a coarse-graining procedure for the case of marginal solvents and to investigate the systematic differences with the good-solvent effective interactions and their ability to describe the experimental findings of Ref. [73].

Chapter 3

Binary Star Polymer Mixtures: Dynamical Phase Behavior

In this chapter, we examine the rheological transition from an arrested to a fluid state for different mixtures of star polymers with varying functionality and size ratios. As a general trend, we find that addition of smaller star polymers in an arrested, concentrated solution of larger ones brings about melting of the large star glass. At the same time, the dependence of the amount of additives needed to melt the glass has a nontrivial dependence on the size ratio. Theoretical analysis, based on effective interactions and mode coupling theory, reproduces the experimental results and helps identify two distinct types of glasses in the composite system.

3.1 Introduction

Perhaps the most spectacular changes of the rheological state of a fluid are those encountered in the neighborhood of the *glass transition*, in which the many-body system runs into a state of *dynamical arrest*. Although dynamical arrest has no visible signature in the *structural* properties of the system, its dynamical response (viscosity, viscoelastic moduli etc.) varies by orders of magnitude when external control parameters (temperature or concentration) are changed by tiny amounts. Accordingly, the understanding of the glass transition has been a topic of vivid interest for decades and it has experienced explosive growth in the realm of soft matter physics [75–79]. Here, the ability to molecularly design various colloidal systems and chemically tune their architecture, composition and physical characteristics opens up a wealth of novel scenarios and paths to various arrested states.

Recently, a great deal of attention has been devoted to the study of the glassy states emerging in colloid-polymer (CP) mixtures, the former being hard, spherical colloids and the latter soft fractals. It has been found that the addition of a small

amount of polymer brings about melting of the colloidal glass and, upon increase of the polymer concentration, a new, *attractive* glass re-emerges [10–13] but this phenomenon is restricted to a small range of polymer-to-colloid size ratios [72]. Low-density dynamically arrested states, akin to a colloidal gel, arise when the colloids in the CP-mixture have an additional, long-range repulsion, the phenomenon being intricately connected to the formation of stable *clusters* in the system [37].

A different direction of investigation lies in replacing the hard, glass-forming colloids with softer ones, such as star polymers [14, 16, 25]. The ability to synthesize well-characterized and reasonably monodisperse stars, both in size and in arm number (functionality) has indeed promoted these systems into excellent models for studying the effects of *softness* in the glass formation. Similar to CP-mixtures, it has been found experimentally that the addition of linear homopolymer melts the glass formed by the star polymers with functionality $f_1 = 122$ [28] but the range of size ratios for which this occurs is much broader than in CP mixtures. The theoretic interpretation of this phenomenon has been given in Sec. 2.5.2 The possibilities to tailor the system’s rheology grow even broader when large, glass-forming stars of functionality $f_1 \gg 1$ are mixed with smaller ones with functionality $f_2 < f_1$.

3.2 Experiments

Different mixtures of small and large stars were measured by Vlassopoulos *et al.* [70, 80]. All large stars were synthesized using a dendrimer scaffold [81] or a hydrosilylated 1,2-polybutadiene backbone [82] and chlorosilane coupling chemistry in order to assemble living linear 1,4-polybutadiene arms and form colloidal stars with nominal functionality $f_1 = 128$ or 270. Small stars were synthesized with the dendrimer scaffold technique and yielded nominal $f_2 = 16, 32$ or 64 [83, 84]. Table 3.1 lists the characteristics of the stars used in this study (extracted from [76, 81–84]).

Several asymmetric binary mixtures were prepared. Most mixtures consisted of large stars of nominal $f_1 = 270$ (LS4, LS5 or LS6) at a high fixed concentration (about $1.4c^*$, c^* being the overlapping concentration) in the glassy state (rheological solid); different small stars were added to these glasses, with varying functionality (18, 32, 64) and arm molecular weight (see Table 3.1), at different concentrations. Some mixtures consisted of a large star with nominal $f_1 = 128$, at the same volume fraction as the LS samples, in the glassy state; similarly, different small stars were added to this glass as well.

Preparation of the mixtures involved forming the glassy state of the large star in toluene and adding the small star (under gentle and prolonged stirring, sometimes using excess solvent and subsequently evaporating to the desired concentration); the original glass was therefore ‘broken’ and the mixture was then left still to ‘equilibrate’ for at least 24 hours. Special care was taken to reduce the risk of degradation by

Code	f	M_w (10^6 g/mol)	R_h (nm)
2518	19	0.541	20.0
3718	18	0.762	25.3
3210	31	0.301	11.5
3220	33	0.644	18.8
3237	35	1.33	27.2
3280	34	3.01	44.5
64015	56	0.0741	5.8
6405	57	0.258	12.3
6430	56	1.34	31.2
6460	61	2.89	49.6
LS4	267	4.9	38.3
LS5	269	7.9	50.7
LS6	263	11.2	63.2
12880	122	8.8	64

Table 3.1: Summary of the physical properties of the polybutadiene stars used in the experiments. The last four entries (separated from the rest by the horizontal line) denote the $f \gg 1$ -systems that were kept at their vitrification concentration, whereas the preceding ones denote various stars of lower f and smaller size that were used as additives. Table courtesy of D. Vlassopoulos.

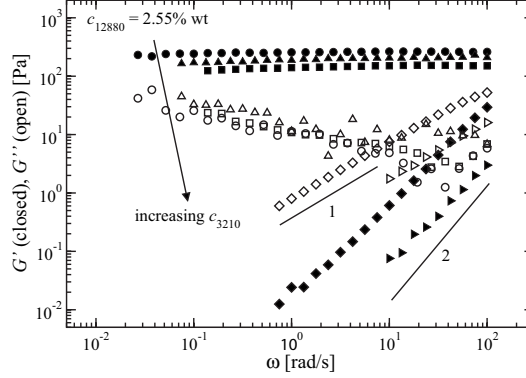


Figure 3.1: Dynamic frequency sweeps depicting the storage G' (closed symbols) and loss G'' (open symbols) moduli as function of frequency for different mixtures consisting of large stars coded 12880 at $c_{12880} = 2.55\%$ wt and small stars coded 3210 at different concentrations: $c_{3210} = 0\%$ (circles); $c_{3210} = 0.066\%$ (triangles up); $c_{3210} = 0.21\%$ (squares); $c_{3210} = 0.50\%$ (diamonds); $c_{3210} = 0.82\%$ (triangles right). Note that for solid samples, $G' > G''$ holds, whereas the opposite is true for fluid ones. Solid lines with slopes 1 and 2 represent the terminal scaling for G'' and G' , respectively. Figure courtesy of D. Vlassopoulos.

adding a small amount of antioxidant [85].

The state of a given sample was investigated with linear rheological measurements; they were carried out with a sensitive strain-controlled rheometer (Rheometric Scientific ARES-HR 100FRTN1). A cone-and-plate geometry (25 mm diameter, 0.04 rad cone angle) was used and the temperature was set at $20 \pm 0.1^\circ\text{C}$ with a recirculating water/ethylene glycol mixture.

A home-made evaporation blocker system was used (with water as the ‘sealant’ fluid in the area between the sample in the cone-plate fixture and an outer ring; water content was controlled and renewed when needed), similar to that reported recently in literature by Sato [86]. Once conditions for reproducible, time-independent and linear measurements were established, small amplitude oscillatory shear measurements were performed in the frequency range 100–0.03 rad/s.

Typical results obtained with a mixture consisting of large stars with $f_1 = 122$ (coded 12880 in Table 3.1), and small stars with $f_2 = 32$ are depicted in Fig. 3.1. In the experiments the storage modulus G' and the loss modulus G'' were determined. It is clear that the large stars exhibit solid-like behavior, since $G' > G''$ and G' is virtually frequency independent. The particular frequency dependence of G'' is

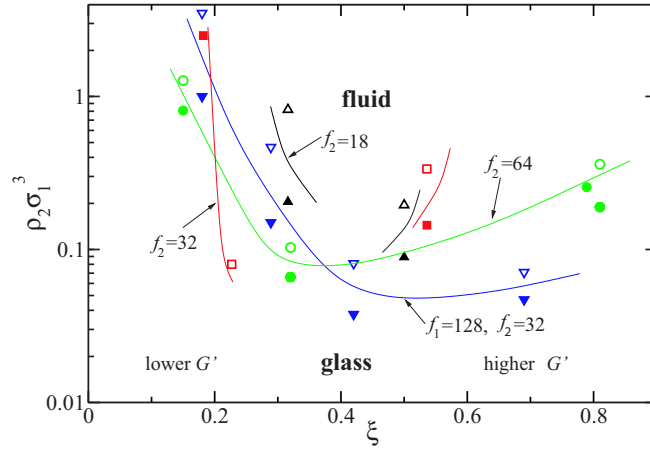


Figure 3.2: Experimental kinetic ‘phase diagram’ of binary star mixtures, indicating regions of liquid and glass for different densities of added small star ρ_2 and size ratios q . Large stars of functionalities $f_1 = 270$ and 128 were used, with densities $\rho_1 \sigma_1^3 = 0.345$ and 0.412 , respectively. Open symbols denote a liquid and closed ones a solid (glass) state. Only the data points closest to the melting lines are shown here. The lines through the data, passing above the full symbols and below the empty ones, are guides to the eye. Figure courtesy of D. Vlassopoulos.

typical for a colloidal glass [87–89]. As we add the small star at constant functionality and molecular weight (sample 3210 in Table 3.1), the glass is weakened with increasing 3210 concentration, as judged by its rheological signal; more specifically, as c_{3210} rises to 0.21% wt, the mixture’s plateau modulus (high-frequency G' limit) decreases substantially, i.e., by 42% with respect to the 12880 value (of 260 Pa); at the same time, the G'' remains virtually unchanged, suggesting that the key effect of the additive is the softening of the cage elasticity of the large stars. Eventually, at $c_{3210} = 0.5\%$ wt, the cage apparently opens up, the glass melts, and the classic viscoelastic liquid response ($G' \sim \omega^2$, $G'' \sim \omega$, $G'' > G'$) is reached. This remarkable finding, and in particular the change of viscoelastic moduli by orders of magnitude upon changing the concentration of the small star (here, basically doubling the concentration), suggests that linear rheological measurements serve as a very sensitive indicator of liquid-to-solid transitions. The same diagnostics has been applied also to determine, e.g., the rheology and dynamics of micellar solutions of block copolymers [90]. Note that the same behavior is observed qualitatively when we keep the concentration of the added small star constant while changing its molecular weight (data are not shown here).

By using the rheological information obtained as outlined above, it is possible to construct a ‘kinetic state’ diagram of density of the added small star against the

ratio of hydrodynamic radii $\xi = R_h^{(\text{small})}/R_h^{(\text{large})}$, number density of the large ones. In this diagram, shown in Fig. 3.2, we map the rheological behavior of the star mixture as we change the additive. One can observe that by increasing the concentration of a given small star, the mixture is transformed from a solid (glass) to a viscoelastic liquid. On the other hand, at constant concentration of the small star, increasing its hydrodynamic radius yields a melting of the glass; eventually, for very large stars, there is an apparently tendency for a re-entrant vitrification of the mixture.

3.3 Structure of the System

We consider a binary mixture of N_1 large stars of functionality f_1 and N_2 smaller ones of functionality f_2 in a macroscopic volume V . The theoretical description of the binary star-polymer mixture is based on the knowledge of the three partial structure factors of the system, which describe the correlations between the centers of the stars. In order to calculate these data, we use the concept of effective interactions [16] between the star cores. In this coarse-grained method, the monomer degrees of freedom are traced out and the star polymers are modeled as soft colloids, an approach pertinent to the problem at hand, as indeed the monomers continue to fluctuate even in the glassy state and only the stars as whole objects arrest. Thus, the positions of the star centers and the correlations between them are the dynamical degrees of freedom of interest. They interact via an ultrasoft pair potential that depends on their relative separation.

The effective interaction between particles of species i and j reads as [57]:

$$\beta V_{ij} = \Theta_{ij} \begin{cases} -\ln\left(\frac{r}{\sigma_{ij}}\right) + \frac{1}{1 + \sigma_{ij}\kappa_{ij}} & \text{for } r \leq \sigma_{ij}; \\ \frac{1}{1 + \sigma_{ij}\kappa_{ij}} \left(\frac{\sigma_{ij}}{r}\right) \exp(\sigma_{ij}\kappa_{ij} - r\kappa_{ij}) & \text{else,} \end{cases} \quad (3.1)$$

where

$$\sigma_{ij} = \frac{\sigma_i + \sigma_j}{2}$$

,

$$\frac{2}{\kappa_{ij}} = \frac{\sigma_i}{\sqrt{f_i}} + \frac{\sigma_j}{\sqrt{f_j}}$$

, and

$$\Theta_{ij} = \frac{5}{36} \frac{1}{\sqrt{2}-1} \left[(f_i + f_j)^{3/2} - \left(f_i^{3/2} + f_j^{3/2} \right) \right].$$

Again, $\beta = (k_B T)^{-1}$ is the inverse temperature, with k_B being Boltzmann's constant and σ_i is the corona diameter of species i that turns out to coincide numerically with

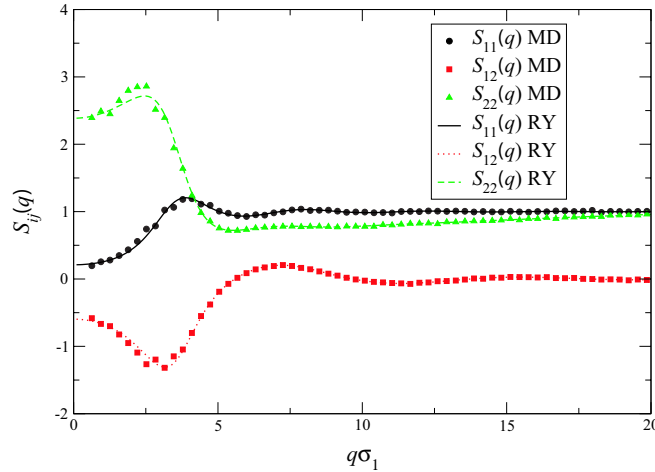


Figure 3.3: Partial structure factors of the binary mixture from molecular dynamics simulations (MD) and Rogers-Young theory (RY). Here the parameters are $f_1 = 270$, $f_2 = 32$, $\rho_1\sigma_1^3 = 0.1$, $\rho_2\sigma_1^3 = 10$, and $\xi = 0.1$.

the corresponding hydrodynamic radius $R_h^{(i)}$ [70]. Accordingly, we define the size ratio of the system ξ as

$$\xi \equiv \frac{\sigma_2}{\sigma_1} < 1. \quad (3.2)$$

The origin of this interaction is entropic, therefore the potential scales linearly with temperature.

Fig. 3.3 contains a comparison of structure factors of the system, as obtained from molecular dynamics (MD) simulations and from solving the OZ equation with the RY closure [66].¹ The interactions between the stars are given by Eq. (3.1). The RY approximation provides an excellent description of the structural properties of the mixture.

The dynamics of the stars can be studied employing one- or two-component mode coupling theory. For details of the two methods see Appendix B. The major difference between the two approaches is the treatment of the small component, which is in the two-component approach dealt with on equal footing as the large stars. Thakur and Bosse [91] show the size ratio dependence of the non-ergodicity parameter in binary hard sphere mixtures, where the ergodic to non-ergodic transition is consistent with our results (Fig. 3.4). The plot shows the development of the large and small star non-ergodicity parameters ($f_{11}(q)$ and $f_{22}(q)$, respectively) on increasing the size ratio. While $f_{11}(q)$ is virtually independent of ξ (except for

¹We simulated a system of 500 large and 5000 small stars to calculate the structure factor. We let the simulation run for 10^6 steps after equilibration.

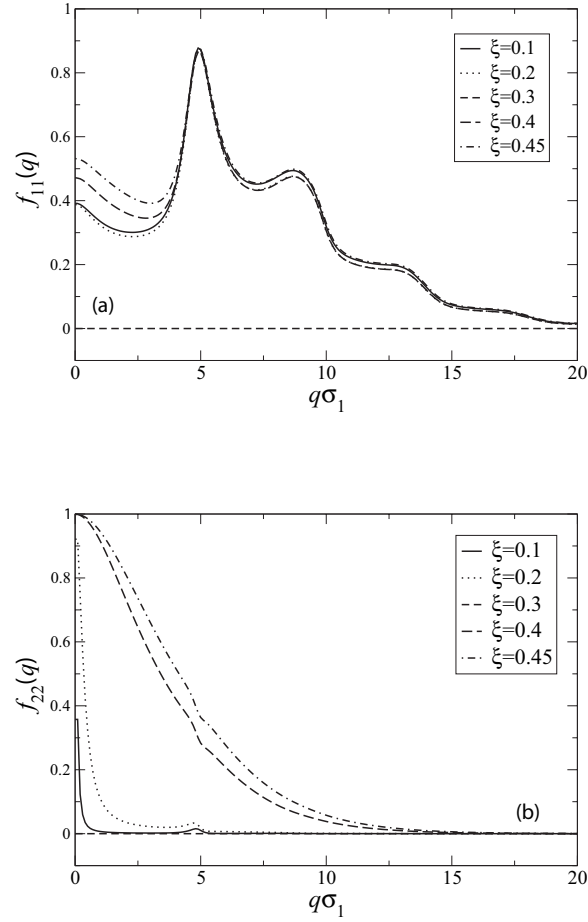


Figure 3.4: The nonergodicity factors $f_{11}(k)$ (a) and $f_{22}(k)$ (b) of the large and small components, for $f_2 = 32$, $\rho_2\sigma_1^3 = 0.02$ for different ξ -values. Note that for $\xi = 0.3$ the system is ergodic.

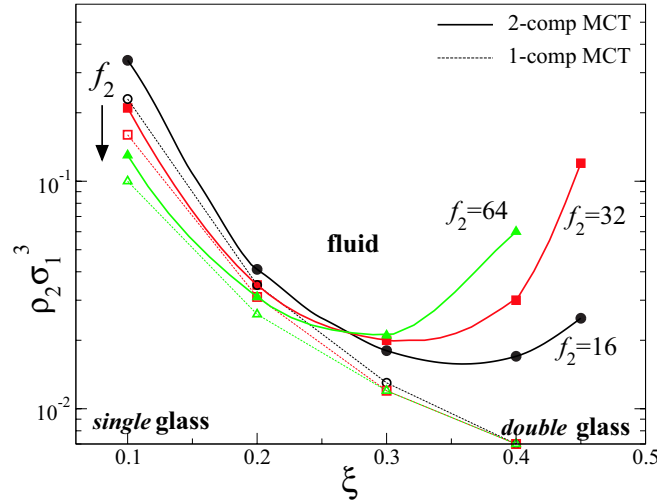


Figure 3.5: Kinetic phase diagram based on MCT calculations. The points trace the melting line separating the solid (below) from the fluid (above) behavior as predicted by one- and two- component MCT. The lines are guides to the eye. The large star functionality is $f_1 = 270$, the number density is kept constant at $\rho_1 \sigma_1^3 = 0.345$. Circles: $f_2 = 16$, squares: $f_2 = 32$, triangles: $f_2 = 64$.

$\xi = 0.3$ where the system is ergodic), $f_{22}(q)$ shows a dramatic change in the shape. For small ξ , $f_{22}(q)$ is nonzero only in a very small range of q . The length scale corresponding to this region is the size of the larger stars. This behavior can be interpreted in terms of a fluid small component [91, 92]. For large ξ , the system displays the behavior of a solid state.

3.4 Phase Diagram

We investigate how the dynamic properties of a solution of large star polymers can be influenced by small star additives. Fig. 3.5 summarizes the result of the MCT calculations. We start from a glassy sample ($f_1 = 270$, $\rho_1 \sigma_1^3 = 0.345$) and investigate the shape of the melting line as a function of the size ratio ξ for different functionalities of small stars in order to show how the dynamics of the system depend on size and functionality of the additives. We find a U-shaped line separating the ergodic from the non-ergodic regions in the parameter space. A similar U-shape was found in the experimental data presented in Fig. 3.2.

For small ξ , the melting of the glass can be interpreted in terms of a standard depletion mechanism where the small component remains mobile. This is corroborated by the fact that for small ξ one- and two-component MCT yield the same

trends and that the $f_{22}(q)$ in Fig. 3.4 show fluid-like behavior. The melting is driven by the fact that the depletion mechanism leads to a decrease of the repulsion between the large particles and thus to a softening of the cages. Within the effective, one-component approximation the depletion effect grows stronger with increasing ξ , as this leads to a concomitant increase of the depletion range and depth, i.e., to a more drastic effective weakening of the inter-star repulsions. However, the essential question is whether the aforementioned one-component approximation indeed holds as ξ increases.

For large ξ , the simple depletion scenario does not hold anymore. The smaller stars become now as large as the voids in the glassy matrix of the large ones and they can get trapped there, forming themselves a glass within the glass. The assumption of small star mobility breaks down. Therefore, the one-component MCT completely fails to describe the experimental results in Section 3.2. Since the small stars become trapped in the cages formed by the large ones, they start to contribute to cage formation themselves. When ξ grows, this trapping mechanism becomes more effective. This leads to a reversal of the slope of the vitrification line. Finally the caging mechanism gets dominant, so that for $\xi > 0.45$ no melting is found within MCT. Therefore, we distinguish between two states under the melting line: a single glass when the small component remains mobile and a double glass when both species become arrested. The same type of behavior is found in experiments of hard sphere mixtures with large size asymmetries [93]. However, in hard sphere mixtures a melting of the large sphere glass upon adding the second component was not observed. This distinction is further supported by a quantitative analysis of the trends in the elastic moduli, presented below.

3.5 Elastic Modulus

The properties of the glass depend on the non-ergodicity parameters of the system. A quantity that readily allows comparisons with experiments is the elastic modulus $G'(\omega)$. The zero-frequency limit² $\omega \rightarrow 0$ of the modulus is given by [94, 95]:

$$G' = \frac{k_B T}{60\pi^2} \int_0^\infty dq q^4 \text{Tr} \left[\left(\rho \frac{d\tilde{\mathbf{C}}(q)}{dq} \cdot \bar{\mathbf{P}}(q, t \rightarrow \infty) \right)^2 \right], \quad (3.3)$$

where $\tilde{\mathbf{C}}(q)$ is the 2×2 matrix of the direct correlation functions defined in Eq. (A.2) and Tr stands for the trace of the resulting matrix. The matrix $\bar{\mathbf{P}}(q, t)$ is the

²The term zero-frequency (or $t \rightarrow \infty$) refers here to the ideal MCT-result, according to which the glass (a non-equilibrium state) survives infinitely long.

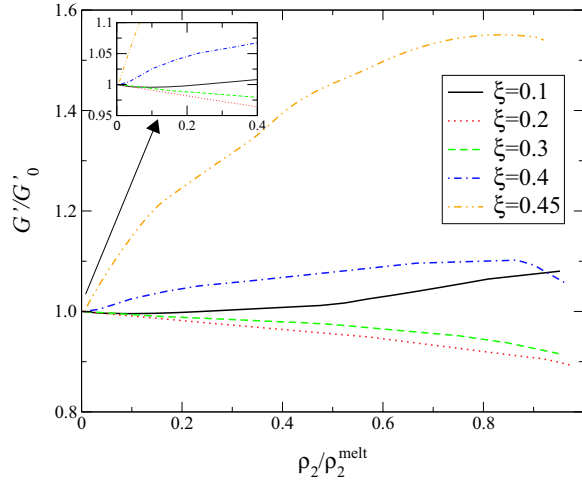


Figure 3.6: Plot of G'/G'_0 , where G'_0 is the elastic modulus of the pure one-component system, as a function of depletion density, for different size ratios ξ . The inset is the magnification of the small ξ region.

dynamical generalization of Eq. (B.8) from Appendix B:³

$$[\bar{\mathbf{P}}(q, t)]_{ij} = \sqrt{x_i x_j} S_{ij}(q, t) \quad (3.4)$$

and the long time limit of the dynamic structure factors is given by

$$S_{ij}(q, t \rightarrow \infty) = S_{ij}(q) f_{ij}(q). \quad (3.5)$$

Clearly, in the ergodic state, $f_{ij}(q) = 0$, the elastic modulus G' vanishes, whereas in non-ergodic states a finite result is obtained. The order of magnitude of the latter is set by $G' \sim k_B T / \sigma^3$, where σ is the particle size, resulting into typical numbers $G' \sim 10^2$ Pa at room temperature.

In Fig. 3.6 we show the theoretical results for G' , demonstrating that, for $\xi \leq 0.3$, the elastic modulus has a (local) maximum at $\rho_2 = 0$, whereas for the larger size ratio, $\xi = 0.4$, it has a minimum there: the double glass displays a higher mechanical resistance to shear than the single one, whereas in the latter the fluid-like second component does not contribute to G' . Its effect is to lower G' through the softening of the cages formed by the large component.⁴ These findings offer additional support to the single/double glass picture put forward above. Indeed, at the small ξ -regime,

³In this notation, $\bar{\mathbf{S}}(q) = \bar{\mathbf{P}}(q, t = 0)$, obtaining the equal-time static structure factors.

⁴For $\xi = 0.1$ the maximum of G' at $\rho_2 = 0$ is only local because as ρ_2 grows, a short-range attraction between the large stars develops, leading to a temporary stabilization of the cages formed by the latter. This attraction is absent for higher ξ -values, see, e.g., [96].

the small star polymers act as agents that tend to break the cages of the large stars, without taking part in glass formation themselves. Accordingly, they lower the total elastic modulus. But as ξ grows and the additives actively participate to cage formation themselves, they contribute in the elastic modulus in their own right, leading to an increase of its value up to a factor 1.6. Similar trends have also been seen in the experiments [70]. At fixed ρ_2 , the ξ -dependence G' is non-monotonic, showing decrease up to $\xi \approx 0.4$ and a growth thereafter [70].

3.6 Summary and Conclusions

We have presented experimental and theoretical results on the ways in which the rheology of soft colloidal systems can be influenced by the addition of chemically identical but physically distinct additives. Colloidal star polymers, which have been used in the present study, provide indeed a clean, versatile and controllable system to this purpose.

The phenomenon of glass melting is similar to the one encountered in colloid-polymer mixtures [10–13]. The physics and implications of this are, however, in our case very different. Whereas in colloid-polymer mixtures the solid melts due to the induction of short range attractions on the colloids, which eventually drive the formation of a reentrant attractive glass, in our case effective attractions are completely absent for the low density of depletants studied. This fundamental difference is witnessed by the fact that, in colloid-polymer mixtures, melting takes place only for very asymmetric size ratios, $\xi \leq 0.1$, whereas in the present case it persists to $\xi \simeq 1$. The melting of the solid in colloid-polymer mixtures requires the fluidity of the added polymer [72]. To the contrary, for star mixtures, the addition of a second component which becomes increasingly glassy is capable of bringing about melting of the double glass.

Moreover, the ability to melt the glass formed by the large component for large size ratios between the large stars and the smaller additives, can be traced back to the softness of the glass-forming component. Moreover, two distinct types of glasses have been identified, one in which the additives are ergodic at all concentrations and one in which they actively participate in cage formation, thus giving rise to a double glass. On the basis of the evidence at hand, we anticipate that there exists no sharp transition between the two types of glasses but rather a diffuse ‘crossover domain’, because due to the softness of the pair interactions the movement of the small stars is not completely blocked, but becomes gradually slower. To answer this question, to address the issue of aging, and to draw a more complete ‘kinetic phase diagram’ encompassing also the region of high additives concentration, more detailed theoretical and simulation work, as well as additional experimental measurements, including rheology and dynamic scattering, are required. In the next chapter, we

present a detailed study of the phase diagram based on theory and simulation in order to contribute to the solution of this problem.

Chapter 4

Binary Star Polymers: Relaxation Dynamics

As we have shown in the previous chapter, the addition of small stars to a glass of large ones leads to a recovery of ergodic behavior in the system, confirmed by theory and experiment. However, we only studied properties of the mixture for $t \rightarrow \infty$. Here, we examine the full time dependence of the correlation functions by molecular dynamics simulations. Moreover, at large concentration of additives an arrested state is expected again. We compare simulation data to theoretical predictions based on mode coupling theory. We find multiple distinct glassy states in the system.

4.1 Asymptotic Solutions of the MCT Equations

The mode coupling equations we use to theoretically describe the dynamics are described in Appendix B. In general, multiple glassy solutions of Eq. (B.9) can exist within mode coupling theory, due to higher order bifurcation singularities. This case has been extensively studied for effective one-component systems for attractive colloids, where higher order MCT singularities have been predicted theoretically [9] and verified by numerical simulations [97, 98] and experiments [10, 11, 90]. For multicomponent systems, a detailed MCT study has not been performed yet. However, suggestions of higher order singularities and glass-glass transitions, in particular of one of the involved species, have started to emerge from simulations of asymmetric polymer blends and soft sphere mixtures [99–101]. In the case of distinct glassy states, the non-ergodic properties will be different, thus the $f_{ij}(q, t)$ will also be different. Also, close to such singularities, competition between the different glassy states modifies the standard MCT dynamical behavior close to the liquid-glass transition (labeled usually of type B or A_2). For such an A_2 transition, a two-step relaxation

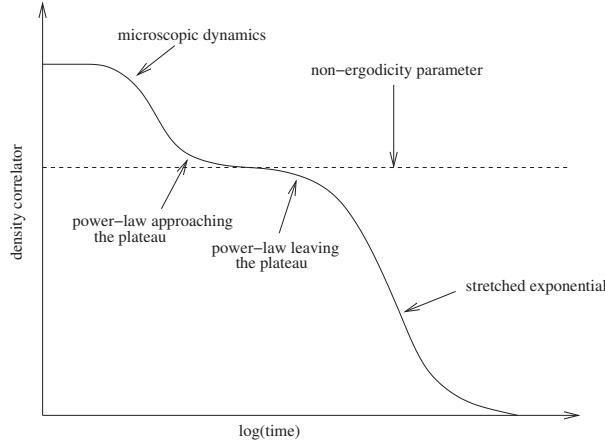


Figure 4.1: Sketch of a density correlator in a fluid close to the glass transition. Following the initial microscopic decay, there is a time window where universal features of MCT are observed. The leading order terms in time at the approach and departure of the plateau are power laws (see Eqs. (4.2) and (4.3)). The final decay of the correlator can be modeled as a stretched exponential (Eq. (4.4)).

is well described by MCT, through an asymptotic study of the correlators near the ideal glass solutions.

The density correlators are defined as

$$\phi_{ij}(q, t) = \langle \rho_i^*(q, 0) \rho_j(q, t) \rangle / \langle \rho_i^*(q, 0) \rho_j(q, 0) \rangle, \quad (4.1)$$

where

$$\rho_j(q, t) = \sum_{l=1}^{N_j} \exp \left[i \mathbf{q} \cdot \mathbf{r}_l^{(j)}(t) \right],$$

with $\mathbf{r}_l^{(j)}$ the coordinates of the l -th particle of species j ($j = 1, 2$) and the asterisk denotes the complex conjugate. A sketch of the behavior of a typical density correlator close to the glass transition is shown in Fig. 4.1. From the density correlator ϕ in the liquid the critical non-ergodicity parameters $f^c(q)$ can be extracted. The approach to the plateau is described by a power law, regulated by the exponent a , i.e.

$$\phi(q, t) - f^c(q) \sim h^{(1)}(q)(t/t_0)^{-a} + h^{(2)}(q)(t/t_0)^{-2a} \quad (4.2)$$

with t_0 the microscopic time, while the departure from the plateau, i.e. the start of the α -process, is expressed in terms of another power law, called the von Schweidler law, regulated by the exponent b ,

$$\phi(q, t) - f^c(q) \sim -h^{(1)}(q)(t/\tau_0)^b + h^{(2)}(q)(t/\tau_0)^{2b} \quad (4.3)$$

with τ_0 being the characteristic time of the relaxation. The exponents a and b are related to each other and to the exponent parameter λ [3] via a transcendental relation, and are independent of the particular q -vector considered. $h_{ij}^{(1)}(q)$ and $h_{ij}^{(2)}(q)$ are referred respectively as critical amplitude and correction amplitude [3]. On the other hand, the α -relaxation process is usually also well described by a stretched exponential, i.e.

$$\phi_{ij}(q, t) = A_{ij}(q) \exp[-(t/\tau_q)^{\beta_q}] \quad (4.4)$$

where the amplitude $A_{ij}(q)$ determines the plateau value, and the stretching exponent $\beta_q \leq 1$. For large q values, it has been shown that $\beta_q \rightarrow b$.

On the other hand, close to higher order singularities, the dynamical behavior is predicted to obey a logarithmic behavior. In particular, it holds,

$$\phi(q, t) \sim f^c(q) - h(q) [B^{(1)} \ln(t/\tau) + B_q^{(2)} \ln^2(t/\tau)]. \quad (4.5)$$

Here τ stands for a time-scale which diverges if the state approaches the mathematical singularity. The formula is obtained by asymptotic solution of the MCT equations [102]. The first term $f^c(q)$ is the sum of the non-ergodicity parameter at the singularity plus a correction which depends on the distance from the singularity.

In the following, when we find that correlators are not described by power-laws or stretched exponentials, we will adopt the expression in Eq. (4.5) to extract the non-ergodicity parameters from the simulations to compare the different glassy states.

4.2 MCT Results

Following the experimental setup discussed in Chapter 3, we investigate the effect of the addition of a second component of varying size and concentration on the glass formed by the one-component large stars with $f_1 = 263$. Here, we do not consider the issue of varying functionality of the small stars, partially discussed in [70], thus we fix $f_2 = 64$. Further studies with different f_2 will be presented elsewhere. Therefore, we consider a glass of large stars only, with density $\rho_1 \sigma_1^3 = 0.345$, corresponding to a glassy state within MCT [27]. At this fixed large star density, we add small stars and study within MCT (and later by simulations) the stability of the large star glass.

MCT long-time limit equations are solved iteratively discretizing the wave vector integrals on a grid of 1000 points for the binary equations (Eq. B.7) and 1600 for the one-component ones (Eq. B.5), with a mesh in wave vectors respectively of $0.1/\sigma_1$ and $0.0625/\sigma_1$.

From the MCT analysis, we determine a glass transition diagram in the (ξ, ρ_2) plane, that is reported in Figure 4.2. Results obtained, both in the full binary treatment of the mixture and in the effective one-component representation, are shown.

In the diagram, we only show the closest two points bracketing the liquid-glass transitions. Lines are a guide to the eye. With respect to the (ρ, T) phase diagrams that are usually shown in colloid-polymer (CP) mixtures [10, 18], we focus here on a single isochore and consider the addition of small stars with different concentrations, analogous to the T -axis, modulating the strength of the (attractive) depletion in CP mixtures, as well as of different size, which sets the effective attractive range in CP mixtures.

Examining Fig. 4.2, a liquid island appears to be surrounded by a sea of glasses. With respect to the reentrance in small additives concentration that is observed in CP mixtures upon increasing additive concentration, we detect two of these, respectively at small and large size of the additives, as well as a reentrance (or two) in size ratio. For convenience, we can roughly divide the phase diagram of star-star mixtures in four different regions to be discussed in the following:

1. small size and small concentration of the additives (region I);
2. large size and small concentration of the additives (region II);
3. large size and large concentration of the additives (region III);
4. small size and large concentration of the additives (region IV).

Let us start by examining region I. The addition of small stars with size ratio up to $\xi \approx 0.2$ causes the large glass star to melt due to a mechanism that is similar to depletion, although the effective interactions involved here are still repulsive, but the repulsion is softened with respect to the one-component case [96]. Indeed, within this region, a regime where effective attractive interactions between large stars become present is not expected [96], but will occur at larger ρ_2 (region IV). The small stars produce however a softening of the repulsion, thus a melting mechanism for the large star glass. In this respect the small stars are always liquid in this regime, even in those states in which the large ones are arrested, therefore we name for simplicity this glass a single glass [70].

On the other hand, moving into region II by increasing the small star diameter, the addition of a second component of not-so-small stars, with $0.2 \lesssim \xi \lesssim 0.45$, is still capable to produce a melting of the glass but through an entirely different mechanism, found in MCT and also confirmed by experiments (see Chap. 3). Indeed, the glass becomes stiffer through the addition of a second glassy component, as signaled by the study of the elastic modulus in theory and experiments reported in [70, 80], up to a certain density where it becomes more convenient entropically to free available volume for both stars simultaneously, paying a (finite) penalty price by decreasing the nearest neighbor distance, hence causing again liquidification upon further ρ_2 increase. Therefore, this melting mechanism is entirely due to the softness of interactions involved, and it does not have an equivalent in terms of mixtures

involving hard-spheres. This second glassy state we identify as a double glass, since both species are now glassy. Thus, it undergoes a double melting mechanism, when both glassy components are liquefied. We note, however, that the presence of two different glasses for asymmetric mixtures, from a single to a double glass, upon increasing the density was already found for hard spheres [91–93], but the new feature of the presently investigated soft mixtures is that both glasses can be simultaneously melted by increasing the amount of the small additives in the mixture.

Clearly, a theoretical framework capable to correctly describe the single glass case should be based on the slowing down of just the large stars, thus one-component MCT, where the smaller stars are assumed to form a fluid medium that does not participate in the glass formation, is the conceptually right framework to use. On the other hand, the double glass corresponds to both species being comparably slow, thus compelling the use of binary MCT. The problem to switch continuously from one to two-component description cannot be incorporated within MCT, because it is based on the assumption of a single slow timescale in the system, and thus it cannot take into account a difference in particle mobilities. However, it turns out that in the case of star polymers mixtures, differently from that of colloid-polymer mixtures [72], at low ξ , i.e. in the single glass regime, both treatments give qualitatively the same behavior, as illustrated also in Figure 4.2, while at large ξ , in the double glass regime, the discrepancy becomes large, signaling the tendency of the small component to also arrest, and only binary MCT can be used, giving rise to the U-shape also observed in the experiments for low ρ_2 . Otherwise the one-component curves provide a monotonic behavior as a function of ξ (see Fig. 4.2). The deviation between the two approaches at large ξ can also be understood in terms of the scaling of the relative short-time mobilities of the two species with size ratio [72]: as $\xi \rightarrow 1$ the time-scale separation between the degrees of freedom of the small and large stars disappears. We just rely on two-component MCT in the following, unless explicitly mentioned.

In the present work we complete the picture of previous results shown in Chapter 3 with the investigation of Regions III and IV. Moreover, we study the full dynamics of the density correlators in the different glasses. In region III, for large concentration of not-so-small additives $\xi \sim 0.4$, we find a reentrance in the glassy regime with respect to ρ_2 , with the appearance of a new glassy state (second double glass) for large ξ and large ρ_2 . Such a new glass originates from a change of the localization length of the original double glass, which is entirely due to the softness of the repulsions. When small stars are added to the double glass, at first there is a liquid where where the interstar distance decreases opening up space for diffusion. But a further increase causes a second jamming at a new length scale that will depend on the particular parameters of the mixture. Interestingly, due to the ultrasoft nature of star polymers, one could in principle speculate that a cascade of reentrant glassy phases of decreasing localization length could be generated upon systematic increase

of ρ_2 , in analogy to what happens in the equilibrium phase diagram of star polymer one-component solutions [19], where a cascade of different crystal structures is found. Moreover, the theory predicts the window of melting of the double glass just up to $\xi \sim 0.45$, but experimental results have already confirmed [70] that this can happen up to much larger ξ , and it might be a limitation of MCT which always tends to overestimate the tendency of glassification.

Finally in region IV, at low ξ , the depletion mechanism can finally induce effective attractions between the large stars [96], causing a liquid-gas phase separation, in complete analogy with colloid-polymer mixtures. Of course, such phase separation is accompanied by an increase in $S(0)$, that could cause a problem in MCT, and predicting a glassy state close to phase separation, exactly like as in CP mixtures [95, 103]. However, with the use of RY structure factors, we can only find a glass within binary MCT for $\xi = 0.1$, while the one-component treatment always provides a liquid state up to the maximum investigated ρ_2 approaching phase separation. We could not push the analysis to larger ρ_2 and $\xi = 0.2, 0.3$, and for larger ρ_2 for $\xi = 0.1$ due to a breakdown in the convergence of the Rogers-Young, as well as the simplest HNC closure in this region. It is interesting to ask the question whether, for low ξ where the emergence of attractive interactions is detected, an attractive glass can be found in star polymer systems, i.e., also in systems with soft interactions. To elucidate this issue, we refer to the simulation results reported below.

The interesting question whether MCT predicts any sharp glass-glass transitions between single and double glass, or between double to second double glass, or towards attractive glass will be the subject of a future study. However, the anomalous dynamics, to be discussed within the analysis of the simulation results, suggests the possibility of the existence of a higher order MCT singularity connected to such glass-glass transitions. It is just to be noted the richness of the glassy phase diagrams of star polymer mixtures, where in principle four distinct glassy states and four kind of glass-glass transition (either sharp or smooth) are found within the present study.

To summarize, MCT predicts, for the chosen $\rho_1\sigma_1^3 = 0.345$ an almost O -shaped liquid region, that is surrounded by four different glassy states and phase separation and/or attractive glass. We can complement the study of phase diagram by looking at the non-ergodic properties of the four glasses. To do so, we report in Figure 4.3, the calculated MCT partial non-ergodicity parameters, both for collective (bottom) and self (top) relaxation dynamics. The results reported here correspond to those for the first glassy points observed theoretically coming from the liquid while increasing ρ_2 , hence they are ‘critical’ non-ergodicity parameters. The small stars $f_2^s(q)$ allows us to distinguish immediately a single from a double glass, since it is identically zero for the single glass, as already found in binary asymmetric hard sphere mixtures [92]. Thus, although, in binary MCT the broken ergodicity transition is postulated to happen simultaneously for both species, the self non-ergodicity parameter allows to

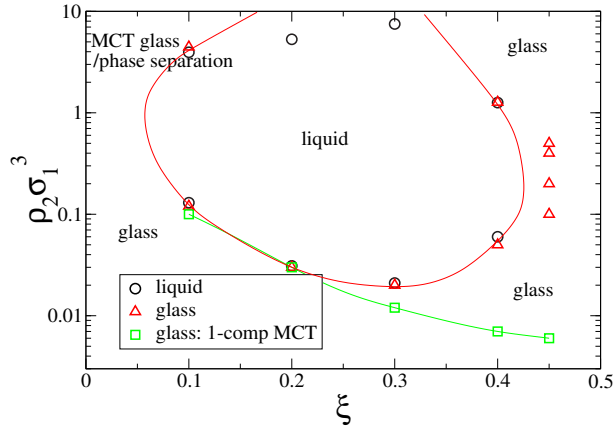


Figure 4.2: Kinetic phase diagram of the system as predicted by ideal MCT. The points are the state points closest to the transition. For a comparison, see Fig. 3.5. The lines are guides to the eye.

distinguish between mobile and immobile species. Also, the partial $f_i^s(q)$ for both types of stars are larger both in range and in amplitude in the second double glass than in the standard one. Fitting $f_i^s(q)$ to a Gaussian curve $\exp(-q^2/6l_0^2)$ provides an estimate for the localization length l_0 within the glass. Fits are also reported in the figure. The Gaussian fit works very well for large stars, but deviations to it are observed for small stars, in both double glasses. The extracted localization length is $l_0 \approx 0.26\sigma_1$ for large stars both in single and double glass, while it is $l_0 \approx 0.14\sigma_1$ for the second double glass, thereby a factor of 2 reduction in the cage length is predicted by the theory. A larger variation in l_0 is predicted for the small stars from $0.51\sigma_1$ for the double glass at low ρ_2 to $0.11\sigma_1$ for the double glass at high ρ_2 . For the collective $f_{ii}(q)$, the results are very similar to those of the self, only much stronger oscillations, in phase with static structure factor peaks, are observed. For the small stars, these are much more pronounced in the second double glass regime than in the standard double glass case, where they weakly appear only at the first peak of $S_{11}(q)$. We notice that upon changes in ρ_2 within the glassy phases, we detect no change in f_q for the double glass while a significant increase is observed for large ρ_2 , accompanied also by an increase in the range, for both star species. This finding is similar to that for attractive glasses in colloid-polymer mixtures, where further increase of the additives leads to an increase in nonergodicity parameter both in amplitude and range. Therefore, in the second double glass regime, although effective interactions remain repulsive, the small stars produce a strong localizing mechanism, that has some similarities with an effective attraction. However, looking at the partial $S_{ij}(q)$ we do not see an increase in the compressibilities or a non-monotonic dependence in the growth of peaks. Simply, the structure factor peaks for large stars continue

to decrease upon addition of small stars, while these display themselves more and more enhanced peaks.

4.3 Simulations: Iso-diffusivity Lines

We performed standard Newtonian dynamics simulations for stars interacting via the effective potential in Eq. (3.1). Although the use of Brownian dynamics simulations would be more realistic for star-star mixtures to mimic the solvent effect, this is by far less efficient and it would not allow us to probe the slow dynamics regime. Moreover, several confirmations of independence of long-time properties from microscopic dynamics have been provided so far [27, 104]. We investigate several mixtures, in order to have a complete picture of the phase diagram and of the dynamical slowing down. Due to the various conditions to be investigated, the number of particles varies throughout the diagram. In general, we fix $N_1 = 1000$ and vary N_2 consequently. However, under particular extreme conditions, like that of the attractive glass study (see below), we use $N_1 = 250$, due to the large ρ_2 investigated. Also, for low values of ρ_2 e.g. in single and double glass regimes, we fix the minimum number of small particles to $N_2 = 500$ and vary N_1 accordingly.

The first issue to take into account is how to fix the short-time mobilities of the small particles with respect to the large ones. As already noticed in earlier simulations of explicit colloid-polymer mixtures, the simple addition of small particles of same mass for MD (and corresponding of same diffusivity for Brownian dynamics), simply increasing the total number density in a state that is already glassy, has the result of just slowing down further the dynamics, even in the case of star polymers. This would imply no melting at any given ρ_2 and ξ in full contrast with MCT predictions and experimental results. Thus, following the ideas in [70], in this paper we adopted the mobility ratio corresponding to the square root of the mass ratio, using the scaling for the mass m of star polymers, namely $m \sim f^{2/3}\sigma^{5/3}$ [14, 16]. In this case, we indeed observe a speeding up of the dynamics upon addition of the second component. Units of length, mass and energy are σ_1 , m_1 and $k_B T$, respectively. Time is measured in $\tau_{\text{MD}} = \sqrt{m_1 \sigma_1^2 / (k_B T)}$ and the integration time step is varied according to the mass ratio, as $\Delta\tau = 5 \cdot 10^{-3} \sqrt{m_2 / m_1} \tau_{\text{MD}}$. Our simulations are done for $f_1 = 263$ and $f_2 = 64$ as the MCT study presented above.

We fixed the density of the large stars to $\rho_1 \sigma_1^3 = 0.345$, as in the MCT calculations. Indeed, this was the last point accessible in simulations, for a one-component system of 263-armed star polymers before crystallization takes place. For this state point, the diffusion coefficient, that will be our reference for the mixture cases, is $D_0 = 0.0119 \sigma_1^2 / \tau_{\text{MD}}$. This value is rather high, and, indeed, the mean squared displacement of the single-component case for $\rho_1 \sigma_1^3 = 0.345$ does not show the presence of a plateau, i.e., no signature of a clear slowing down of the dynamics. Nonetheless,

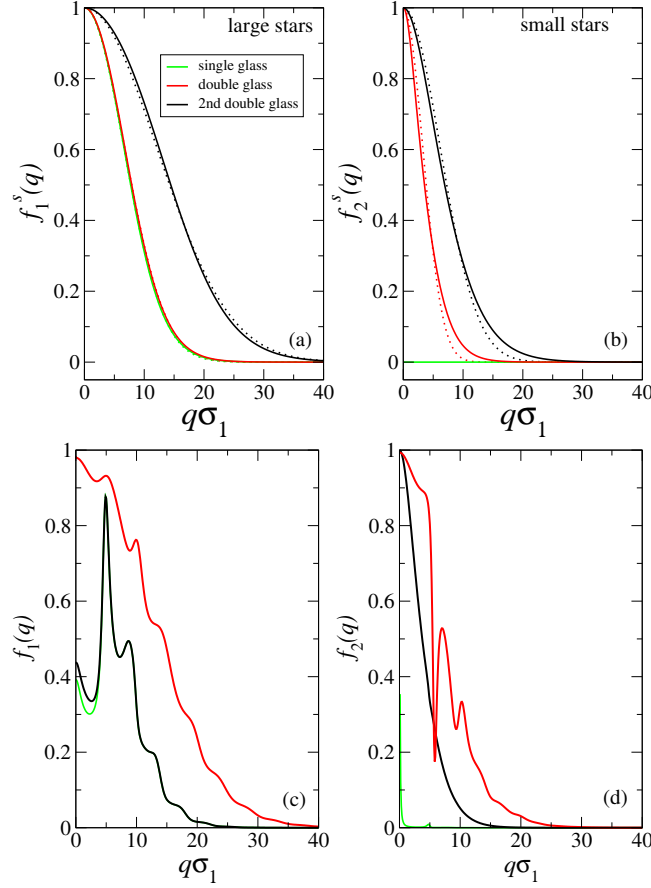


Figure 4.3: Partial non-ergodicity parameters from MCT. The top figure shows the self dynamics for the three different glasses and Gaussian fits to extract the localization length. In the bottom part we show the collective dynamics. For all curves it is $\rho_1\sigma_1^3 = 0.345$. For the single glass it holds $\rho_2\sigma_2^3 = 0.12$ and $\xi = 0.1$, while in the double glass it is $\xi = 0.4$. The second double glass corresponds to $\rho_2 = 1.27$ and $\xi = 0.4$. The Gaussian fits are the dotted lines. The self non-ergodicity parameter of the large stars in the single and double glass is virtually identical, therefore the lines fall on top of each other, however the self dynamics for the small ones is very different in both cases. Also the Gaussian fits fall on top of the MCT data for the self non-ergodicity parameter of the large ones. Therefore they are indistinguishable in the figure. The collective dynamics of the large stars in the single and double glass only shows deviations for small q .

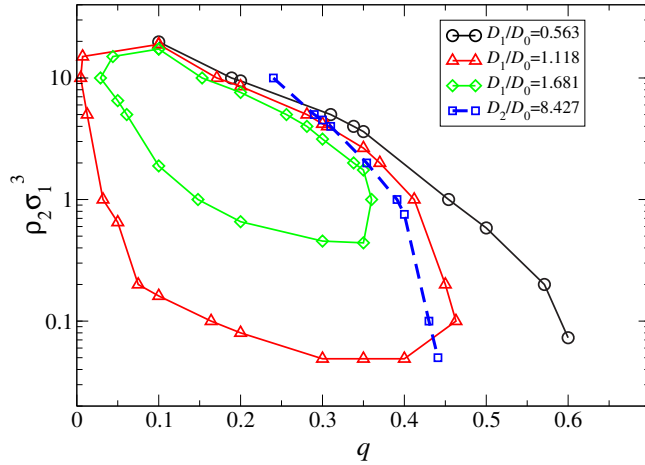


Figure 4.4: Iso-diffusivity lines from MD simulations in the (ρ_2, ξ) -representation. The density of large stars is kept constant at $\rho_1 \sigma_1^3 = 0.345$. The line for the smallest value of the diffusivity is not closed because the chosen value of D is smaller than the diffusivity of the reference one-component system (D_0).

this choice of ρ_1 allows us to calculate quite complete iso-diffusivity lines, in a reasonable computer time. Such lines are precursors of the glass transition lines, and they always display a similarity in shape as the MCT line, as demonstrated already for one-component star polymers [27], for other repulsive potentials [105], as well as for short-range attractive square well [13].

To study iso-diffusivity lines we calculate the mean-squared displacement (MSD) $\langle r^2(t) \rangle$ of large and small stars separately. From the long-time behavior, we extract the respective self-diffusion coefficient defined as, following Einstein relation,

$$D = \lim_{t \rightarrow \infty} \langle r^2(t) \rangle / (6t). \quad (4.6)$$

In Fig. 4.4, we report the iso-diffusivity lines for three different values of D/D_0 in the (ξ, ρ_2) plane. The fact that we examine only a decade in decrease of D/D_0 is due to the many constraints to study the whole phase diagram in very different conditions between the different four regions of small/large ξ and small/large ρ_2 and to the one-component tendency to crystallize for $\rho_1 \sigma_1^3 > 0.345$ (see below). Also, the line corresponding to the slowest states is drawn only on the large ξ side, since $D < D_0$ and hence slower than the one-component case ($\rho_2 = 0$ -axis and $\xi = 0$ -axis). The upper left corner is missing, again, due to the intervening phase separation. Notwithstanding all these details, it is evident the shape of an asymmetric “O” that resembles the shape of the MCT phase diagram. Moreover, we know that the shape of the iso-diffusivity lines is robust with respect to the decrease of D/D_0 , thus we can assume these results to be general enough for the description

of star-star mixtures. The agreement with experiments that was found for the low ρ_2 U-shape is confirmed also by simulations incorporating the mobility issue in the right way, while further experiments at large ρ_2 are needed to confirm the O -shape predictions of both MCT and simulations.

Interestingly, from the simulations we can also trace out correctly the iso-diffusivity lines of the small stars. Within binary MCT there should be no distinction between the glass lines of the large and small stars respectively, however this is based on the wrong approximation that small stars are as slow as the large stars. Removing this constraint in the simulations, we also report in Figure 4.4 an iso-diffusivity line of the small stars. It has a similar shape as the large ξ /large ρ_2 region while the dynamics of the small stars is much faster for low ξ .

We can now exploit the simulation results to directly probe the four regions of slowing down and compare the different glasses, in order to clarify the characteristics of the multiple glassy states appearing in these types of mixtures, in comparison with the MCT results. However, to do so, we need to overcome the crystallization problem for small ρ_2 , which does not allow to see a real slowing down of the dynamics for the one-component system, and consequently also the single and double glass. Hence, we considered the addition of polydispersity in the large stars diameter only, chosen to follow a Gaussian distribution with a width of 10% [106]. We also checked that, compared to the one-component case, the dynamics is not substantially affected. In this way, we could reach low values of diffusivity by increasing ρ_1 , as illustrated in Figure 4.5 compiling together results for the monodisperse and polydisperse one-component reference system. Hence, we selected the value $\rho_1\sigma_1^3 = 0.41$ to investigate the dynamics of single and double glass respectively. To improve statistics, we average over 5 independent runs for each studied state point. Each independent run for the three studied state points required about 3 months CPU time. On the other hand, for the other two glasses at large ρ_2 , we still consider our initial value $\rho_1\sigma_1^3 = 0.345$, since it is now the crucial presence of large additives affecting the dynamics, and therefore we do not need to go to higher ρ_1 . In this respect, it is perhaps useful to think of the phase diagram of Figs. 4.2 and 4.4 in terms of different ρ_1 values. At lower ρ_1 , the single and double glass phase will disappear, while the attractive glass will be still competing with phase separation, as in CP mixtures. The only glass which should still be stable is the second double glass. At this point it would be interesting to ask the question of which minimum f_1 and f_2 are necessary for this to happen, as we know that one-component star polymer systems with less than $\approx 40 - 45$ arms do not ever glassify.

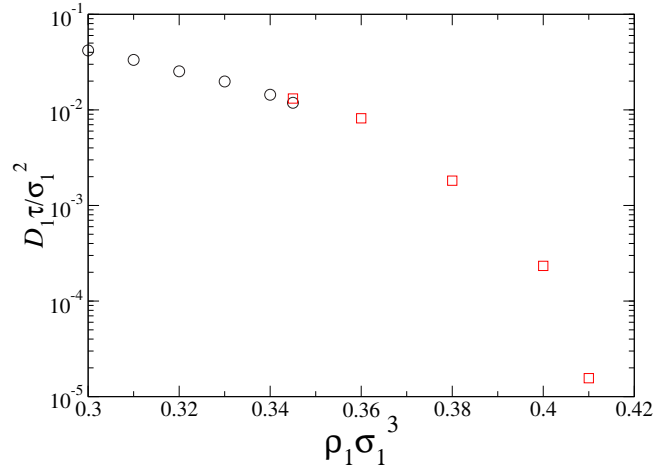


Figure 4.5: Diffusivity of the one-component system as a function of star density. The circles correspond to the monodisperse case. The squares correspond to simulations with added polydispersity to prevent the system from forming a crystal.

4.4 Multiple Glassy States

4.4.1 Region I: Single Glass

The state point reported here corresponds to $\rho_1 = 0.41$, $\rho_2 = 0.1$ and $\xi = 0.1$. Since $f_2 = 64$, we have a mass ratio $m_2/m_1 = 8.4 \times 10^{-3}$, and we are in the effective one-component regime.

Indeed, the mean squared displacement shows a clear separation in time-scales between the two species. After the initial ballistic regime, the small stars simply become diffusive, while the large ones display a long plateau, lasting about 3 decades in time, before eventually reaching the diffusive regime, so that there is a clear separation of time-scales. Correspondingly, a difference in the diffusion coefficient (and relaxation time) of about 3 orders of magnitude is observed. Thus, we can argue convincingly that the large stars are nearly arrested in a jammed state, with a localization length that can be extracted from the plateau height $l_0 \sim 0.25\sigma_1$ (horizontal line in Figure). By convention, we define the localization length as $l_0 = \sqrt{\langle r^2(t^*) \rangle}$, where t^* is the point of inflection of the MSD. A similar value could be extracted from a simulation of star polymers in theta-solvent [106], as well as from the MCT results above, suggesting rather robustly that the localization length of a soft star glass is slightly higher than of the typical hard sphere one due to the softness of the cages which allows more flexibility in the rattling than the rigid hard sphere ones.

We now turn to examine the density correlators. In Fig. 4.7, we show the behavior of $\phi_{ii}(q, t)$ for large (top panel) and small stars (bottom panel), respectively, for

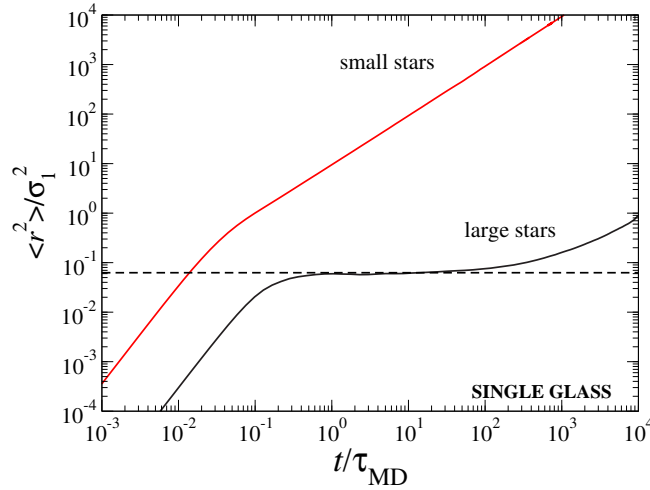


Figure 4.6: Mean squared displacement for the large and small stars in the single glass. The densities are $\rho_1\sigma_1^3 = 0.41$ and $\rho_2\sigma_1^3 = 0.1$; the size ratio is $\xi = 0.1$. The line indicates the estimate of the localization length for the large stars at the inflection point of MSD.

several wave vectors. As for the MSD, the large stars display a marked plateau, at all wave vectors, lasting for about three decades in time, and showing an oscillatory behavior in the height of the plateau with wave-vectors, as commonly found in standard glasses. We extract the non-ergodicity parameter of the system by fitting with a stretched exponential law the $\phi_{11}(q, t)$ for the large stars. We find that $f_{11}(q)$ oscillates in phase with the static structure factor, but in contrast to the MCT predictions (that are quite independent in the single glass region of the specific considered state point as discussed previously), it shows a marked increase at low q , while beyond the first peak the agreement is very good. We find that the stretching exponent β_q as a function of $q\sigma_1$ also oscillates in phase with $f_{11}(q)$, and tends for large q approximately to 0.6. Indeed, using this as b exponent for the von Schweidler law (Eq. (4.3)), we find that all curves are well-fitted with this type of law, in the region of departure from the plateau, and the estimate for $f_{11}(q)$ is in perfect agreement with that obtained from the stretched exponential fits. This also corresponds to an exponent parameter $\lambda \approx 0.7$, which is consistent with that calculated within MCT.

A similar analysis can be done on the small stars correlators. However, here the plateaus are so small that no accurate analysis can be performed. Nonetheless at small wave vectors, the stretched exponential fits work quite well. We find a tiny signal for the $f_{22}(q)$ just close to the first peak of the $S_{11}(q)$ for the large stars, suggesting a small loss of ergodicity of the small stars in the frozen cages of the large stars. This is in good agreement with the MCT predictions, but we do not detect

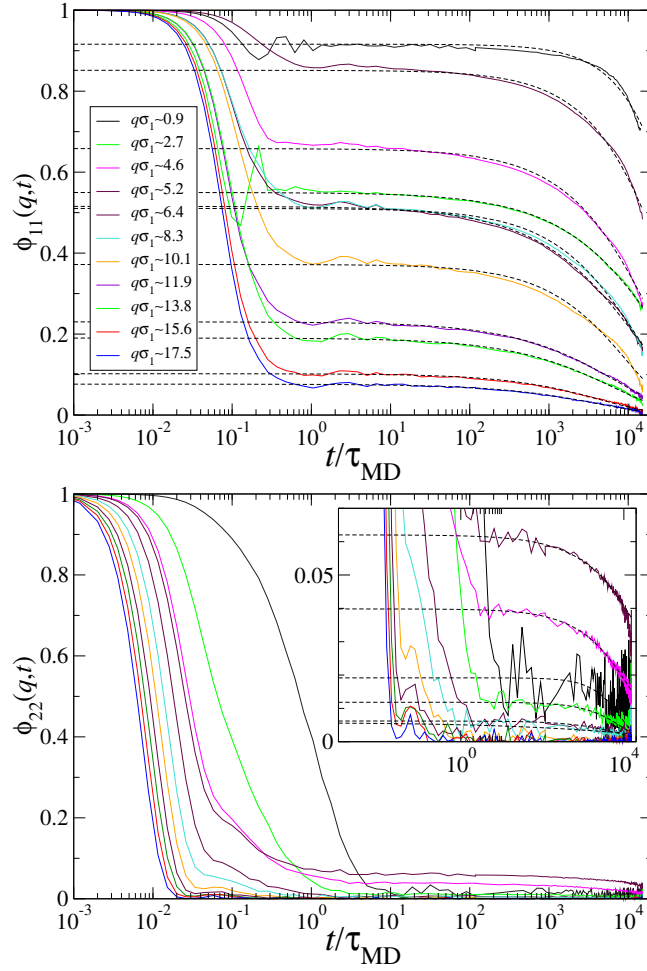


Figure 4.7: Density correlators for the large (top) and small (bottom) stars in the single class for different values of q . The parameters are the same as in Fig. 4.6. The dashed lines are stretched exponential fits to the curves. The inset in the lower figure show a magnification with the fits close to the peak in $f_{22}(q)$.

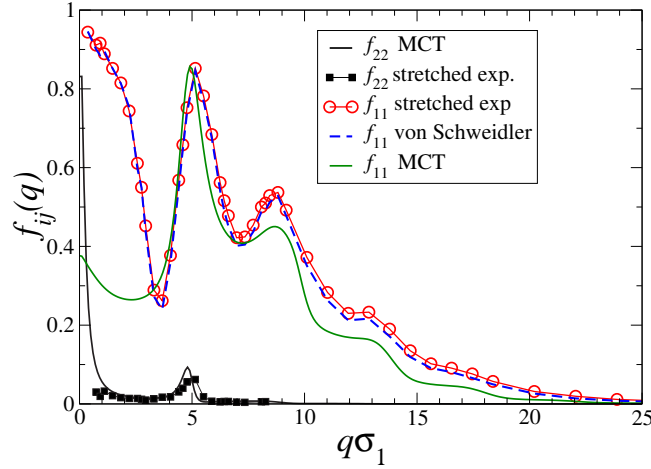


Figure 4.8: Comparison of partial non-ergodicity parameters from MCT and simulation in the single glass. The values from the simulations are obtained by stretched exponential fits for both types of stars. Also shown are von Schweidler fit results for large stars with $b = 0.6$. The simulation parameters are the same as in Fig. 4.6. The MCT results refer to critical parameters for $\rho_1\sigma_1^3 = 0.345$, $\rho_2 = 0.12$ and $\xi = 0.1$.

any increase of non-ergodicity at large length-scales. While MCT underestimates the non-ergodicity parameter of the large stars at low q , it overestimates the same for the small stars compared to the simulation results. Nonetheless, it is interesting to note that the small stars, although being very mobile, do display appreciable plateaus at the $S_{11}(q)$ peak, whose time duration is the same as those of the large star plateaus (see curve for $q\sigma = 5.2$ in Figure 4.7 b). Thus a coupling in time between large and small stars exists only at the peak of $S_{11}(q)$, which might explain why two-component MCT is still capable of correctly describing the general behavior of the mixture in this regime.

We can conclude from the combined study of MCT and simulations of the single glass that it really corresponds to a glass formed by the large stars only, whose properties are those typical of star polymer ultra-soft glasses. The small stars presence induces a weakening of the stability of such glass, until eventually melting it, and we observe this in the behavior of the large stars diffusion coefficient which increases with increasing density of the additives. Finally the small stars are truly ergodic and very mobile, they are never trapped in a metastable glass state, but do show a reduced loss of ergodicity for length-scales of the order of the static structure factor first peak for the large stars. We remark that this behavior is seen both in binary MCT and simulations, while it could not have been detected by an effective one-component treatment of large stars only.

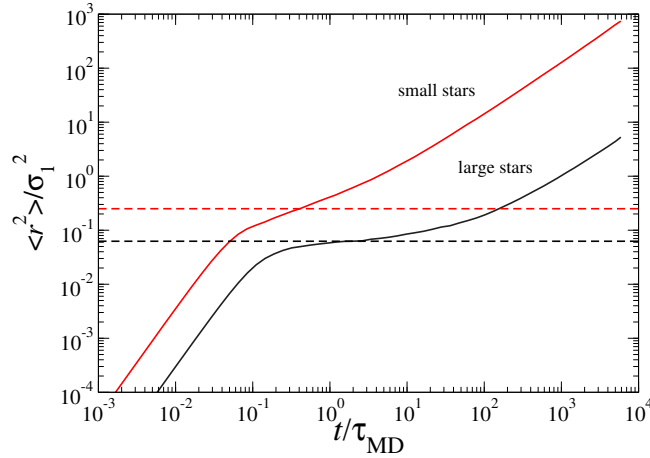


Figure 4.9: Mean squared displacement for the large and small stars in the double glass. The densities are $\rho_1\sigma_1^3 = 0.41$ and $\rho_2\sigma_1^3 = 0.1$; the size ratio is $\xi = 0.4$.

4.4.2 Region II: Double Glass

We now turn to examine the arrested state in the low ρ_2 at large ξ . We consider the case $\rho_1\sigma_1^3 = 0.41$, $\xi = 0.4$ and $\rho_2\sigma_1^3 = 0.1$, so that the composition of the mixture is the same as for the single glass examined above. However, the additives are larger and, consequently, also their mass is larger. Here the mass ratio is $m_2/m_1 = 8.5 \cdot 10^{-2}$, which is one order of magnitude larger than in the single glass. Therefore we treat both components in this case on equal footing in the theoretic approach, i.e., we use binary MCT. Indeed, the simulations confirm an arrest of both species.

In Fig. 4.9, we show the MSD for both components in the mixture. Differently from the single case, we observe a significant slowing down also in the small component behavior, suggested by the intermediate time regime where the slope of $\langle r^2 \rangle$ versus time is smaller than 1, indicating a subdiffusive regime in the dynamics. In the same time window, the large stars are more confined, as suggested by the presence of a plateau, whose height provides a localization length l_0 that is equal to that of the single glass. This is in agreement with the MCT predictions discussed above, which suggest that the glassy properties of the large stars are unchanged, in terms of non-ergodicity parameter and localization length, upon moderate addition of small stars of different size. For the small stars we can deduce instead a localization length of the order of $0.5\sigma_1$, about twice as large as that of the large stars, again in agreement with MCT predictions.

Looking at the partial density correlators for the double glass in Figure 4.10, we see a close similarity for the large stars correlators to those of the single glass. Only the time duration of the plateau is different, due to the relative position of the chosen state point with respect to the glass transition. Indeed, it can be seen in

Figs. 4.2 and 4.4 that this state point is ‘more liquid’ than the one we studied for the single glass. Similarly to the previous paragraph, we can analyze the decay in terms of a stretched exponential and of a von Schweidler law and the results are totally equivalent to those of the single glass for what concerns the large stars dynamics. The resulting f_q is reported in Fig. 4.11 together with corresponding critical MCT predictions in this regime.

The story is completely different for the small stars. The density correlators are not describable in terms of stretched exponentials. Indeed, they are best fitted with a $\ln(t)$ second order polynomial of Eq. (4.5), as in other systems where a competition between two glassy states originates an anomalous dynamical behavior [99–101, 107, 108]. This seems to suggest the possible existence of a MCT a higher order singularity [102]. Interestingly, the logarithmic behavior is found only for the small stars, while the large stars remain close to a standard liquid-glass transition or A_2 singularity. Indeed, small stars are those exhibiting a clear change of dynamics upon increasing ξ : from highly mobile in a frozen matrix to becoming arrested themselves, so that the logarithmic behavior could arise from a competition between these two dynamics. Although no explicit studies for binary mixtures exhibiting higher order singularities are available, we will perform further MCT analysis in the next future to study if the single-to-double glass transition is a true glass-glass transition, corresponding to two distinct solutions of MCT equations, or if it is just a smooth crossover.

Performing the fits following Eq. (4.5), we extract a non-ergodicity parameter for the small component in good agreement with the one calculated within MCT close to the liquid-glass transition ($\rho_2\sigma_1^3 = 0.05$, see Fig. 4.2). Also, by looking at the $h_q^{(2)}$ extracted from the fits, we can find out what is the optimal wave vector q^* at which the decay is purely logarithmic [102, 109]. This indicates the dominant length scale in the arrest process, and indeed it was estimated before for the attractive glass [107]. Here, $h_q^{(2)} \sim 0$ for $q\sigma_1 \approx 4$, corresponding to a length-scale slightly larger than the nearest-neighbor length for the large stars, indicating that small stars are mostly trapped between neighboring large stars. Around this q^* -value there is the expected crossover between concave and convex shape for the $\phi(q, t)$. As for the single glass case, the estimates of $f_{ij}(q)$ from the simulations differ from the MCT ones especially at low q , though the discrepancy is reduced in this case.

4.4.3 Region III: Second Double Glass

We analyze the state point $\rho_1 = 0.345$, $\rho_2\sigma_1^3 = 3.4$ and $\xi = 0.4$, where a further decrease in diffusivity is observed upon addition of small stars, as it can be seen in Fig. 4.4 .

From the MSD reported in Fig. 4.12, we see that both components exhibit a slowing down in the dynamics, therefore we have evidence of a second double glassy

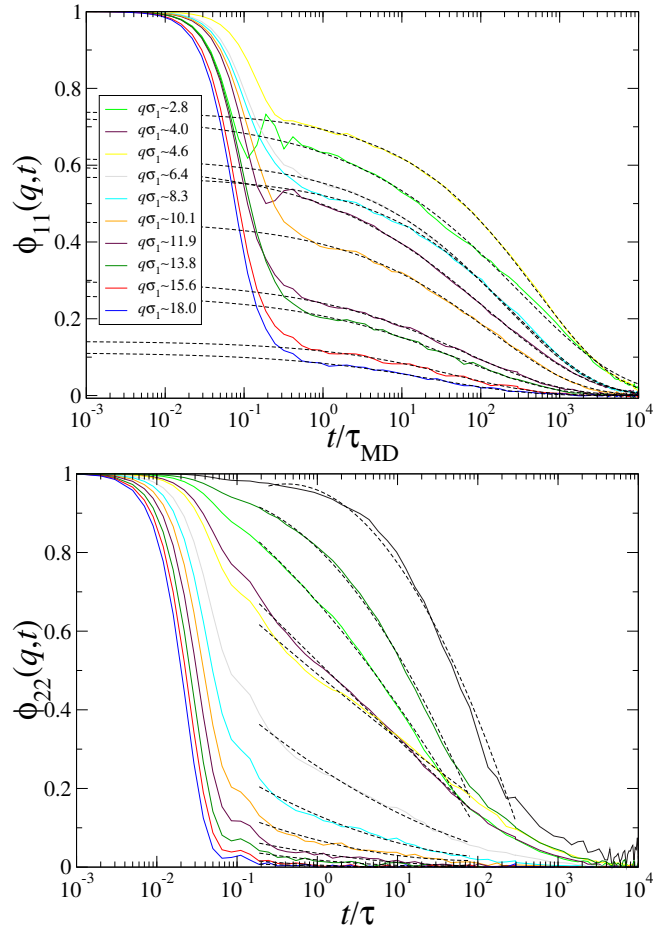


Figure 4.10: Density correlators for the large (top) and small (bottom) stars in the double glass for different values of q . The parameters are the same as in Fig. 4.9. The dashed lines for the large stars are stretched exponential fits, for the small stars we use logarithmic fits.

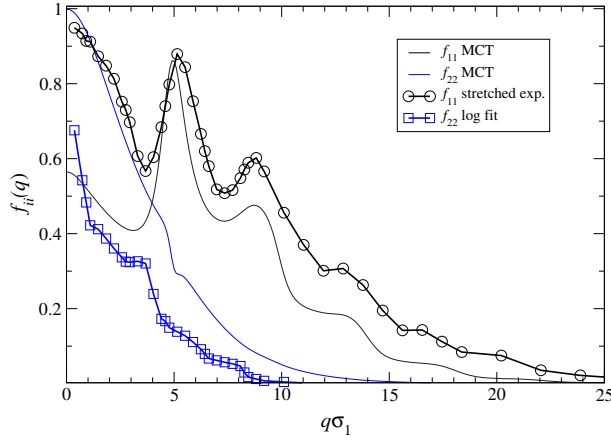


Figure 4.11: Comparison of partial non-ergodicity parameters from MCT and simulation in the double glass. The values from the simulations are obtained by stretched exponential fits for the large stars and from logarithmic fits for the small stars. The MCT results refer to critical parameters for $\rho_1\sigma_1^3 = 0.345$, $\rho_2 = 0.05$ and $\xi = 0.4$. The simulation parameters are the same as in Fig. 4.9.

state. However, the localization lengths that can be extracted from the MSD are smaller than those for the double glass discussed above. Indeed, we find $l_0 \approx 0.14$ for the large stars, corresponding to about half of the cage length that we found both in single and double glass, while $l_0 \approx 0.2$ for the small stars, again at least twice as small as that of the other (conventional) double glass. These values are again in remarkable agreement with those predicted by MCT .

The fitting procedure to the density correlators turns out to be opposite to that of the standard double glass. Indeed, we cannot fit the correlators for the large stars with stretched exponentials, but rather they are found to follow the logarithmic decay of Eq. (4.5). On the other hand, the small stars $\phi_{22}(q, t)$ are well described by a stretched exponential decay for small wave vectors, while this fitting procedure becomes unreliable at large q . The logarithmic behavior for large stars suggests the possibility of the presence of a higher order MCT singularity for the large stars or, at least, a competition between two different glassy states. Indeed, upon increasing ρ_2 at fixed $\xi = 0.4$, the large stars are passing from the standard glass to a much more localized one. The same is true for the small stars in this region, so that a similar *log*-behavior could be also, in principle, observed for the small stars for some more accurate choice of the parameters, but, within the present study, we are not able to detect that. However, we do observe here a deviation from standard stretched exponential behavior at large q even for the small stars.

From the logarithmic fits for the large stars, we find the non-ergodicity parameter

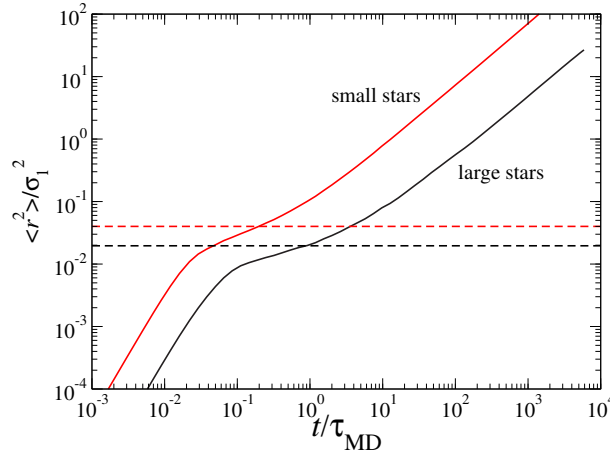


Figure 4.12: Mean squared displacement for the large and small stars in the second double glass. The densities are $\rho_1\sigma_1^3 = 0.345$ and $\rho_1\sigma_1^3 = 3.4$; the size ratio is $\xi = 0.4$.

for large stars, again in quite good agreement with MCT predictions, as shown in Fig. 4.14. Also, we can determine the q^* where the log behavior is enhanced, i.e. $q^*\sigma_1 \cong 16.6$, thus invoking smaller length scales than those of nearest-neighbor as responsible for the mechanism of arrest. We notice that this length is much smaller than that found for attractive glasses in CP mixtures [107], consistently with the fact that here no attractive bonding is present. For the small stars, the Kohlrausch fits are good at small wave-vectors, but become more uncertain for large q values. This does not allow to detect a robust b exponent to apply the Von Schweidler fits. However, the fits are good enough for a good agreement for f_q with the MCT predictions for the critical parameters $\rho_1 = 0.345$, $\rho_2 = 1.27$ and $\xi = 0.4$.

4.4.4 Region IV: Attractive Glass and Phase Separation

For large asymmetries in the size ratio we reach an increase of the small star density leads finally to an attraction between the large stars and a demixing transition [96]. Therefore the investigation of this part of the phase diagram and the study of a formation of an attractive glass is hindered by a phase separation.

Indeed, the RY closure does not allow us to investigate this part of the phase diagram as the convergence of the closure already breaks down before reaching the demixing line. An increase in the $q \rightarrow 0$ -limit is observed for all partial structure factors. However, at $\rho_2\sigma_1^3 = 4.45$ two-component MCT predicts a arrested state (see Fig. 4.2). Within one-component MCT this state is still fluid. The properties of the non-ergodicity parameters of the large stars found by binary MCT however are typical of an attractive glass.

Simulations in this part of the phase diagram are very time consuming due to the

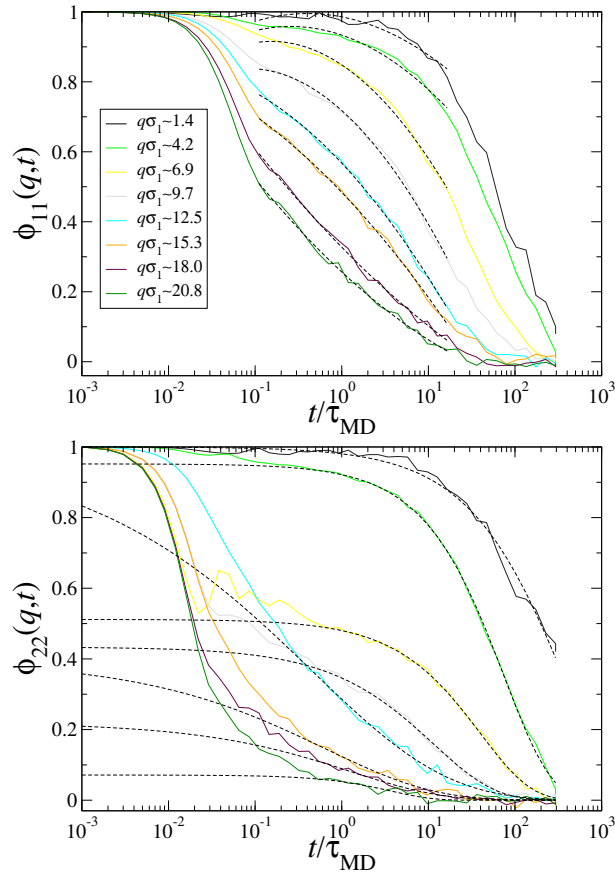


Figure 4.13: Density correlators for the large (top) and small (bottom) stars in the second double glass for different values of q . The parameters are the same as in Fig. 4.12. Here the large stars are described by logarithms, for the small ones we use stretched exponentials.

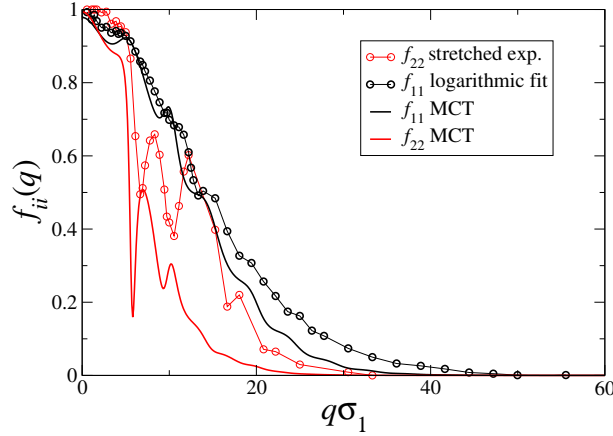


Figure 4.14: Comparison of non-ergodicity parameters from MCT and simulation in the second double glass. The values from the simulations are obtained by logarithmic fits for large stars and stretched exponentials for small stars. The simulation parameters are the same as in Fig. 4.9.

large density ratio investigated. A decrease of the diffusivity of the large stars was observed only for $\rho_2\sigma_1^3 \sim 15$, that means there are more than 40 times as many small as large particles in the simulation box, making it necessary to simulate a huge total number of particles. Additionally, the proximity of the demixing line even further complicates the simulation study. A detailed study of the attractive glass will be the subject of a future study.

4.5 Conclusions

Additionally to the previously found glassy states in binary star polymer mixtures we find new arrested states at high density of the smaller additives. These arrested states are found within the framework of mode coupling theory as well as in MD simulations. Indeed, the iso-diffusivity lines from the simulations capture the features of the ideal MCT transition line. The dynamical properties of these arrested states, however, are clearly distinct. In the simulations we find density correlators that show the typical stretched exponential behavior as well as logarithmic decays, as predicted by MCT in the vicinity of a higher order singularity. The non-ergodicity parameters extracted from the simulation data are in qualitative agreement with the MCT results.

Chapter 5

Ultrasoft Systems with Attractive Interactions

In this chapter we are dealing with star polymers with explicit attractive interactions. In the first part, we study a one-component model for star polymer solutions with competing attractive and repulsive interactions. In the second part, we investigate the conformations of star polymers with attractive end groups, so called telechelic or end-functionalized star-polymers, in dilute solution.

5.1 Attractive Forces in Star Polymer Solutions

5.1.1 Theoretical Model

There are several origins of attractive forces in star polymers solutions. One possibility is the introduction of depletants, e.g. polymers or star polymers, with a smaller size than the main component (see Secs. 2.2.3 and 2.5, [28, 32, 44, 96]). As we have seen, the attraction can be influenced by modifying the softness and/or size of the depletants. In this case, as for purely repulsive stars, the interaction is entropic and thus the system is athermal. The interaction between the stars acquires a dependence on the depletant concentration which can be interpreted as an inverse temperature.

A second possibility is to consider residual dispersion forces in solution due to a non-perfect matching of the refraction index between solute and solvent. Here the attractive forces can be influenced by screening the dipole-dipole interaction through addition of salt, which remains mainly in the intermolecular space, not affecting therefore the conformation of the stars. The system is not athermal. For this case we concentrated on intermediate/small functionality stars described in terms of a one component model potential, discussing the phase diagram and the

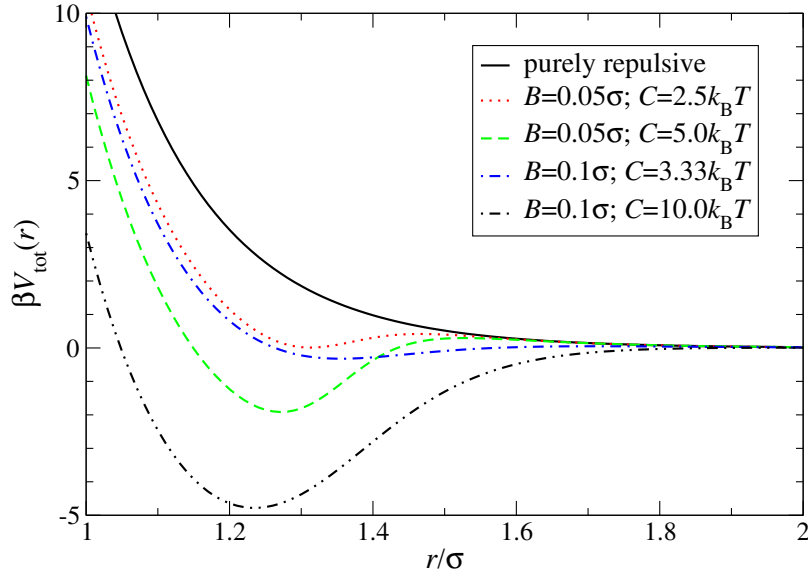


Figure 5.1: Total interaction potential between the stars as a function of the center-to-center distance. It is $A = 1.35\sigma$ and $f = 32$ for all curves, the other parameters are indicated in the legend.

dynamics. In the following we will study a system with an effective one-component interaction which mimics these effects.

Again, we start from the repulsive star-star interaction given by Eq. (2.3). Figs. 2.3 and 2.10 show the modification of the effective interaction adding polymer chains to a star solution. Similar effects have been found for binary star polymer solutions [96]. Depending on the composition of the mixture, very different interactions can be obtained which cause a rich equilibrium and non-equilibrium behavior. As we have seen, for different parameter combinations the mixture exhibits micro- or macrophase separation. Lo Verso *et al.* proposed a simple one-component potential to describe such depletion effects [110]. This potential was used to study fluid-fluid demixing [110] and dynamical arrest for stars with intermediate functionalities ($50 < f < 100$) [111]. A shift of the glass transition lines to higher densities was observed. Recently, the same model was used to study cluster formation in low-functionality star polymers ($f = 32$) [112]. Here, we use this modeling to describe the vitrification of low-functionality star polymers with short-range attractions.

The attractive contribution is chosen to have the same functional form as a Fermi distribution, i.e.

$$V_{\text{attr}}(r) = -\frac{C}{\exp[(r - A)/B] + 1}. \quad (5.1)$$

A and B determine the width and the position of the minimum of the potential.

C sets the strength of the attraction. This simple model can be used to describe dispersion or depletion effects. Since the attractive part of the interaction is not entropic, the system depends on the temperature. However, when we deal with depletion effects, we can interpret T as the inverse depletant density. Attraction range and depth depend on size and concentration of the depletants in this case.

The total interaction potential is then given by

$$V_{\text{tot}}(r) = V_{\text{ss}}(r) + V_{\text{attr}}(r), \quad (5.2)$$

where $V_{\text{ss}}(r)$ is the plain star-star interaction which is given by equation (2.3). In the following, we keep A fixed at $A = 1.35\sigma$ and vary B and C to study the dynamic properties of the system. The functionality is kept constant at $f = 32$. The total potential for several parameter combinations is shown in Fig. 5.1. As can be seen in the figure, the potential displays short range attractions and long range repulsions. Indeed, the interplay of the repulsive and attractive parts of the potential leads to cluster formation also in this model [112].

5.1.2 Mode Coupling Results

The structure of the star polymer solution was calculated using the modified hypernetted chain (MHNC) closure (see Appendix A). These were used to determine the freezing line according to the Hansen-Verlet criterion [113], i.e. the lines where the main peak of the structure factor exceeds a value of 2.85. Moreover, we used the structures factor as input to calculate the nonergodicity parameters with MCT.

In Figure 5.2, we show typical repulsive glass non-ergodicity factors for different temperatures, densities and values of B . We added the ideal MCT transition lines to the phase diagram presented in Ref. [112]. As can be seen from the figure, the arrested region of the phase diagram shrinks as B is increased. This arrested state is completely absent for purely repulsive star polymers [27], where an arrested state is only found for higher functionalities. Accordingly, the arrested region vanishes for high temperatures.

Additionally, in Ref. [114] Brownian dynamics simulations [115] were performed in order to determine the long-term self diffusion coefficient of the system. It was found that the additional long-range repulsion leads to a dramatic slowing down of the dynamics, which is absent for systems which do not exhibit this repulsion. The region of the phase diagram corresponds to the one where MCT predicts an arrested state.

As already stated, in these systems the strength of the attraction and the long range repulsion become stronger on decreasing the temperature and the value of B . Moreover, the range of the attraction decreases with B . As a consequence, in the arrested region, the first shell of neighbors progressively becomes more localized

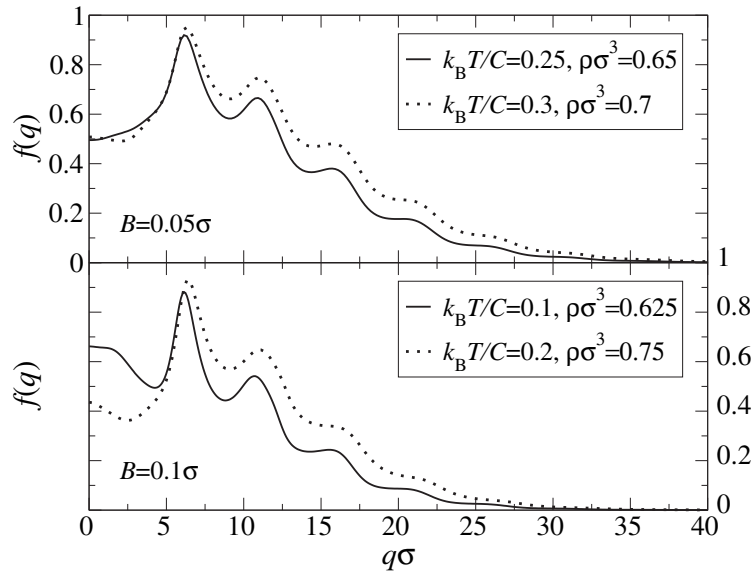


Figure 5.2: Typical examples of nonergodicity parameters for low-functionality star polymers with attractions.

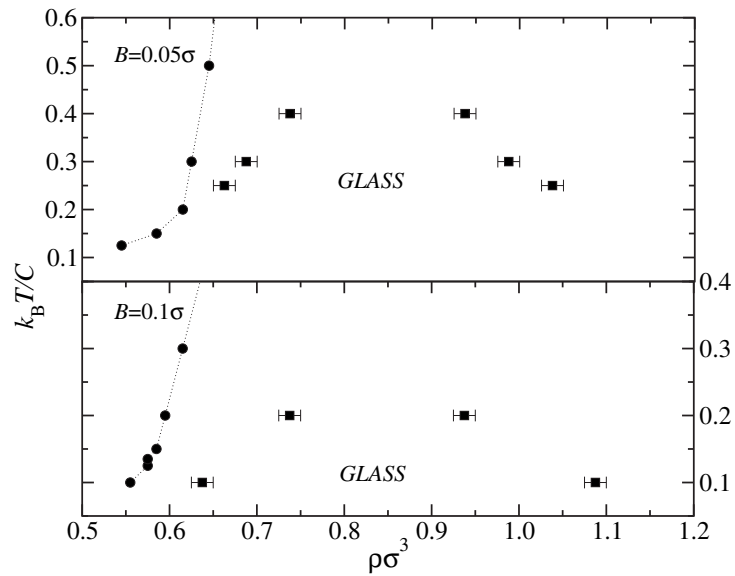


Figure 5.3: Glass region for the studied system. The squares denote the nonergodicity transition, the circles the Hansen-Verlet line from Ref. [112].

in the minimum of the well potential while the second-neighbor shell experiences an increase of the repulsive barrier. These effects stabilize the cage and lead to a slowing down of the dynamics.

5.1.3 Conclusions

We have shown that the interplay of long-range repulsion and short-range attraction in star polymers changes the dynamics fundamentally. This opens new ways to steer the rheological behavior of soft colloidal dispersions. The nature of this previously unknown arrested state and possible glass/glass transitions remain a challenging task for future investigations. Moreover, an experimental study of mixtures low-functionality star-polymers and polymer chains might be able to verify this new phenomenon.

5.2 Collapse of Telechelic Star Polymers

Conformational properties of star-shaped polymer aggregates that carry attractive end-groups are investigated by simulation and analytical theory. We focus on the case of low telechelic star polymer functionalities, $f \leq 5$, a condition which allows aggregation of all attractive monomers on one site. By performing extensive computer simulations and introducing a variational free energy expression for the conformations, we establish the functionality- and polymerization-number dependence of the transition temperature from the “star burst” to the “water melon” macroparticle structure. Extensions to multi-armed telechelic star polymers that feature partially collapsed configurations are also discussed.

5.2.1 Introduction

Self-organizing soft materials are relevant in developing novel macromolecular compounds with peculiar structural and dynamical properties, which are related to mesoscopic aggregation as well as intra- and inter-molecular association [116, 117]. In this context, progresses in the synthesis of well-characterized chains with attractive end-groups, called *telechelic polymers*, allowed the study of star polymers with attractive polar end groups, telechelic associating polymers with hydrophobic terminal groups, associating polyelectrolytes in homogeneous solutions, and telechelic planar brushes [118–121]. The thermodynamics and the structure of planar telechelic brushes have been recently analyzed also from a theoretical point of view, shedding light into the quantitative characteristics of both the conformations and the interactions of the same [122–124]. Further theoretical approaches have been developed to describe flower-like micelles with hydrophobic terminal groups that self-assemble

in water. Such aggregates show a characteristic ‘bridging attraction’ [122,125] that can even lead to a liquid-vapor phase transition [126]. The interesting feature of telechelic star polymers is the possibility of attachment between the attractive terminal groups. In dilute solutions, this gives rise to intra-molecular association as well as inter-association between micelles, depending on the details of the molecular structure. Examples of low-functionality telechelic stars, very similar to the ones considered in this work, are mono-, di-, and tri- ω -zwitterionic, three-arm star symmetric polybutadienes. Experiments have shown that these self-assemble into distinct supramolecular structures, including collapsed, soft-sphere conformations [119,127]. In particular, using low-angle laser light scattering and dynamic light scattering, it was found that samples with three zwitterion end groups present a low degree of inter-association between macromolecules, showing instead a preference for intra-association and formation of collapsed soft spheres [118,128]. X-ray scattering and rheological experiments support the conclusion that this tendency persists at higher concentrations, all the way into the melt [119]. There, the formation of transient gels has been found for the case of two- and three-zwitterion macromolecules, with the network characteristics depending on the molecular weight of the arms [127].

The conformations of telechelic micelles are evidently determined by the competition between entropic and energetic contributions. A detailed investigation, by theory and simulation, of the mechanisms leading to the formation of collapsed soft spheres is, however, still lacking. In this section we perform extensive computer simulations, accompanied by a scaling analysis of the free energies of candidate structures of telechelic micelles with small functionality, $f \leq 5$. We find that at high temperatures the system assumes the usual star burst (*sb*) configuration. On the contrary, at sufficiently low temperatures, the end-monomers attach to each other and the micelles assume an overall closed configuration, akin to the collapsed soft spheres conjectured in the experimental study of Ref. [119]. Due to the peculiar shape of these aggregates, featuring two points of aggregation, one at each end, we term them “water melons” (*wm*). For intermediate temperatures, the macromolecules exhibit several configurations that correspond to a partial assembling of the terminal groups. The number of chains connected at their ends depends on the temperature T , the functionality f and the degree of polymerization N (molecular weight) of the chains. In particular, at a given, sufficiently low T , the *wm*-configuration becomes more stable with respect to the *sb*-one with decreasing N and increasing f , as will be demonstrated in what follows. Our theoretical predictions are found to agree well with simulation results.

5.2.2 Molecular Dynamics simulations

We employed monomer-resolved molecular dynamics simulations to examine the conformations of isolated telechelic micelles. We use the same simulation model

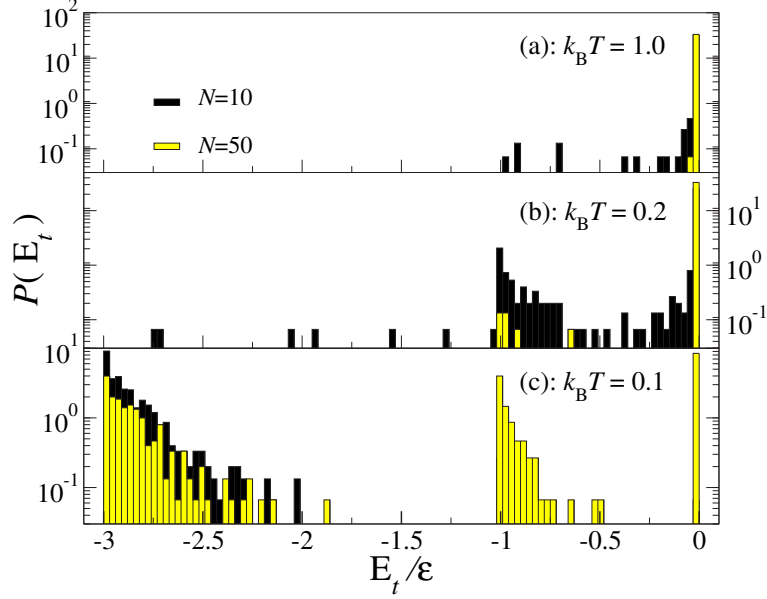


Figure 5.4: The probability distribution function $P(E_t)$ obtained from simulations of $f = 3$ telechelic micelles carrying $N = 10$ and $N = 50$ monomers per arm. Note the logarithmic scale.

as in Sec. 2.4.1. The pair interaction between the terminal monomer of each arm, however, is given by a full Lennard-Jones potential:

$$\beta V_{tt} = 4\epsilon \left[\left(\frac{\sigma_{\text{LJ}}}{r} \right)^{12} - \left(\frac{\sigma_{\text{LJ}}}{r} \right)^6 \right]. \quad (5.3)$$

The time step was $\Delta t = 10^{-3}\tau$, with a total of 2×10^5 time steps used for equilibration and 5×10^7 to gather statistics. The characteristic quantities measured in the simulation were the radius of gyration R_g of the molecules, the radial distribution function $g_t(r)$ between the terminal monomers as well as the expectation value E_t of the interaction energy between the terminal groups. The latter quantity is defined via

$$E_t = \left\langle \sum_{i=1}^f \sum_{j>i} V_{\text{LJ}}(|\mathbf{r}_i - \mathbf{r}_j|) \right\rangle, \quad (5.4)$$

where $\langle \dots \rangle$ denotes a statistical average and \mathbf{r}_i stands for the coordinates of the end monomer of the i -th chain.

We considered temperatures between $k_{\text{B}}T = 0.01\epsilon$ and $k_{\text{B}}T = 1.2\epsilon$. For $k_{\text{B}}T \gtrsim 0.2\epsilon$, we found that the micelle configuration is similar to that of a star polymer

without attractive ends, i.e., the aforementioned *sb*-configuration. However, a morphological transition of the micelles takes place upon lowering the temperature. In Fig. 5.4 we show the probability distribution function $P(E_t)$ for the end-monomer interaction energy E_t for the case $f = 3$, at different temperatures and number of monomers. At $k_B T = 1.0\epsilon$, Fig. 5.4(a), $P(E_t)$ shows almost all the events around $E_t = 0$, meaning that in the vast majority of configurations the end-monomers are sufficiently far apart, so that the attractions are vanishing. For $k_B T = 0.2\epsilon$, Fig. 5.4(b), $P(E_t)$ takes a bimodal form with two peaks, one at $E_t = 0$ and one at $E_t = -\epsilon$. The latter corresponds to a conformation in which two chains are end-attached, with their terminal monomers at a distance r_{\min} , whereas the third chain is still free (intermediate configuration). Note that the molecule does fluctuate between the two conformations, as witnessed both by the bimodal character of the probability distribution and by the non-vanishing values of $P(E_t)$ for $-\epsilon < E_t < 0$. Upon further lowering of the temperature at $k_B T = 0.1\epsilon$, Fig. 5.4(c), $P(E_t)$ develops a peak at $E_t = -3\epsilon$, corresponding to a configuration in which *all three* terminal monomers are confined at a distance r_{\min} from each other. This is the state in which the micelle has aggregation points at both ends, which we termed ‘water melon’ (*wm*)-conformation. The trend described above, is qualitatively the same for the different N . However in each panel we can notice a higher probability to have a *wm* decreasing the number of monomers. For fixed N the probability increases with the arm number. We further find a considerable sharpening of the peak at $E_t = -3\epsilon$ for lowered temperature since fluctuations around the ground state are getting more suppressed. Similar results have been found for the cases $f = 2, 4$, and 5. The minimum value of E_t for $f = 2$ is $-\epsilon$ and for $f = 4$ it is -6ϵ , corresponding to a *wm*-configuration in which *every* end-monomer is confined at a distance r_{\min} from every other one, i.e., an arrangement at the vertices of a regular tetrahedron of edge length r_{\min} . Due to geometrical constraints, for $f = 5$ it is not possible to have all five end-monomers at contact with each other; the minimum value assumed E_t is -9ϵ in this case, corresponding to the arrangement of the terminal segments on the vertices of *two* regular tetrahedra of edge length r_{\min} , which share a common face.

The temperature dependence of the gyration radius R_g for fixed $N = 10$ and different f -values is shown in the main plot of Fig. 5.5. At high temperatures, R_g has a plateau that corresponds to *sb*-case and scales as $f^{1/5} N^{3/5}$ [15]. As T is lowered, we find a rapid decrease of R_g within a narrow temperature range and a saturation to a lower plateau value that corresponds to the size of the *wm*-configuration. The attachment of the terminal monomers leads to a shrinking of the molecule, in agreement with the experimental findings of collapsed soft-sphere conformations [119]. The *wm*-configuration persists to higher T -values upon increasing the functionality f , a trend that can be attributed to the increasingly strong attractive-energy contributions to the *wm*-free energy as f grows. In the inset of Fig. 5.5 we show the

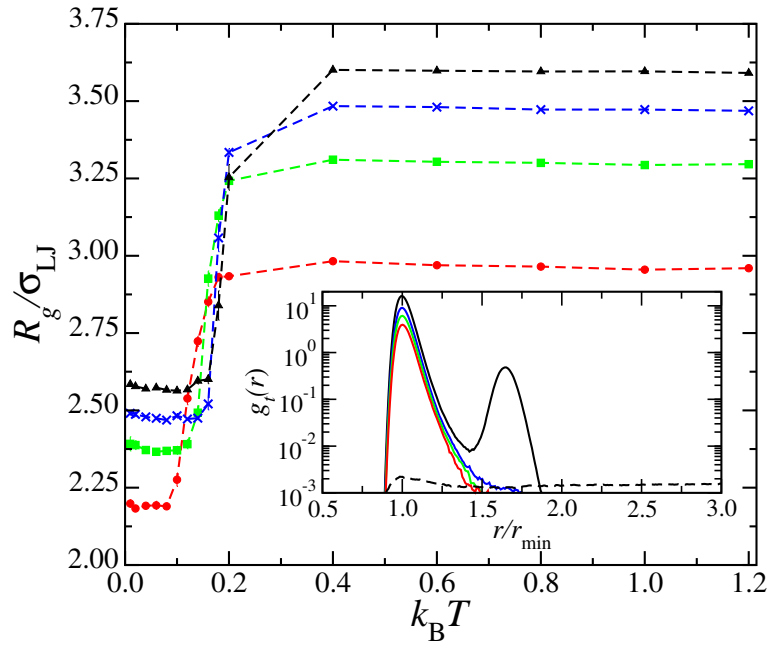


Figure 5.5: Temperature dependence of the radius of gyration R_g obtained by simulations of telechelic micelles ($N = 10$). From top to bottom: $f = 5$ (black), $f = 4$ (blue), $f = 3$ (green), and $f = 2$ (red). Inset: the end-monomer radial distribution function $g_t(r)$ obtained from simulations at $k_B T = 0.1\epsilon$ (solid curves); the sequence from top to bottom and the color coding are the same as those in the main plot. The dashed line is $g_t(r)$ for $f = 3$ and $k_B T = 1.0\epsilon$ for comparison. For clarity, each curve has been multiplied by a different, arbitrary constant.

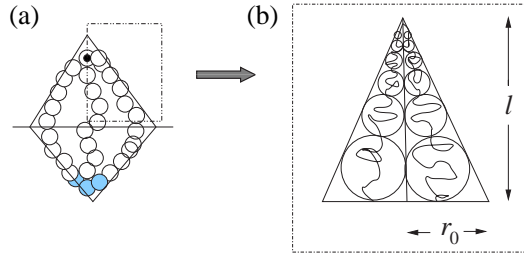


Figure 5.6: (a): Schematic representation of a water-melon with 3 arms; we depict it geometrically as a double cone of half-chains. (b): The corresponding blob model of two arbitrarily chosen, attached arms.

terminal-segment radial distribution function for the various f -values at $k_{\text{B}}T = 0.1\epsilon$, where the *wm*-conformation is stable and compare it with the one obtained for $f = 3$ at $k_{\text{B}}T = 1.0\epsilon$, where the micelles assume a *sb*-conformation. The aggregation of the end-monomers is clearly witnessed by the high peak at $r = r_{\text{min}}$, which is present at $k_{\text{B}}T = 0.1\epsilon$, as opposed by the flat shape of $g_t(r)$ at $k_{\text{B}}T = 1.0\epsilon$. Whereas for $f = 2, 3$ and 4 a single accumulation peak can be seen, a double peak is present for the case $f = 5$. This feature arises from the arrangement of the five terminal monomers at the vertices of two tetrahedra that share a common face. The most distant vertices of the two are separated by a distance $\sqrt{8/3}r_{\text{min}}$, at which indeed the second peak in $g_t(r)$ shows up.

5.2.3 Free Energy

Lo Verso *et al.* [129] proposed a scaling theory for the free energy of the two states considered. The excluded volume parameter v is set to unity, consistent with the choice $\sigma_{\text{LJ}} = 1$ above ($v \cong \sigma_{\text{LJ}}^3$). In the case of the *sb*-configuration, the free energy is entirely entropic in nature and can be expressed as a sum of the elastic and excluded-volume contributions. For a single chain, minimization of this sum with respect to the chain radius R_g leads to the scaling laws

$$R_g \sim N^{3/5} \quad (5.5)$$

and

$$F \sim k_{\text{B}}TN^{1/5}. \quad (5.6)$$

For high-functionality star polymers, Flory theory can be improved in order to better take into account the inter-chain correlations by invoking the blob model of Daoud and Cotton [15,17]. For the small f -values at hand, instead each chain was modeled as a blob of radius $\sim R_g$ that occupies a section of space delimited by a solid angle

$4\pi/f$. Accordingly, the total free energy of the sb -configuration is approximated by

$$F_{sb} = k_{\text{B}}TfN^{1/5}. \quad (5.7)$$

. The attractive, energetic contribution of the terminal monomers is very small, since the latter are far apart in the sb -state, and therefore it can be ignored.

In the wm -configuration, there are two accumulation points: the first is the point in which the chains are chemically linked and the second is at the other end, at which the end-monomers stick together. In order to properly take into account the monomer correlations within the macromolecule [130], Lo Verso *et al.* [129] employed a blob model to estimate the excluded-volume contributions to the free energy F_{wm} [123, 131]. A schematic representation of the water melon and the associated blob model are shown in Fig. 5.6(a); the wm is thereby modeled as a double cone. With r_0 and l being the radius and height of the cone that contains n_b blobs of a single chain, we obtain

$$\frac{F_{wm}}{k_{\text{B}}T} = \frac{3}{2}f\frac{r_0^2 + l^2}{N} + 2fn_b + E_{\text{attr}}. \quad (5.8)$$

The first term at the right-hand side of Eq. (5.8) above is the stretching contribution of f chains, each having an extension $\sqrt{r_0^2 + l^2}$. The second is the excluded-volume cost and arises from the total number of $2fn_b$ blobs, each contributing an amount $k_{\text{B}}T$ [123, 130, 131]. Finally the third term is the attractive energy contribution arising from the total number of contacts between terminal monomers. Accordingly,

$$E_{\text{attr}} = -\frac{f(f-1)\epsilon}{2k_{\text{B}}T} \quad (5.9)$$

for $f = 2, 3$, and 4, whereas

$$E_{\text{attr}} = -\frac{9\epsilon}{k_{\text{B}}T} \quad (5.10)$$

for $f = 5$. For given N , f , and T , F_{wm} depends variationally on r_0 , l , and n_b but two constraints must be considered. First, blobs are close-packed within each cone, hence:

$$\frac{l}{\cos(\alpha/2)} = D \sum_{n=0}^{n_b-1} \left(\frac{1 + \sin(\alpha/2)}{1 - \sin(\alpha/2)} \right), \quad (5.11)$$

where $\alpha = \arctan(r_0/l)$ and D is the diameter of the first, smallest blob, which is taken equal to the monomer size. Second, the monomer number N is obtained by summing over the monomers of all blobs of a chain, taking into account that a blob of size b contains $N_b \sim b^{5/3}$ monomers. This results into the constraint:

$$N(r_0, l) = 2D^{5/3} \sum_{n=0}^{n_b-1} \left(\frac{1 + \sin(\alpha/2)}{1 - \sin(\alpha/2)} \right)^{(5n/3)}. \quad (5.12)$$

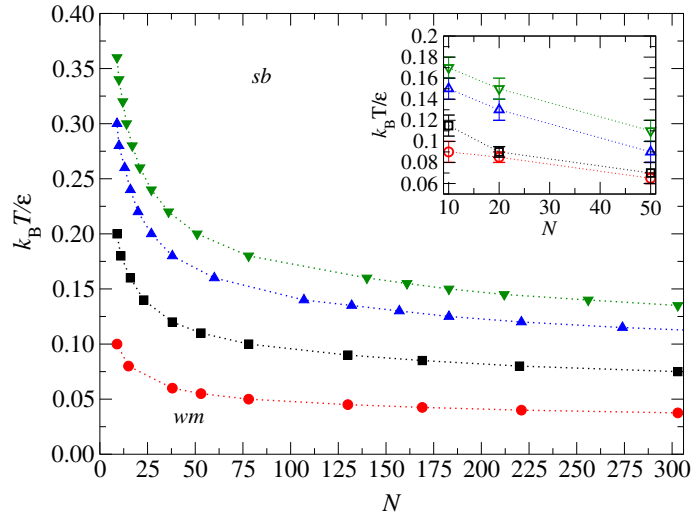


Figure 5.7: Temperature versus N diagram corresponding to the sb - and wm -morphological transitions of telechelic micelles. Main figure: theoretical results. Inset: transition lines in simulations, determined via the T dependence of R_g . From bottom to top (full/empty symbols): $f = 2$ (circle), $f = 3$ (square), $f = 4$ (triangle up), $f = 5$ (triangle down).

Eqs. (5.11) and (5.12) were solved numerically to express n_b and l in terms of r_0 and then we minimized numerically F_{wm} with respect to r_0 using Eq. (5.8). We found that the cone angle α between two arms increases rapidly with N for small N -values: for $5 \lesssim N \lesssim 20$ it changes from 20 to 40 degrees. This trend reflects the physical impossibility for the chains to form an aggregate for short chains. Once the excluded volume interactions are balanced, the angle increases slowly, by about 5 degrees for $25 \lesssim N \lesssim 400$.

Comparing the resulting, minimized free energies F_{wm} with F_{sb} , we obtained the *transition* temperature between sb and wm as a function of the degree of polymerization¹. In Fig. 5.7 we show the T vs. N transition lines, separating the wm -state (below) from the sp -one (above). The ‘critical number’ N_c increases with decreasing T . and the transition temperature increases with f . Stated otherwise, for fixed N the theoretical model gives evidence to a stronger stability of the wm configuration on increasing f and lowering the temperature. On the other hand, keeping f and T fixed, the sb -configuration is stable above a certain value of N_c . The dependence of the repulsive contribution in the free energy on the number of monomers is not trivial: increasing N , the number of blobs n_b increases and so does the contribution

¹As we are dealing with finite systems, these are not sharp transitions but rather crossover phenomena.

due to the excluded volume interaction. The entropic contribution is proportional to r_0^2 , which increases with N , and to $1/N$. The balance between all these terms in Eq. (5.8) determines the stable micelle conformation: it is physically more expensive for the molecule to assume a *wm*-configuration the lower f and the higher N is. N_c decreases rapidly with T and the *wm*-state becomes unstable for $k_B T \gtrsim 0.3\epsilon$. The inset of Fig. 5.7 show the results coming from simulation: notice the full agreement of the theoretical prediction trends. The value of transition temperature is overestimated in theory, reflecting the mean-field nature of the latter, which ignores fluctuation effects. There exist also configurations intermediate to the *wm*- and *sb*-ones, in which only a partial association of arms takes place. Such configurations are also expected to be dominant as f further increases, due to the very high entropic penalty inherent to a complete intramolecular association. These conformations can also be analyzed theoretically along the lines put forward in this work, since intermediate states can be looked upon as a combination of smaller water melons that are all attached on a common center. These are results of work which is in progress.

5.2.4 Conclusions

We have studied the dependence of the equilibrium conformations of telechelic micelles on the temperature, arm number and functionality of the same. The association number of the terminal groups is strongly temperature dependent. The system presents a stable, water-melon configuration for low temperatures that opens up as T grows. We expect that dynamical properties of such macroparticles in solution will have unusual characteristics. For instance, at low temperatures and near the overlap concentration, various types of gels can appear, owing their viscosity either to transient network formation or to the existence of entangled loops. A more accurate comprehension of the changes in the micelle conformations is a relevant starting point aiming at gaining control over the supramolecular structural and dynamical properties of the system [132]. This is an issue of major importance for molecular design, targeting specific biological and technical applications.

Chapter 6

Conclusions and Outlook

In this thesis we presented results adding to the understanding of the mechanisms leading to dynamical arrest in soft condensed matter. We focused on studies of soft colloidal mixtures. The first system that we dealt with consists of star polymers and polymer chains in a good solvent. We proposed an effective star-chain interaction and confirmed it by extensive molecular dynamics simulations. In agreement with experimental findings [32] we observed the formation of star clusters for low star concentration and low functionalities. Accordingly, the chain-mediated effective interaction between the stars exhibits a short-ranged attraction and long-ranged repulsion. However, for larger functionalities the cluster phase is completely absent. Moreover, we investigated the long-time dynamics of the system by mode coupling theory. We found polymer induced melting of the solution of glassy stars. Again, our results are in agreement with previous experimental studies [28]. However, the melting mechanism only persists up to chain sizes of about half the star sizes. Stiakakis *et al.* [28] suggested that larger chains form transient networks in the solution. It would be very interesting to study the microscopic details of the mixture in monomer resolved computer simulations. Additionally, a comparison with dynamic light scattering data from experiments would give valuable insights in the dynamics of soft colloids.

Furthermore, we studied a binary mixture of star polymers. Here the softness of the additive can also be altered, opening an additional parameter to steer the macroscopic flow of the stars. Following the experimental setup, we considered only small densities of additives. Both the rheological measurements and the theoretic calculations based on the mode coupling theory point to the existence of two clearly distinct glassy states. While the dynamics of the large stars is almost identical in both glasses, the small stars turn from a fluid in the matrix consisting of the large stars to being arrested themselves. Moreover, both theory and experiment predict the same melting behavior.

To study the dynamics of the binary star polymer system in greater detail, we

performed additional mesoscopic molecular dynamics simulations to study the full time dependence of the density correlators. The simulations confirmed the melting lines and the shape of the nonergodicity parameters from mode coupling theory. We were also able to find additional arrested states for high densities of additives. One of them has the typical features of an attractive glass [9], while the other one consists of distorted cages with low coordination which can only exist in systems with soft interactions. It will be a very interesting task to characterize the change in local order which brings about the anisotropy. Moreover, experimental studies for high densities of additives would be important in order to verify the simulation results. Additionally, it would be interesting to abandon athermal solvents and study the influence of solvent quality on the properties.

Furthermore, we studied a one-component model of star polymers with competing short range attraction and long range repulsion. The additionally induced local order brings about arrested states even for very low functionalities. Finally, we investigated star polymers with attractive end groups in dilute solution by simulations. Changes of the temperature cause a collapse of the stars to dense water-melon structures. The phase behavior of such telechelic micelles for finite concentrations, especially focusing on bridging attractions and phase separation, will constitute a very interesting field of research in the future.

Appendix A

Ornstein-Zernike Equation for Binary Mixtures

In the two-component case the Ornstein-Zernike (OZ) equation reads as [33]:

$$\tilde{\mathbf{H}}(q) = \tilde{\mathbf{C}}(q) + \tilde{\mathbf{C}}(q) \cdot \mathbf{D} \cdot \tilde{\mathbf{H}}(q), \quad (\text{A.1})$$

where $\tilde{\mathbf{H}}(q)$ and $\tilde{\mathbf{C}}(q)$ are symmetric 2×2 matrices with

$$[\tilde{\mathbf{H}}(q)]_{ij} = \tilde{h}_{ij}(q) \quad \text{and} \quad [\tilde{\mathbf{C}}(q)]_{ij} = \tilde{c}_{ij}(q). \quad (\text{A.2})$$

\mathbf{D} is a diagonal 2×2 matrix containing the number densities $\rho_i = N_i/V$ of the two species

$$[\mathbf{D}]_{ij} = \rho_i \delta_{ij}. \quad (\text{A.3})$$

The total correlation functions $h_{ij}(r)$ ($i, j = 1, 2$) are related to the radial distribution functions via $h_{ij}(r) = g_{ij}(r) - 1$, whereas the $c_{ij}(r)$ are the direct correlation functions of the system.

Due to the symmetry of the interactions it holds $h_{ij}(r) = h_{ji}(r)$. Therefore the OZ equation (A.1) provides three equations for the six unknown functions $h_{ij}(r)$ and $c_{ij}(r)$. In order to compute these functions, we need additional three closure equations. For the kind of soft mixtures we investigate, the Rogers-Young closure turns out to be very accurate. In the multicomponent version it reads as [16]:

$$g_{ij}(r) = \exp[-\beta V_{ij}(r)] \left[1 + \frac{\exp[\gamma_{ij}(r)f(r)] - 1}{f(r)} \right]. \quad (\text{A.4})$$

Here $\gamma_{ij}(r) = h_{ij}(r) - c_{ij}(r)$ and $f(r) = 1 - \exp(-\alpha r)$ ($\alpha > 0$). The value for the parameter α is determined by requiring the equality of the ‘fluctuation’ and ‘virial’ total compressibilities of the system [66, 96]. For $\alpha \rightarrow 0$ one obtains the Percus-Yevick closure, for $\alpha \rightarrow \infty$ the hypernetted chain closure.

In order to obtain thermodynamic consistency, we have to calculate the compressibilities. The total pressure of the system is given by [133]

$$\beta P = \rho - \frac{2\pi}{3} \sum_i \sum_j \rho^2 x_i x_j \int_0^\infty dr r^3 \frac{\partial V_{ij}(r)}{\partial r} g_{ij}(r), \quad (\text{A.5})$$

where ρ is the total number density and the x_i are the partial concentrations $x_i = \rho_i/\rho$. By differentiation of the pressure with respect to the total density ρ at fixed x_i we obtain the virial compressibility:

$$\rho k_B T \kappa_T^{\text{vir}} = \left[\frac{\partial \beta P}{\partial \rho} \right]^{-1}. \quad (\text{A.6})$$

Another possibility to calculate the compressibility of the mixture is based on the structure factors of the system, which are defined as

$$S_{ij}(q) = \delta_{ij} + \sqrt{\rho_i \rho_j} \tilde{h}_{ij}(q). \quad (\text{A.7})$$

For binary mixtures, the fluctuation compressibility is given by [134]:

$$\rho k_B T \kappa_T^{\text{fl}} = \frac{S_{11}(0)S_{22}(0) - S_{12}^2(0)}{x_2 S_{11}(0) + x_1 S_{22}(0) - s \sqrt{x_1 x_2} S_{12}(0)}. \quad (\text{A.8})$$

The other closure we used in this thesis for one-component systems is the modified hypernetted chain (MHNC) closure. In general, every closure can be written in the form [33]

$$g(r) = \exp[-\beta V(r) + h(r) - c(r) + B(r)], \quad (\text{A.9})$$

where $B(r)$ is the bridge function, which is in general not known. In the MHNC, $B(r)$ is approximated by the bridge function of hard spheres with diameter d . The parameter d is determined by minimizing the free energy [135] via the relation

$$\int d^3r [g(r) = g_{\text{HS}}(r, \eta_{\text{HS}})] \frac{\partial N_{\text{HS}}(r, \eta_{\text{HS}})}{\eta_{\text{HS}}} = 0, \quad (\text{A.10})$$

where $\eta_{\text{HS}} = \pi \rho d^3/6$, with ρ denoting the density. For the hard sphere radial distribution function we use the parametrization of Verlet and Weis [136].

Appendix B

Mode Coupling Theory

Our theoretical study of the glass transition is based on the ideal Mode Coupling Theory (MCT), a theory that describes the time evolution of the density autocorrelation functions, starting only from the knowledge of the static structure factors, via a set of coupled integro-differential equations [3]. The normalized time-dependent collective density autocorrelation functions are defined as,

$$\phi_{ij}(q, t) = \langle \rho_i^*(q, 0) \rho_j(q, t) \rangle / \langle \rho_i^*(q, 0) \rho_j(q, 0) \rangle, \quad (\text{B.1})$$

where

$$\rho_j(q, t) = \sum_{l=1}^{N_j} \exp \left[i \mathbf{q} \cdot \mathbf{r}_l^{(j)}(t) \right],$$

with $\mathbf{r}_l^{(j)}$ the coordinates of the l -th particle of species j ($j = 1, 2$) and the asterisk denotes the complex conjugate. It is also useful to focus on the self part of the density correlation functions, which describes the dynamics of a tagged particle,

$$\phi_j^s(q, t) = \left\langle \sum_{l=1}^{N_j} \exp \left\{ i \mathbf{q} \cdot \left[\mathbf{r}_l^{(j)}(t) - \mathbf{r}_l^{(j)}(0) \right] \right\} \right\rangle. \quad (\text{B.2})$$

The long-time limit value of $\phi_{ij}(q, t)$, i.e. the partial non-ergodicity factor, respectively for the collective and self correlation functions, is defined as,

$$f_{ij}(q) = \lim_{t \rightarrow \infty} \phi_{ij}(q, t) \quad (\text{B.3})$$

$$f_j^s(q) = \lim_{t \rightarrow \infty} \phi_j^s(q, t). \quad (\text{B.4})$$

A glass transition is identified within MCT as an ergodic to non-ergodic transition, when the non-ergodicity factor discontinuously jumps from zero, typical of a fluid, to a finite value typical of a glass [3].

In binary mixture for large size asymmetries, there is a vast separation of time-scales between large (species 1) and small (species 2) stars due to the enormous difference in masses. Therefore we can use one-component MCT for the large stars only, and solve the equation for the non-ergodicity parameter $f_{11}(q)$,

$$\frac{f_{11}(q)}{1 - f_{11}(q)} = \frac{1}{2} \int \frac{d^3k}{(2\pi)^3} V(\mathbf{q}, \mathbf{k}) f_{11}(k) f_{11}(|\mathbf{q} - \mathbf{k}|), \quad (\text{B.5})$$

with

$$\begin{aligned} V(\mathbf{q}, \mathbf{q}) &= \frac{\rho_1}{q^4} [\mathbf{q} \cdot (\mathbf{q} - \mathbf{k}) \tilde{c}_{11}(|\mathbf{q} - \mathbf{k}|) + \mathbf{q} \cdot \mathbf{k} \tilde{c}_{11}(k)] \\ &\times S_{11}(q) S_{11}(k) S_{11}(|\mathbf{q} - \mathbf{k}|), \end{aligned} \quad (\text{B.6})$$

where $\tilde{c}_{11}(q)$ is the Fourier transform of the direct correlation function of the large stars. The solution with the largest $f_{11}(q)$ is the real long-time limit [3] of the density correlators. We note here that, in the one-component effective treatment of the binary mixture, we use $S_{11}(q)$ calculated still from solving the binary OZ equation within RY closure, arising from the full binary interactions of the studied model. In this respect, we are treating the small stars as an effective medium, and their influence on the interactions between the large stars is taken into account explicitly and not through an effective one-component picture [96].

MCT assumes on a vast separation of time scales between the slow and fast degrees of freedom. For smaller size asymmetries, the separation of timescales between the different star species decreases and one-component MCT cannot be used [72]. In the general case of a mixture, when relaxation time-scales are comparable, MCT equations are easily generalized [137, 138]. In the two-component description, we include all the partial structure factors [137]. We have to consider a 2×2 matrix $\bar{\mathbf{f}}$ of the partial non-ergodicity parameters:

$$[\bar{\mathbf{f}}(q)]_{ij} = f_{ij}(q).$$

The long-time limit is in this case given by

$$\bar{\mathbf{f}}(q) = \bar{\mathbf{S}}(q) - \{\bar{\mathbf{S}}(q)^{-1} + \mathcal{F}(\bar{\mathbf{f}}, q)\}^{-1}, \quad (\text{B.7})$$

where the matrix $\bar{\mathbf{S}}(q)$ depends on the partial structure factors in the form

$$[\bar{\mathbf{S}}(q)]_{ij} = \sqrt{x_i x_j} S_{ij}(q), \quad (\text{B.8})$$

where $x_i = N_i/(N_1 + N_2)$ is the number concentration of species i . The functional $\mathcal{F}(\bar{\mathbf{f}}, q)$ is defined as

$$\begin{aligned} \mathcal{F}_{ij}(\bar{\mathbf{f}}, q) &= \frac{1}{2q^2} \frac{\rho}{x_i x_j} \sum_{mnm'n'} \int \frac{d^3k}{(2\pi)^3} V_{imm'}(\mathbf{q}, \mathbf{k}) \\ &\times f_{mn}(k) f_{m'n'}(p) V_{jnn'}(\mathbf{q}, \mathbf{k}), \end{aligned} \quad (\text{B.9})$$

with $\rho = \rho_1 + \rho_2$. The vertices $V_{imm'}(\mathbf{q}, \mathbf{k})$ depend on the equilibrium structure of the system and are given by

$$V_{imm'}(\mathbf{q}, \mathbf{k}) = \frac{\mathbf{q} \cdot \mathbf{k}}{q} \tilde{c}_{im}(k) \delta_{im'} + \frac{\mathbf{q} \cdot (\mathbf{q} - \mathbf{k})}{q} \tilde{c}_{im'}(|\mathbf{q} - \mathbf{k}|) \delta_{im}.$$

In the case of binary or multicomponent MCT, the theory predicts, through the couplings between species in Eq. (B.7) a simultaneous jump from zero to a finite value for all partial collective non-ergodicity parameters $f_{ij}(q)$. However, this does not hold for the self $f_i^s(q)$, for which the equations are [92],

$$K_i(q) = \frac{1}{\rho_i q^2} \sum_{j,k} \int \frac{d^3 q'}{(2\pi)^3} f_i^s(|\mathbf{q} - \mathbf{q}'|) \tilde{c}_{ij}(q') \tilde{c}_{ik}(q') \sqrt{S_{jj}(q') S_{kk}(q')} f_{jk}(q'), \quad (\text{B.10})$$

where

$$f_i^s(q) = \frac{1}{1 + q^2/K_i(q)}, \quad (\text{B.11})$$

so that it is possible to distinguish also the case of mobile particles in a frozen environment, for example for the small stars in our case, when $f_{22}(q) \neq 0$ but $f_{22}^s(q) = 0$ [91, 92].

Bibliography

- [1] R. J. Hunter, *Foundations of Colloid Science*, Oxford University Press, Oxford, 2 edition, 2001.
- [2] W. B. Russell, D. A. Saville, and W. R. Schowalter, *Colloidal Dispersions*, Cambridge University Press, Cambridge, 1989.
- [3] W. Götze, Aspects of Structural Glass Transitions, in *Liquids, Freezing and Glass Transition*, edited by J.-P. Hansen, D. Levesque, and J. Zinn-Justin, p. 287, North-Holland, Amsterdam, 1991.
- [4] F. Sciortino and P. Tartaglia, *Adv. Phys.* **54**, 471 (2005).
- [5] C. N. Likos, *Soft Matter* **2**, 478 (2006).
- [6] G. Bryant, S. R. Williams, L. Qian, I. K. Snook, E. Perez, and F. Pincet, *Phys. Rev. E* **66**, 060501(R) (2002).
- [7] B. J. Alder and T. E. Wainwright, *J. Chem. Phys* **27**, 1208 (1957).
- [8] P. N. Pusey and W. van Meegen, *Nature* **320**, 340 (1986).
- [9] K. A. Dawson, G. Foffi, M. Fuchs, W. Götze, F. Sciortino, M. Sperl, P. Tartaglia, T. Voigtmann, and E. Zaccarelli, *Phys. Rev. E* **63**, 011401 (2001).
- [10] K. N. Pham, A. M. Puertas, J. Bergholtz, S. U. Egelhaaf, A. Moussaid, P. N. Pusey, A. B. Schofield, M. E. Cates, M. Fuchs, and W. C. K. Poon, *Science* **296**, 104 (2002).
- [11] T. Eckert and E. Bartsch, *Phys. Rev. Lett.* **89**, 125701 (2002).
- [12] A. M. Puertas, M. Fuchs, and M. E. Cates, *Phys. Rev. Lett.* **88**, 098301 (2002).
- [13] E. Zaccarelli, G. Foffi, K. A. Dawson, S. V. Buldyrev, F. Sciortino, and P. Tartaglia, *Phys. Rev. E* **66**, 041402 (2002).

-
- [14] G. S. Grest, L. J. Fetters, J. S. Huang, and D. Richter, *Adv. Chem. Phys.* **XCIV**, 67 (1996).
- [15] M. Daoud and J. P. Cotton, *J. Phys. (Paris)* **43**, 531 (1982).
- [16] C. N. Likos, *Phys. Rep.* **348**, 261 (2001).
- [17] T. A. Witten and P. A. Pincus, *Macromolecules* **19**, 2509 (1986).
- [18] C. N. Likos, H. Löwen, M. Watzlawek, B. Abbas, O. Jucknische, J. Allgaier, and D. Richter, *Phys. Rev. Lett.* **80**, 4450 (1998).
- [19] M. Watzlawek, C. N. Likos, and H. Löwen, *Phys. Rev. Lett.* **82**, 5289 (1999).
- [20] T. A. Witten, P. A. Pincus, and M. E. Cates, *Europhys. Lett.* **2**, 137 (1986).
- [21] J. Bang, T. P. Lodge, X. H. Wang, K. L. Brinker, and W. R. Burghardt, *Phys. Rev. Lett.* **89**, 215505 (2002).
- [22] T. P. Lodge, J. Bang, M. J. Park, and K. Char, *Phys. Rev. Lett.* **92**, 145501 (2004).
- [23] J. Bang and T. P. Lodge, *Phys. Rev. Lett.* **93**, 245701 (2004).
- [24] M. Laurati, J. Stellbrink, R. Lund, D. Richter, and E. Zaccarelli, *Phys. Rev. Lett.* **94**, 195504 (2005).
- [25] D. Vlassopoulos, G. Fytas, T. Pakula, and J. Roovers, *J. Phys.: Condens. Matter* **13**, R855 (2001).
- [26] M. Kapnistos, D. Vlassopoulos, G. Fytas, K. Mortensen, G. Fleischer, and J. Roovers, *Phys. Rev. Lett.* **85**, 4072 (2000).
- [27] G. Foffi, F. Sciortino, P. Tartaglia, E. Zaccarelli, F. Lo Verso, L. Reatto, K. A. Dawson, and C. N. Likos, *Phys. Rev. Lett.* **90**, 238301 (2003).
- [28] E. Stiakakis, D. Vlassopoulos, C. N. Likos, J. Roovers, and G. Meier, *Phys. Rev. Lett.* **89**, 208302 (2002).
- [29] A. Jusufi, M. Watzlawek, and H. Löwen, *Macromolecules* **32**, 4470 (1999).
- [30] A. A. Louis, P. G. Bolhuis, and J.-P. Hansen, *Phys. Rev. E* **62**, 7961 (2000).
- [31] A. A. Louis, P. G. Bolhuis, J.-P. Hansen, and E. J. Meijer, *Phys. Rev. Lett.* **85**, 2522 (2000).

-
- [32] E. Stiakakis, G. Petekidis, D. Vlassopoulos, C. N. Likos, H. Iatrou, N. Hadjichristidis, and J. Roovers, *Europhys. Lett.* **72**, 664 (2005).
- [33] J. P. Hansen and I. R. MacDonald, *Theory of Simple Liquids*, Academic, London, 3 edition, 2006.
- [34] A. Stradner, H. Sedgwick, F. Cardinaux, W. C. K. Poon, S. U. Egelhaaf, and P. Schurtenberger, *Nature* **432**, 492 (2004).
- [35] N. Hoffmann, F. Ebert, C. N. Likos, H. Löwen, and G. Maret, *Phys. Rev. Lett.* **97**, 078301 (2006).
- [36] R. P. Sear and W. M. Gelbart, *J. Chem. Phys.* **110**, 4582 (2000).
- [37] F. Sciortino, S. Mossa, E. Zaccarelli, and P. Tartaglia, *Phys. Rev. Lett.* **93**, 055701 (2004).
- [38] S. Mossa, F. Sciortino, P. Tartaglia, and E. Zaccarelli, *Langmuir* **20**, 10756 (2004).
- [39] Y. Liu, W. R. Chen, and S. H. Chen, *J. Chem. Phys.* **122**, 044507 (2005).
- [40] A. Imperio and L. Reatto, *J. Phys.: Condens. Matter* **16**, 3769 (2004).
- [41] A. Imperio and L. Reatto, *J. Chem. Phys.* **124**, 164712 (2006).
- [42] N. Hoffman, H. Löwen, and C. N. Likos, *J. Phys.: Condens. Matter* **18**, 10193 (2006).
- [43] B. Götzelmann, R. Evans, and S. Dietrich, *Phys. Rev. E* **57**, 6785 (1998).
- [44] C. N. Likos, C. Mayer, E. Stiakakis, and G. Petekidis, *J. Phys.: Condens. Matter* **17**, 3379 (2005).
- [45] S. W. Provencher, *Comput. Phys. Commun.* **27**, 213 (1982).
- [46] J. A. Higgins and H. C. Benoît, *Polymers and Neutron Scattering*, Clarendon Press, Oxford, 1986.
- [47] B. M. Mladek, D. Gottwald, G. Kahl, M. Neumann, and C. N. Likos, *Phys. Rev. Lett.* **96**, 045701 (2006).
- [48] B. Krüger, L. Schäfer, and A. Baumgärtner, *J. Phys. (Paris)* **50**, 3191 (1989).
- [49] G. S. Grest and K. Kremer, *Phys. Rev. A* **33**, 3628 (1986).
- [50] O. F. Olaj, W. Landschbauer, and H. Pelinka, *Macromolecules* **13**, 299 (1980).

-
- [51] O. F. Olaj, G. Zifferer, and H. Rehmann, *Monatsh. Chemie* **116**, 1395 (1985).
- [52] A. Y. Grosberg, A. R. Khalatur, and A. R. Khokhlov, *Makrom. Chem. Rapid Commun.* **3**, 709 (1982).
- [53] L. Schäfer and A. Baumgärtner, *J. Phys. (Paris)* **47**, 1431 (1986).
- [54] J. Dautenhahn and C. K. Hall, *Macromolecules* **27**, 5933 (1994).
- [55] A. Jusufi, J. Dzubiella, C. N. Likos, C. von Ferber, and H. Löwen, *J. Phys.: Condens. Matter* **13**, 6177 (2001).
- [56] G. S. Grest, K. Kremer, and T. A. Witten, *Macromolecules* **20**, 1376 (1987).
- [57] C. von Ferber, A. Jusufi, M. Watzlawek, C. N. Likos, and H. Löwen, *Phys. Rev. E* **62**, 6949 (2000).
- [58] J. Batoulis and K. Kremer, *Macromolecules* **22**, 4277 (1989).
- [59] C. N. Likos, M. Schmidt, H. Löwen, M. Ballauff, D. Pötschke, and P. Lindner, *Macromolecules* **34**, 2914 (2000).
- [60] C. N. Likos, S. Rosenfeldt, S. Dingenouts, M. Ballauff, P. Lindner, N. Werner, and F. Vögtle, *J. Chem. Phys.* **117**, 1869 (2002).
- [61] M. Doi and S. F. Edwards, *The Theory of Polymer Dynamics*, Clarendon Press, Oxford, 1 edition, 1986.
- [62] W. H. Stockmayer, *Makromolekulare Chemie* **35**, 54 (1960).
- [63] B. H. Zimm, W. H. Stockmayer, and M. Fixman, *J. Chem. Phys.* **22**, 1716 (1953).
- [64] M. Daoud, J. P. Cotton, B. Farnoux, G. Jannink, G. Sarma, H. Benoit, R. Duplessix, and P. G. de Gennes, *Macromolecules* **8**, 804 (1975).
- [65] S. F. Edwards, *Proceedings of the Physical Society of London* **85**, 613 (1965).
- [66] F. J. Rogers and D. A. Young, *Phys. Rev. A* **30**, 999 (1984).
- [67] J. Dzubiella, C. N. Likos, and H. Löwen, *J. Chem. Phys.* **116**, 9518 (2002).
- [68] P. Attard, *J. Chem. Phys.* **91**, 3083 (1989).
- [69] B. Loppinet, E. Stiakakis, D. Vlassopoulos, G. Fytas, and J. Roovers, *Macromolecules* **34**, 8216 (2001).

-
- [70] E. Zaccarelli, C. Mayer, A. Asteriadi, C. N. Likos, F. Sciortino, J. Roovers, H. Iatrou, N. Hadjichristidis, P. Tartaglia, H. Löwen, and D. Vlassopoulos, *Phys. Rev. Lett.* **95**, 268301 (2005).
- [71] K. Binder and W. Kob, *Glassy Materials and Disordered Solids*, World Scientific, Singapore, 2005.
- [72] E. Zaccarelli, H. Löwen, P. P. F. Wessels, F. Sciortino, P. Tartaglia, and C. N. Likos, *Phys. Rev. Lett.* **92**, 225703 (2004).
- [73] E. Stiakakis, D. Vlassopoulos, and J. Roovers, *Langmuir* **19**, 6645 (2003).
- [74] R. L. C. Vink, A. Jusufi, J. Dzubiella, and C. N. Likos, *Phys. Rev. E* **72**, 030401 (2005).
- [75] M. E. Cates and M. R. Evans, editors, *Soft and Fragile Matter: Nonequilibrium Dynamics, Metastability and Flow*, volume 53 of *Scottish Graduate Series*, Institute of Physics, Bristol, 2000.
- [76] D. Vlassopoulos, *J. Polym. Sci. B: Polym. Phys.* **42**, 2931 (2004).
- [77] R. G. Larson, *The Structure and Rheology of Complex Fluids*, Oxford, New York, 1999.
- [78] M. Ediger, *Ann. Rev. Phys. Chem.* **51**, 99 (2000).
- [79] P. G. Denenedetti and F. H. Stillinger, *Nature* **410**, 259 (2001).
- [80] C. Mayer, E. Stiakakis, E. Zaccarelli, C. N. Likos, F. Sciortino, P. Tartaglia, H. Löwen, and D. Vlassopoulos, to appear in *Rheol. Acta* (2007).
- [81] J. Roovers, L. L. Zhou, P. M. Toporowski, M. Vanderzwan, H. Iatrou, and N. Hadjichristidis, *Macromolecules* **26**, 4324 (1993).
- [82] J. Roovers, P. Toporowski, and J. Martin, *Macromolecules* **22**, 1897 (1989).
- [83] P. M. Toporowski and J. Roovers, *J. Polym. Sci. A: Polym. Chem.* **24**, 3009 (1986).
- [84] L. L. Zhou, N. Hadjichristidis, P. M. Toporowski, and J. Roovers, *Rubber Chemistry and Technology* **65**, 303 (1992).
- [85] E. Stiakakis, D. Vlassopoulos, B. Loppinet, J. Roovers, and G. Meier, *Phys. Rev. E* **66**, 051804 (2002).
- [86] J. Sato and V. Breedveld, *Appl. Rheol.* **15**, 390 (2005).

-
- [87] T. G. Mason and D. A. Weitz, *Phys. Rev. Lett.* **75**, 2770 (1995).
- [88] J. J. Crassous, R. Regisser, M. Ballauff, and N. Willenbacher, *J. Rheol.* **49**, 851 (2005).
- [89] L. Raynaud, B. Ernst, C. Verge, and J. Mewis, *J. Colloid Interface Sci.* **181**, 11 (1996).
- [90] J. Grandjean and A. Mourchid, *Europhys. Lett.* **65**, 712 (2004).
- [91] J. S. Thakur and J. Bosse, *Phys. Rev. A* **43**, 4378 (1991).
- [92] J. S. Thakur and J. Bosse, *Phys. Rev. A* **43**, 4388 (1991).
- [93] A. Imhof and J. K. G. Dhont, *Phys. Rev. Lett.* **75**, 1662 (1995).
- [94] G. Nägele and J. Bergenholtz, *J. Chem. Phys.* **108**, 9893 (1998).
- [95] J. Bergenholtz and M. Fuchs, *Phys. Rev. E* **59**, 5706 (1999).
- [96] C. Mayer, C. N. Likos, and H. Löwen, *Phys. Rev. E* **70**, 041402 (2004).
- [97] F. Sciortino, P. Tartaglia, and E. Zaccarelli, *Phys. Rev. Lett.* **91**, 268301 (2003).
- [98] E. Zaccarelli, G. Foffi, F. Sciortino, and P. Tartaglia, *Phys. Rev. Lett.* **91**, 108301 (2003).
- [99] A. J. Moreno and J. Colmenero, *J. Chem. Phys.* **125**, 016101 (2006).
- [100] A. J. Moreno and J. Colmenero, *Phys. Rev. E* **74**, 021409 (2006).
- [101] A. J. Moreno and J. Colmenero, *J. Chem. Phys.* **125**, 164507 (2006).
- [102] W. Götze and M. Sperl, *Phys. Rev. E* **66**, 011405 (2002).
- [103] E. Zaccarelli, G. Foffi, K. A. Dawson, F. Sciortino, and P. Tartaglia, *Phys. Rev. E* **63**, 031501 (2001).
- [104] T. Gleim, W. Kob, and K. Binder, *Phys. Rev. Lett.* **81**, 4404 (1998).
- [105] P. Kumar, S. V. Buldyrev, F. Sciortino, E. Zaccarelli, and H. E. Stanley, *Phys. Rev. E* **72**, 021501 (2005).
- [106] A. N. Rissanou, D. Vlassopoulos, and I. A. Bitsanis, *Phys. Rev. E* **71**, 011402 (2005).

-
- [107] F. Sciortino, P. Tartaglia, and E. Zaccarelli, *Phys. Rev. Lett.* **91**, 1 (2003).
- [108] E. Zaccarelli, I. Saika-Voivod, , A. J. Moreno, S. V. Buldyrev, P. Tartaglia, and F. Sciortino, *J. Chem. Phys.* **124**, 124908 (2006).
- [109] M. Sperl, *Phys. Rev. E* **69**, 011401 (2004).
- [110] F. Lo Verso, M. Tau, and L. Reatto, *J. Phys.: Condens. Matter* **15**, 1505 (2003).
- [111] F. Lo Verso, L. Reatto, G. Foffi, P. Tartaglia, and K. A. Dawson, *Phys. Rev. E* **70**, 061409 (2004).
- [112] F. Lo Verso, C. N. Likos, and L. Reatto, *Prog. Colloid Polym. Sci.* **133**, 78 (2006).
- [113] J.-P. Hansen and L. Verlet, *Phys. Rev.* **184**, 151 (1969).
- [114] F. Lo Verso, C. N. Likos, C. Mayer, and L. Reatto, *Mol. Phys.* **104**, 3523 (2006).
- [115] M. P. Allen and D. J. Tildesley, *Computer Simulation of Liquids*, Oxford University Press, Oxford, 1987.
- [116] M. Muthukumar, C. K. Ober, and E. L. Thomas, *Science* **277**, 1225 (1998).
- [117] T. C. B. McLeish, editor, *Theoretical Challenges in the Dynamics of Complex Fluids*, volume 339 of *NATO ASI*, Kluwer, London, 1997.
- [118] M. Pitsikalis, N. Hadjichristidis, and J. W. Mays, *Macromolecules* **29**, 179 (1996).
- [119] D. Vlassopoulos, T. Pakula, G. Fytas, M. Pitsikalis, and N. Hadjichristidis, *J. Chem. Phys.* **111**, 1760 (1999).
- [120] F. Clément, A. Johner, J. J. Joanny, and A. N. Semenov, *Macromolecules* **33**, 6148 (2000).
- [121] Y. D. Zaroslov, G. Fytas, N. Hadjichristidis, O. E. Philippova, and A. R. Khokhlov, *Macromol. Chem. Phys.* **206**, 173 (2005).
- [122] A. N. Semenov, J. F. Joanny, and A. R. Khokhlov, *Macromolecules* **28**, 1066 (1995).
- [123] A. G. Zilman and S. A. Safran, *Eur. Phys. J. E* **4**, 467 (2001).

- [124] X.-X. Meng and W. B. Russel, *Macromolecules* **36**, 10112 (2003).
- [125] S. R. Bhatia and W. B. Russel, *Macromolecules* **33**, 5713 (2000).
- [126] U. Batra, W. B. Russel, M. Pitsikalis, S. Sioula, J. W. Mays, and J. S. Huang, *Macromolecules* **30**, 6120 (1997).
- [127] D. Vlassopoulos, M. Pitsikalis, and N. Hadjichristidis, *Macromolecules* **33**, 9740 (2000).
- [128] M. Pitsikalis and N. Hadjichristidis, *Macromolecules* **28**, 3904 (1995).
- [129] F. Lo Verso, C. N. Likos, C. Mayer, and H. Löwen, *Phys. Rev. Lett.* **233**, 102 (2006).
- [130] A. Y. Grosberg and A. R. Khokhlov, *Statistical Physics of Macromolecules*, AIP, New York, 1994.
- [131] P. G. de Gennes, *Solid State Physics, Supplement 14: Liquid Crystals*, Academic, New York, 1978.
- [132] G. Arya and A. Z. Panagiotopoulos, *Phys. Rev. Lett.* **95**, 188301 (2005).
- [133] J. L. Lebowitz and J. S. Rowlinson, *J. Chem. Phys.* **41**, 133 (1964).
- [134] C. N. Likos and N. W. Ashcroft, *J. Chem. Phys.* **97**, 9303 (1992).
- [135] F. Lado, *Phys. Rev. Lett.* **89**, 196 (1982).
- [136] L. Verlet and J.-J. Weis, *Phys. Rev. A* **5**, 939 (1972).
- [137] W. Götze and T. Voigtmann, *Phys. Rev. E* **67**, 021502 (2003).
- [138] J.-L. Barrat and A. Latz, *J. Phys.: Condens. Matter* **2**, 4289 (1990).

Acknowledgments

I want to express my gratitude to all the people who contributed to this thesis by their help.

First of all, I would like to thank Professor Dr. Christos N. Likos for his guidance and the knowledge he taught me in the last years. It was a a great pleasure working with him. He always had time for extended discussions.

I want to express my gratitude to Professor Dr. Hartmut Löwen. In particular I would like to thank him for all the stimulating discussions we had and his valuable suggestions and comments.

I also want to thank Professor Dr. Kurt Binder for refereeing this thesis.

I am very grateful to Dr. Emanuela Zaccarelli for our long-time collaboration concerning the glass transition in soft colloids. We had a lot of discussions related to dynamical arrest and she gave numerous contributions to this thesis. Additionally, I want to thank her, Professor Francesco Sciortino, and Professor Piero Tartaglia for the kind hospitality during my stay in Rome.

I would like to thank Professor Dimitris Vlassopoulos, Professor Georgios Petekidis and Dr. Emmanuel Stiakakis who performed the experiments quoted in this work. It was very rewarding to compare the theoretical results with the reality.

I would like to thank Dr. Federica Lo Verso for the work about telechelic and attractive star polymers we have done together. She is not only a great collaborator

but also a good friend.

I owe special thanks to Dr. Norman Hoffmann and Martin Konieczny with whom I shared my office in the last years. We had a great time and a lot of fun together. They are my 'oldest' friends at the university.

I also want to thank all the other colleagues at our institute. They contributed to a great working atmosphere without which scientific work would not be possible and that made the time appear so much shorter.

I also want to thank Stephan Theiss for his support he gave in many ways through the years. I really learned a lot from him.

The Gründerstiftung zur Förderung von Forschung und wissenschaftlichem Nachwuchs an der Heinrich-Heine-Universität Düsseldorf enabled me to do this work by giving me a Ph. D. fellowship for which I am very grateful.

Finally, I want to thank my parents who gave me the possibility to study. I know that they will be always there if I need them. Moreover, I would like to thank all my friends who provided me with the certainty that there is a life beyond physics.

Die hier vorgelegte Dissertation habe ich eigenständig und ohne unerlaubte Hilfe angefertigt. Die Dissertation wurde in der vorgelegten oder in ähnlicher Form noch bei keiner anderen Institution eingereicht. Ich habe bisher keine erfolglosen Promotionsversuche unternommen.

Düsseldorf, den 05.02.2007

(Christian Mayer)